EUSKAL HERRIKO U NIBERTSITATEA - UNIVERSIDAD DEL PAIS VASCO
MATERIALEN FISIKA SAILA - DEPARTAMENTO DE FÍSICA DE MATERIALES

Nano-FTIR -

Nanoscale Infrared Near-Field Spectroscopy

Florian Huth

- PhD Thesis -

Thesis supervisor
Prof. Rainer Hillenbrand

2015

Universidad del País Vasco Euskal Herriko Unibertsitatea

AUTORIZACION DEL/LA DIRECTOR/A DE TESIS

PARA SU PRESENTACION

Dr/a. **Rainer Hillenbrand** con N.I.F **X9481047X**

como Director/a de la Tesis Doctoral:

Nano-FTIR - Nanoscale Infrared Near-Field Spectroscopy

realizada en **CIC NanoGUNE**

por el Doctorando Don/ña. **Florian Huth**,

autorizo la presentación de la citada Tesis Doctoral, dado que reúne las condiciones necesarias para su defensa.

En Donostia - San Sebastian a 27 de Enero de 2015

EL/LA DIRECTOR/A DE LA TESIS

Fdo.: _____

Universidad del País Vasco Euskal Herriko Unibertsitatea

AUTORIZACION DEL PONENTE DE TESIS

PARA SU PRESENTACION

Dr/a. **Jose Maria Pitarke**

como Ponente de la Tesis Doctoral:

Nano-FTIR - Nanoscale Infrared Near-Field Spectroscopy

realizada en **CIC NanoGUNE**

por el Doctorando Don/ña. **Florian Huth**,

y dirigida por el Dr./a **Rainer Hillenbrand**

autorizo la presentación de la citada Tesis Doctoral, dado que reúne las condiciones necesarias para su defensa.

En Donostia - San Sebastian a 27 de Enero de 2015

EL PONENTE DE LA TESIS

Fdo.: _____

Universidad del País Vasco Euskal Herriko Unibertsitatea

CONFORMIDAD DEL DEPARTAMENTO

El Consejo del Departamento de **Fisica de Materiales**

en reunión celebrada el día ___ de _____ de _____ ha acordado dar la conformidad a la admisión a trámite de presentación de la Tesis Doctoral titulada:

Nano-FTIR - Nanoscale Infrared Near-Field Spectroscopy

dirigida por el/la Dr/a. **Rainer Hillenbrand**

---

y presentada por Don/ña. **Florian Huth**

ante este Departamento.

En Donostia – San Sebastian a _____ de _____ de 2015

VºBº DIRECTOR/A DEL DEPARTAMENTO

SECRETARIO/A DEL DEPARTAMENTO

Fdo.: _____

Fdo.: _____

Universidad del País Vasco Euskal Herriko Unibertsitatea

ACTA DE GRADO DE DOCTOR O DOCTORA
ACTA DE DEFENSA DE TESIS DOCTORAL

DOCTORANDO/A DON/DÑA. **Florian Huth**

TITULO DE LA TESIS: **Nano-FTIR - Nanoscale Infrared Near-Field Spectroscopy**

El Tribunal designado por la Comisión de Postgrado de la UPV/EHU para calificar la Tesis Doctoral arriba indicada y reunido en el día de la fecha, una vez efectuada la defensa por el/la doctorando/a y contestadas las objeciones y/o sugerencias que se le han formulado, ha otorgado por_____la calificación de:

unanimidad ó mayoría

SOBRESALIENTE / NOTABLE / APROBADO / NO APTO

Idioma/s de defensa (en caso de más de un idioma, especificar porcentaje defendido en cada idioma): _____

En Donostia – San Sebastian a ____de _____de 2015

EL/LA PRESIDENTE/A, EL/LA SECRETARIO/A,

Fdo.: Fdo.:

Dr/a: _____ Dr/a: _____

VOCAL 1º, VOCAL 2º, VOCAL 3º,

Fdo.: Fdo.: Fdo.:

Dr/a: _____Dr/a:_____Dr/a:_____

EL/LA DOCTORANDO/A,

Fdo.: _____

Contents

1 Summary

Optical spectroscopy in the infrared (IR) frequency range has tremendous merit in chemical and structural analysis of materials. IR radiation addresses a rich variety of light-matter interactions because photons in this low energy range can excite molecular vibrations and phonons, as well as plasmons and electrons of non-metallic conductors[1,2]. A widely used analytical tool for chemical identification of inorganic, organic and biomedical materials[3], as well as for exploring conduction phenomena[4], is Fourier Transform Infrared Spectroscopy[2] (FTIR), which will be briefly introduced in chapter 3 of this thesis. In infrared spectroscopy the unique response of materials to broadband infrared illumination is utilized to identify and characterize them. The majority of the characteristic interactions are found in the so-called "finger-print" region of the infrared spectrum spanning from 5 – 20 μm wavelength (corresponding to 400 – 2000 wavenumbers [cm^{-1}]). However, the diffraction-limited spatial resolution of this technique, which is in the range of 10 μm, has been preventing applications in nanoscale material and device analysis, industrial failure analysis or quality control.

Recently, tip-enhanced near-field optical microscopy[5] and scattering-type scanning near-field optical microscopy (s-SNOM)[6,7] have become valuable methods for nanoscale material characterization. They enable optical spectroscopies such as fluorescence, Raman, infrared or terahertz spectroscopy to be performed with nanoscale spatial resolution[5]. At infrared frequencies, s-SNOM enables for example the nanoscale mapping of free carriers in transistors[8], semiconductor nanowires[9,10] and vanadium oxide[11,12], of chemical composition of polymers[13-17] and biological objects[18,19], of phonons[20,21] and strain[22] in polar crystals, or of plasmons in graphene[23,24]. Chapter 3 of this work will introduce the basic principles of this technique. It is typically based on atomic force microscopy (AFM) where the tip is illuminated with a focused laser beam. The tip-scattered light is detected simultaneously to topography providing an excellent optical resolution in the 10 nm range, independent of the wavelength[6,7]. Using metallic tips, the strong optical near-field interaction between tip and sample modifies the scattered light, allowing for probing the local dielectric properties with nanoscale resolution.

Local spectral information is obtained, up to now, by time-consuming imaging at various but limited wavelengths from tunable laser sources[13,20,25,26]. The set of near-field

images yield the wavelength-dependent dielectric sample properties, from which local chemical composition or conductivity can be determined[18,27]. For chemical identification of unknown nanostructures, however, the acquisition of local near-field spectra in a broad spectral range spanning from near- to far-infrared frequencies is needed. This issue was addressed in this thesis by developing a novel FTIR system that allows for broadband infrared-spectroscopic nano-imaging of dielectric properties, which became established under the acronym *nano-FTIR*. It combines the analytical power of infrared spectroscopy with the ultra-high spatial resolution of s-SNOM. Utilizing (i) broadband infrared radiation for illuminating the probing tip and (ii) strong signal enhancement employing an asymmetric[28] FTIR spectrometer, the spatial resolution of conventional IR spectroscopy could be improved by more than 2 orders of magnitude. The basic working principles of *nano-FTIR* are presented in chapter 5 of this work.

Nano-FTIR has been experimentally realized with different broadband sources during this thesis. In a first step, a thermal source, similar to what is used in conventional infrared spectroscopy has been implemented for broadband infrared illumination (chapter 6). By mapping a semiconductor device, spectroscopic identification of silicon oxides and quantification of the free-carrier concentration in doped Si regions with a spatial resolution better than 100 nm could be demonstrated[29].

Due to the limited power of the thermal source, however, only strong phonon and plasmon resonances could be mapped, but not the vibrational contrasts of molecular organic substances, which rely on relatively weak resonances[30]. Therefore the *nano-FTIR* setup was combined with a novel laser-based infrared continuum source[31], which is able to provide broadband illumination of sufficient power for detecting the weak molecular vibrational resonances of organic samples (chapter 7). It could be demonstrated, for the first time, that *nano-FTIR* can acquire molecular vibrational spectra throughout the mid-infrared fingerprint region at a spatial resolution of 20 nm, by imaging a typical polymer sample (poly(methyl methacrylate), PMMA). Furthermore, first experimental evidence has been provided that the near-field absorption spectra match well with conventional (far-field) FTIR absorption spectra. Theoretical considerations corroborate this observation (chapter 7.4). This relates, in particular, to the spectral line positions, line widths and line shapes, and therefore allows for direct chemical recognition of nanoscale materials by consulting standard

FTIR databases. As an application example, the identification of a nanoscale sample contamination was demonstrated.

In typical IR s-SNOM studies and also in the first experiments with *nano-FTIR*, standard (commercial) metalized AFM tips were used. The infrared antenna performance of these tips[32], however, is widely unexplored and antenna concepts[33-47] have not yet been applied to optimize near-field probes for the infrared spectral range. In chapter 8 of this work a novel concept is proposed, aiming for superior probing tips that utilize geometrical resonances to optimize the optical performance of tips in near-field optical experiments. By focused ion beam (FIB) machining infrared-resonant antenna tips could be successfully fabricated on standard Si cantilevers. Characterization of these tips by electron energy loss spectroscopy (EELS), Fourier transform infrared (FTIR) spectroscopy and Fourier transform infrared near-field spectroscopy (nano-FTIR) clearly revealed geometrical antenna resonances in the tips, which are found to be in good agreement with numerical calculations. Employing these tips for near-field infrared imaging of individual tobacco mosaic viruses (TMV), state-of-the-art AFM performance accompanied by an excellent optical performance could be verified. Due to their well-defined geometry, these antenna tips will furthermore significantly ease the qualitative description of the tip-sample near-field interaction, which will be essential for quantitative measurements of the local sample properties such as dielectric function and molecular absorption.

In conclusion, a novel technique for nanoscale infrared spectroscopy (named "nano-FTIR") has been developed. It enables the analysis of a large variety of materials with nanoscale spatial resolution and has interesting application potential in widely different sciences and technologies, ranging from materials to chemical and biological sciences. Envisioned applications include nanoscale chemical mapping of polymer blends, organic fibers, and biomedical tissue, as well as quantitative and contact-free measurement of the local free-carrier concentration and mobility in doped nanostructures.

2 Resumen

La espectroscopia óptica presenta unas cualidades excepcionales para el análisis químico y estructural de los materiales; especialmente, en las frecuencias del rango del infrarrojo (IR) y de los terahercios (THz). La radiación IR y de THz abarca una gran variedad de interacciones entre luz y materia, ya que, en este rango de baja energía, los fotones pueden excitar vibraciones moleculares y fonones, así como plasmones y electrones de conductores no metálicos[1,48-50], motivo por el cual actualmente se están dirigiendo ingentes esfuerzos al desarrollo de sistemas de captura de imágenes en estas regiones[51,52]. Una de las herramientas analíticas que más se utiliza para la identificación de materiales inorgánicos, orgánicos y biomédicos[3], así como en el estudio de los fenómenos de conductividad[4], es la Espectroscopia Infrarroja por Transformada de Fourier (FTIR), la cual expondremos brevemente en el Capítulo 3 de esta tesis. En la espectroscopia infrarroja, la respuesta única que los materiales generan ante radiación infrarroja de banda ancha se emplea para la identificación y caracterización unívoca de los mismos. La mayoría de las interacciones características se producen en la denominada región de «huella» (fingerprint region) del espectro infrarrojo, que comprende el rango de longitud de onda entre 5 y 20 μm (correspondiente a números de onda entre 400 y 2000 cm^{-1}). Esta técnica, sin embargo, dada su resolución espacial, limitada por la difracción, y situada en el rango de las 10 μm, no ha podido ser aplicada para el análisis de dispositivos y materiales en escalas micro y nanométricas, o en análisis de procesos industriales y control de calidad.

Recientemente, la microscopía óptica de campo cercano aumentada en la punta[6] ("tip-enhanced near-field optical microscopy") se ha convertido en un importante método para la caracterización de materiales a escala nanométrica. Esta técnica permite realizar análisis basados en la espectroscopia óptica, tales como la espectroscopia de fluorescencia, la espectroscopia Raman y la espectroscopia de infrarrojos o de terahercios, con una resolución espacial de nanómetros[5]. El amplio y prometedor potencial de esta técnica ha quedado probado en múltiples estudios. En las frecuencias de infrarrojos, la microscopía óptica de barrido de campo cercano de tipo dispersivo (s-SNOM)[6,7] permite, por ejemplo, mapear a escala nanométrica los portadores libres en transistores[8], nanohilos semiconductores[9,10] y óxido de vanadio[11,12], la composición

química de polímeros[13-16] y objetos biológicos[18,19], la tensión en cerámicas[22] y los plasmones en grafeno[23,24]. En el Capítulo 4 presentaremos los principios básicos de esta técnica, que, por lo general, suele estar basada en un microscopio de fuerzas atómicas (AFM), donde la punta se ilumina con un haz concentrado de luz láser; de ese modo, la luz dispersada desde la punta se detecta al mismo tiempo que la topografía, proporcionando así una excelente resolución óptica en el rango de los 10 nm, cualquiera que sea la longitud de onda[6,7]. Al utilizar puntas metálicas, la fuerte interacción óptica que se produce entre la punta y la muestra modifica la luz dispersada, gracias a lo cual se pueden estudiar las propiedades dieléctricas locales con resolución nanométrica.

Hasta ahora, la información espectral local de un material se obtenía mediante un lento proceso de captura de imágenes a diferentes –y limitadas– longitudes de onda, empleando diversas fuentes láser de amplitud modulable[13,20,25,26]. El conjunto de imágenes de campo cercano permite revelar las propiedades dieléctricas de la muestra que dependen de la longitud de onda, a partir de las cuales se puede determinar la composición química o la conductividad de la misma[18,27]; sin embargo, para poder identificar nanoestructuras desconocidas, resulta necesario obtener los espectros de campo cercano locales en un amplio rango espectral, desde el infrarrojo cercano al infrarrojo lejano. Esta problemática ha sido abordada en esta tesis mediante el desarrollo de un innovador sistema FTIR que permite obtener imágenes de espectroscopia infrarroja de banda ancha a escala nanométrica de las propiedades dieléctricas, y que recibe el nombre de *nano-FTIR* (descripción en la Fig. 2.1). Esta técnica combina el poder analítico de la espectroscopia de infrarrojos con la sumamente alta resolución espacial de la técnica s-SNOM. A partir de una radiación infrarroja de banda ancha superconcentrada[5,53] con una antena infrarroja[5,20], de un detector de la luz dispersada, y de un fuerte aumento de la señal gracias al uso de un espectrómetro FTIR asimétrico[28], se consiguió mejorar la resolución espacial de la espectroscopia IR convencional en más de dos órdenes de magnitud. Los principios básicos de la técnica *nano-FTIR* serán descritos en el Capítulo 5.

Durante la realización de esta tesis, y con carácter experimental, se han empleado en este innovador sistema de espectroscopia y de obtención de imágenes (*nano-FTIR*) diversas fuentes de banda ancha. En un primer paso, se utilizó como fuente de iluminación infrarroja de banda ancha una fuente térmica similar a la que se emplea en la espectroscopia infrarroja convencional (Capítulo 6). Al mapear el dispositivo

semiconductor, se pudo constatar la identificación espectroscópica de los óxidos de silicio y la cuantificación de la concentración de portadores libres en regiones altamente dopadas de silicio con una resolución espacial superior a los 100 nm.

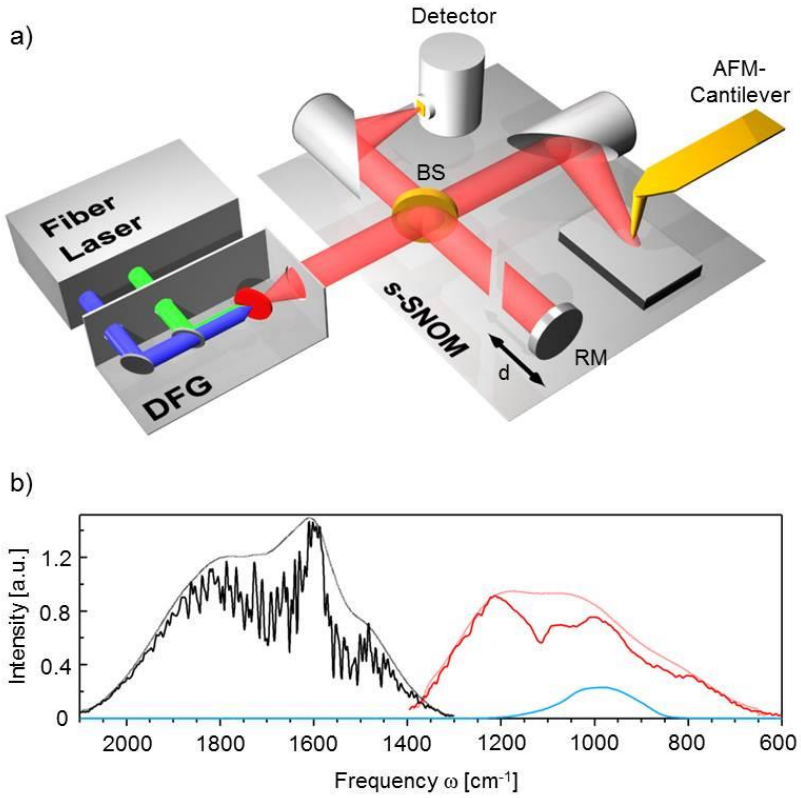

Fig. 2.1 Nano-FTIR con una fuente coherente de luz continua en el infrarrojo medio. **(a)** Configuración experimental que muestra el sistema láser-fibra-Er que emite un tren de pulsos a 1,55 µm (azul), y otro que se ensancha y se vuelve rojo (verde). Una unidad DFG superpone ambos haces en un cristal no lineal, que posteriormente emite un haz continuo en el infrarrojo medio que se utiliza para iluminar la punta del microscopio AFM del sistema nano-FTIR. La luz retrodispersada se analiza con un interferómetro de Michelson asimétrico formado por un divisor de haz (BS) y un espejo de referencia (RM). **(b)** Espectros obtenidos en dos configuraciones del haz continuo en el infrarrojo medio, en la región de "huella" de baja frecuencia 700-1400 cm^{-1} (rojo) y en la región de "huella" de frecuencias más elevadas 1300-2100 cm^{-1} (negro). Las mediciones fueron realizadas a una distancia de unos 2 m de la fuente. Las líneas finas representan los espectros corregidos para la absorción atmosférica.

Sin embargo, debido a la limitada potencia de la fuente térmica, solo se pudieron cartografiar las fuertes resonancias de fonones y plasmones, pero no el contraste vibracional de sustancias orgánicas, que obedece a resonancias relativamente débiles[30]. Por tal motivo, se procedió a combinar el sistema *nano-FTIR* con una novedosa fuente continua de infrarrojos basada en luz láser[31], capaz de proporcionar una luz de banda ancha con la potencia suficiente para poder detectar las resonancias vibracionales débiles de muestras orgánicas (Capítulo 7). Por primera vez, se pudo demostrar que la

técnica *nano-FTIR* permite obtener espectros vibracionales moleculares a lo largo de la región de "huella" en el infrarrojo medio con una resolución espacial de 20 nm, gracias al mapeado de una muestra de polímero PMMA (metacrilato de metilo). Además, se aportaron las primeras pruebas experimentales que demuestran que los espectros de absorción en el infrarrojo cercano se corresponden bien con los espectros de absorción FTIR (Fig. 2.2).

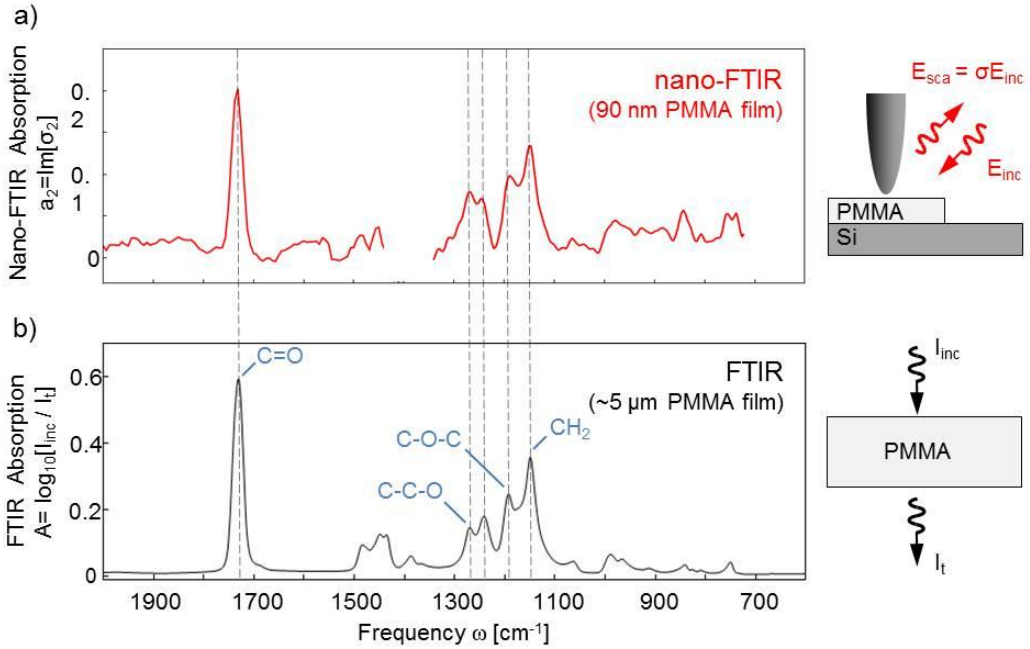

Fig. 2.2 Comparación de la técnica de FTIR de campo lejano convencional con la técnica nano-FTIR **(a)** Espectro de absorción nano-FTIR de una película de 90 nm de PMMA **(b)** Espectro FTIR de campo lejano de una película de PMMA de ~5 µm de grosor. Los datos nano-FTIR se obtuvieron a partir de dos mediciones consecutivas en las que el espectro fue modificado, pasando de los (2000 cm^{-1} – 1400 cm^{-1}) a los (1400 cm^{-1} – 800 cm^{-1}). El tiempo de adquisición fue de 25 y 16 min, respectivamente, y la resolución espectral de 6 cm^{-1}. El espectro FTIR de campo lejano se obtuvo transcurridos 20 min, con una resolución espectral de 4 cm^{-1}. Los esquemas a la derecha de los espectros muestran la técnica nano-FTIR y la técnica FTIR convencional.

Las consideraciones teóricas no hacen sino corroborar esta observación, especialmente en cuanto a las posiciones, al ancho y a la forma de las líneas de los espectros, y que permite, por tanto, reconocer la estructura química de los materiales nanométricos directamente, consultando las bases de datos FTIR estándares. A título de ejemplo de su aplicación, se constató la identificación de la contaminación de una muestra a escala nanométrica (Fig. 2.3)

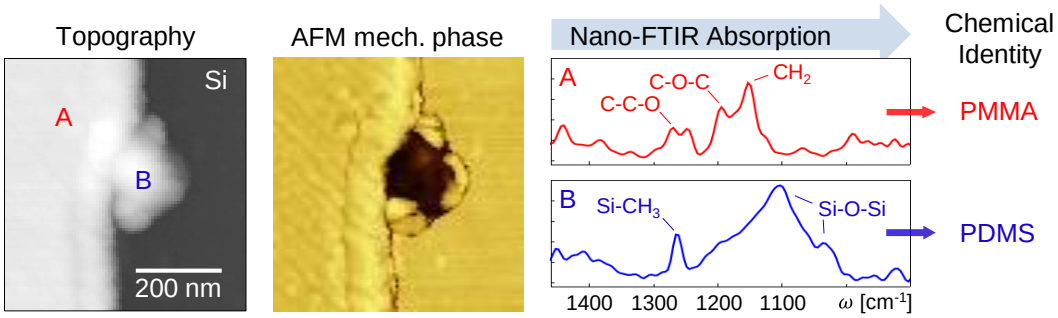

Fig. 2.3 Identificación química de la contaminación en una muestra a escala nanométrica con nano-FTIR. En la imagen de la muestra (izquierda), se puede observar un pequeño contaminante en la muestra (B) junto a una delgada película de PMMA (A) en un sustrato de Si (región oscura). En la imagen correspondiente a la fase mecánica (imagen del medio), el contraste ya pone de manifiesto que la partícula está formada por un material diferente que la partícula y el sustrato. La comparación de los espectros de absorción nano-FTIR en las posiciones A y B (recuadro derecho) con las bases de IR estándar revela la estructura química de la película y de la partícula. El espectro se registró en 7 minutos, con una resolución espacial de 13 cm^{-1}.

En los estudios convencionales de s-SNOM en infrarrojos, así como en los primeros experimentos con *nano-FTIR*, se emplean puntas metalizadas estándares (comerciales) para microscopios AFM. Sin embargo, el rendimiento de estas puntas como antena de infrarrojos[32] sigue siendo un gran desconocido, y los conceptos relativos a las antenas[33-47] aún no han sido aplicados para la mejora de los estudios de campo cercano en el rango de la región infrarroja. En el Capítulo 8 se propone un concepto innovador, basado en el uso de puntas mejoradas que emplean resonancias plasmónicas geométricas para optimizar el rendimiento óptico de las puntas en los experimentos que se realizan en la región del campo cercano. Con un sistema de haz de iones focalizados (FIB), las puntas de antena infrarrojas podrían ser fabricadas con éxito en micro-palancas flexibles (cantilevers) estándares de Si. La caracterización de estas puntas mediante la Espectroscopia de Pérdida de Energía de Electrones (EELS), la Espectrometría Infrarroja por Transformada de Fourier (FTIR) y la Espectroscopia Infrarroja por Transformada de Fourier en Campo Cercano (nano-FTIR) mostró claramente las resonancias geométricas de la antena en las puntas, que se corresponden en buena medida con los cálculos numéricos. El uso de estas puntas en la obtención de imágenes en campo cercano de virus individuales del mosaico del tabaco constató un buen AFM, además de un magnífico rendimiento óptico. Gracias a su bien definida geometría, estas puntas de antena facilitarán notablemente la descripción cualitativa de la interacción entre punta y muestra en la región del campo cercano, lo que resulta

esencial para poder realizar mediciones cuantitativas de las propiedades locales de la muestra, tales como la función dieléctrica y la absorción molecular.

3 Introduction to Fourier Transform Infrared Spectroscopy (FTIR)

In this chapter, a short introduction to infrared spectroscopy will be presented. In particular, Fourier Transform Infrared Spectroscopy (FTIR), which is one of the most common used techniques to measure infrared spectra, will be explained in detail. The concept of a Michelson interferometer as well as the Fourier Transformation will be briefly introduced to understand the experimental formation of infrared spectra.

3.1 Introduction

Infrared spectroscopy uses the infrared region of the electromagnetic spectrum (see Fig. 3.1), that is light with a longer wavelength and lower energy than visible light, to identify and study materials. Photon energies associated with this part of the spectrum efficiently induce vibrational excitations of bonds or groups within molecules.

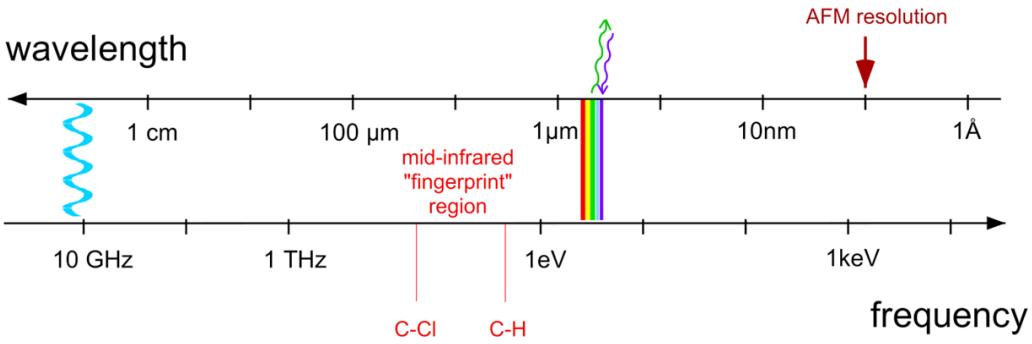

Fig. 3.1 Electromagnetic Spectrum. The mid-infrared part is also called the “fingerprint region”, because many materials exhibit unique vibrational modes in this frequency range, which can be exploited for material identification and characterization.

Molecules experience a wide variety of vibrational motions, characteristic of their component atoms. Consequently, many materials will absorb infrared radiation that corresponds in energy to these vibrations. In the simplest case, the infrared spectrum of a material is recorded by passing a beam of infrared light through it. When the frequency of the infrared light is the same as the vibrational resonance frequency of a

bond, absorption occurs. Examination of the transmitted light reveals how much energy was absorbed at each frequency (or wavelength). As most materials consist of many different atoms and hence a lot of different bonds, the infrared spectra usually are very complex and thus can serve as a unique so-called “infrared fingerprint” of a material. Nowadays huge databases of infrared spectra have been collected, which allow for identification of unknown substances by simply comparing their spectrum with the database.

One of the most common instruments for recording infrared spectra is the Fourier Transform Infrared (FTIR) Spectrometer. Its basic working principle will be introduced in the next paragraphs, conceptually following the description of the book *Fourier Transform Infrared Spectrometry*[2]

3.2 Michelson Interferometer

FTIR spectrometers use an interferometer to measure infrared spectra from the material of interest. Although there exist a lot of different interferometers, the theoretical concept they rely on is not much different from the original design that was introduced in 1891 by Michelson[54,55], which is known as Michelson interferometer and schematically illustrated in Fig. 3.2.

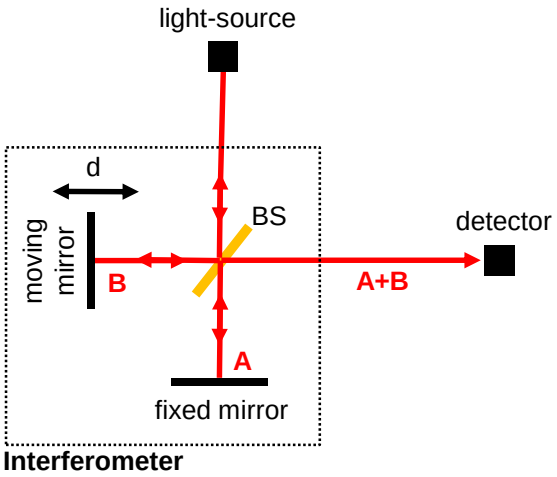

Fig. 3.2 Michelson Interferometer. A collimated beam emitted from a light source is split by a beamsplitter (BS) in two equal beams, the one is reflected by the BS (beam B), the other one is transmitted (beam A). Both beams are reflected back by a mirror perpendicular to their beampaths and recombine again at the BS. Part of the recombined beam is focused onto a detector. One of the mirrors can be moved precisely along the beam propagation axis to change the distance the light travels between the BS and the mirror.

The Michelson interferometer uses a beamsplitter (BS) that splits an incident beam of light into two beams of equal intensity, one is transmitted through the BS (beam A) while the other one is reflected (beam B). Both beams are reflected by a planar mirror back to the beamsplitter, from where they are partly reflected towards the detector. By changing the distance of one of the mirrors (moving mirror, Fig. 3.2), interference between the two beams (A and B) leads to a variation of the intensity at the detector. This variation is measured as a function of the mirror position (i.e. the optical path difference d of the interferometer arms) to form a so-called interferogram, from which the spectrum can be calculated (as shown in detail in the next paragraphs).

To better illustrate the processes that occur in a Michelson interferometer, a simple situation is considered, where the light source is monochromatic and produces a perfectly collimated beam. The wavelength of this source is λ_0[cm], so that its wavenumber (or spatial frequency) ω_0[cm^{-1}] is

$$\omega_0 = \frac{1}{\lambda_0}. \tag{3.1}$$

The electric field emitted by the source is $E_S = |E_S|e^{i\omega_0 t}$, corresponding to a source intensity $I_0 \propto |E_0|^2$. The fields of the two beams A and B after the beam splitter are given by

$$E_A = |E_A|e^{i\omega_0 t} \text{ and } E_B = |E_B|e^{i(\omega_0 t+\varphi)} \tag{3.2}$$

where $\varphi = 4\pi\omega_0 d$ is the phase difference between the two fields because of the path difference d. The intensity at the detector is then given by $I_D \propto |E_D E_D^*|$ where $E_D = E_A + E_B$. It follows:

$$I_D(d) = |E_A|^2 + |E_B|^2 + 2|E_A||E_B|\cos(4\pi\omega_0 d) \tag{3.3}$$

Assuming $I_A = I_B = 0.5I_0$, we obtain:

$$I_D(d) = 0.5I_0(\omega_0)(1 + \cos(2\pi\omega_0 d)) \tag{3.4}$$

When the mirror is moved with a constant speed, the intensity $I_{\mathrm{D}}(d)$ at the detector will vary sinusoidal.

In practice, there are several factors that affect the magnitude of the signal that is measured at the detector, like the transmission of the beamsplitter, responsivity of the detector and detector amplification characteristics. These factors, however, do not change from one measurement to the next for a given system configuration and can be described by a wavenumber-dependent correction-factor $R(\omega_0)$:

$$I_{\mathrm{D}}(d) = 0.5R(\omega_0)I_0(\omega_0)(1 + \cos(2\pi\omega_0 d)) \tag{3.5}$$

By defining $S(\omega_0)$=$0.5R(\omega_0)I_0(\omega_0)$ and omitting the constant term in eq. (3.7), we obtain

$$I(d) = S(\omega_0)cos2\pi\omega_0 d, \tag{3.6}$$

which in FTIR spectroscopy is called the interferogram. The amplitude of the interferogram, $S(\omega_0)$, is the intensity of the source that is only modified by the instrument characteristics.

3.3 Fourier Transform Spectroscopy

The spectrum $S(\omega)$ is calculated by computing the Fourier transform of the interferogram $I(d)$. In case the source is monochromatic (as in chapter 3.2), performing the Fourier transform of a measured interferogram is a trivial operation, since the amplitude and wavelength can both be measured directly from the sinusoidal interferogram. If the source emits either several discrete spectral lines or continuous radiation, however, the interferogram is more complex. Fig. 3.3a illustrates the interferogram of a source that emits at two narrow spectral lines. It is a superposition of two cosine waves, each of them originating from one of the spectral emission lines of the source. For a source that emits a broad spectrum, as in Fig. 3.3b and c, the

interferogram is sinusoidal with an exponentially decaying envelope, as it is now a superposition of many different cosine waves. For an optical path difference $d = 0$, they are all in phase, yielding a maximum signal I_D.The position $d = 0$ is thus called the white light position (WLP). The narrower the width of the spectrum, the wider is the envelope of the interferogram (Fig. 3.3b), and vice versa (Fig. 3.3c).

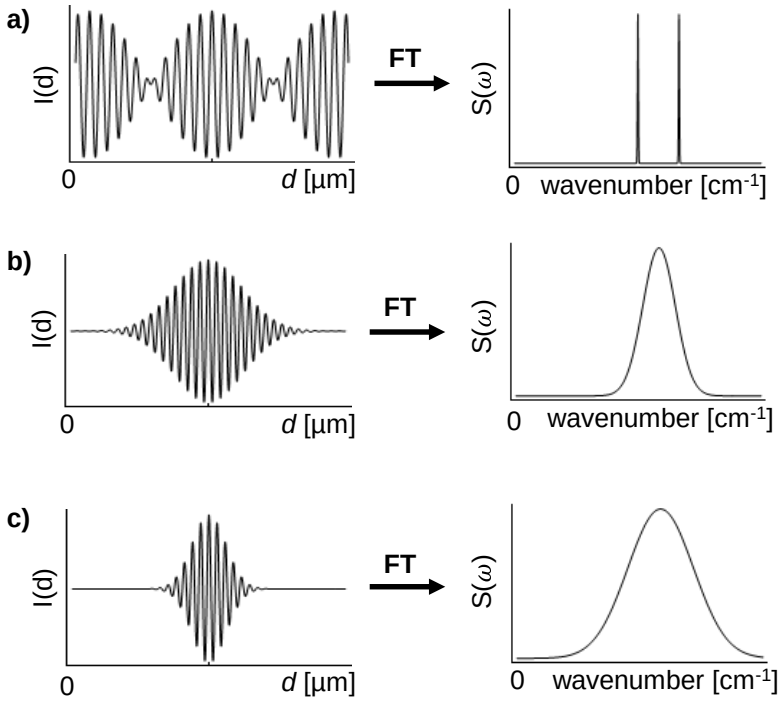

Fig. 3.3 Simple spectra and interferograms: **a)** Two very narrow lines of equal intensity. **b)** Lorentzian band centered at the mean of the lines in (a) **c)** Lorentzian band at the same wavenumber as (b) but of twice the width; FT denotes the Fourier Transform.

When the source is a continuum, the interferogram can be represented by the integral

$$I(d) = \int_{-\infty}^{+\infty} S(\omega) cos 2\pi\omega d \, \mathrm{d}\omega \tag{3.7}$$

which is one-half of a cosine Fourier transform pair, where the other is

$$S(\omega) = \int_{-\infty}^{+\infty} I(d) cos 2\pi\omega d \, \mathrm{d}d \tag{3.8}$$

Eq. (3.8) shows that in theory one could measure the complete spectrum from 0 to ∞ cm^{-1} at infinitely high spectral resolution. To achieve this, however, it would be necessary to scan the moving mirror of the interferometer an infinitely long distance.

The effect of measuring the signal over a limited distance causes the spectrum to have a finite spectral resolution. This will be discussed in detail in section 3.3.1. Also, practically the Fourier transform is performed with data acquisition (DAQ) cards with limited acquisition speed. Thus the signal is recorded in finite sampling intervals dd, which in turn limits the maximum frequency ω_{max} that can be measured. This is called the spectral bandwidth and will be explained in more detail in section 3.3.5.

The most commonly used FTIR spectrometers use a Michelson interferometer to measure the infrared transmission spectra of a sample, as illustrated in Fig. 3.4. A broadband infrared beam is passed through the interferometer and then illuminates the sample. An infrared detector measures the transmitted light.

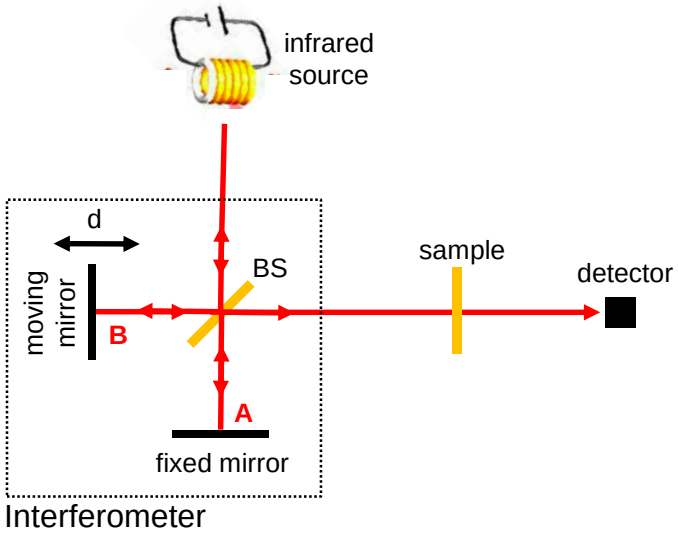

Fig. 3.4 Conventional Transmission-FTIR spectroscopy. Infrared radiation from a broadband infrared source (here: a heated coil) is passed through a Michelson-type interferometer, comprising a beamsplitter (BS), a fixed and a moving mirror. After the interferometer, the light is passed through the sample and then focused onto the detector.

Typically, thermal sources are used as continuous broadband infrared sources. A simple version of such a thermal source is a small coil (see Fig. 3.4), which is heated by a current to > 1000 K. According to Planck´s law, the emission of a blackbody of temperature T (in K) can be described by

$$I(\omega,T)=\frac{2h\omega^3}{c^2}\frac{1}{e^{\frac{h\omega}{k_BT}}-1}, \tag{3.9}$$

where $I(\omega,T)$ denotes the spectral radiance, T the absolute temperature of the blackbody, k_B the Boltzmann constant, h the Planck constant and c the speed of light. Note that the above notation is valid for ω in units of [Hz]. By substituting $\omega[Hz] = 10^2 c\omega[\mathrm{cm}^{-1}]$, $I(\omega,T)$ becomes

$$I(\omega,T)=2*10^6 hc\omega\frac{1}{e^{\frac{10^2 hc\omega}{k_BT}}-1}, \tag{3.10}$$

valid for ω in units of $[\mathrm{cm}^{-1}]$, as it is used throughout this thesis. Already at 1000 K, a thermal source emits radiation spanning from the visible throughout the infrared up to the THz spectral regime[2]. A calculated example emission spectrum will be shown in Fig. 3.6.

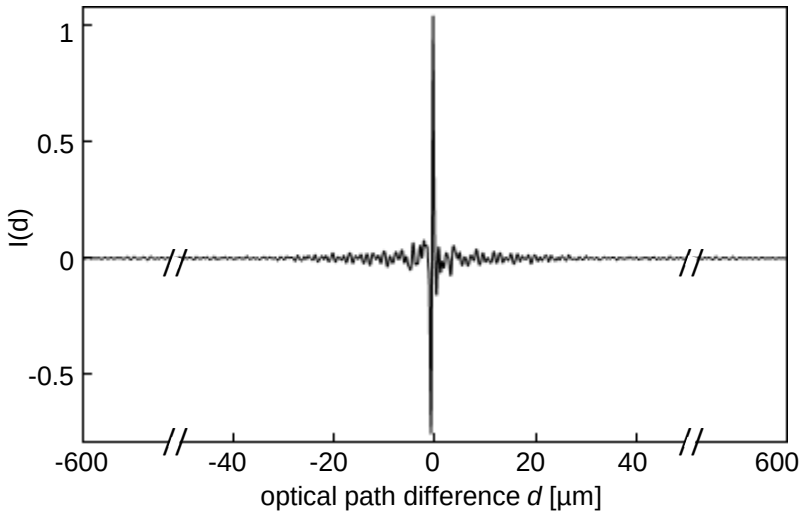

Fig. 3.5 Example interferogram, when a broadband beam is passed through a Michelson interferometer. The intensity $I(d)$ is recorded vs. the delay of the moving mirror (i.e. the optical path difference d between the fixed and the moving mirror). The measurement was performed with a Bruker Hyperion 2000 microscope coupled to a Vertex 70 FTIR spectrometer in the absence of a sample. The measurement was done by Roman Krutokhvostok.

If such a broadband beam is passed through a Michelson interferometer, the resulting interferogram shows only one pronounced peak at the white light position $d = 0$, due to the rapid decay of the envelope, analog to Fig. 3.3c., An example interferogram is shown in Fig. 3.5, measured with a commercial Bruker Hyperion 2000 microscope coupled to a Vertex 70 FTIR spectrometer. The measurement was performed without a sample loaded, i.e. the beam passes only through air.

As described earlier in this section, the infrared spectrum $S(\omega)$ can be obtained by computing the Fourier transform (FT) of the interferogram $I(d)$. Fig. 3.6 shows the spectrum that is obtained from the interferogram from Fig. 3.5 (black). The spectrum shows a maximum intensity at around 2000 cm^{-1} and several distinct absorption peaks. These are well known and originate from atmospheric absorption in the air, that the infrared beam had to pass between the source and the detector. The most prominent ones are due to water vapor around 1600 cm^{-1} and 3700 cm^{-1} and from CO_2 around 2350 cm^{-1} (ref.[56]). As there was no sample through which the broadband beam had to pass, the spectrum (apart from the atmospheric absorption peaks) essentially resembles the emission of the infrared source, convoluted with the responsivity of the used detector. The red curve in Fig. 3.5 shows the simulated emission spectrum of a blackbody emitter at 1000 K according to Planck´s law, as introduced in eq. (3.10). Both spectra, the measured (black) and the simulated (red) have been normalized to their maximum value and a good agreement is found. The small shift might be due to the responsivity of the detector, which typically has a maximum between 1000 cm^{-1} and 1500 cm^{-1}, or the source in the used instrument was operated at a slightly different temperature.

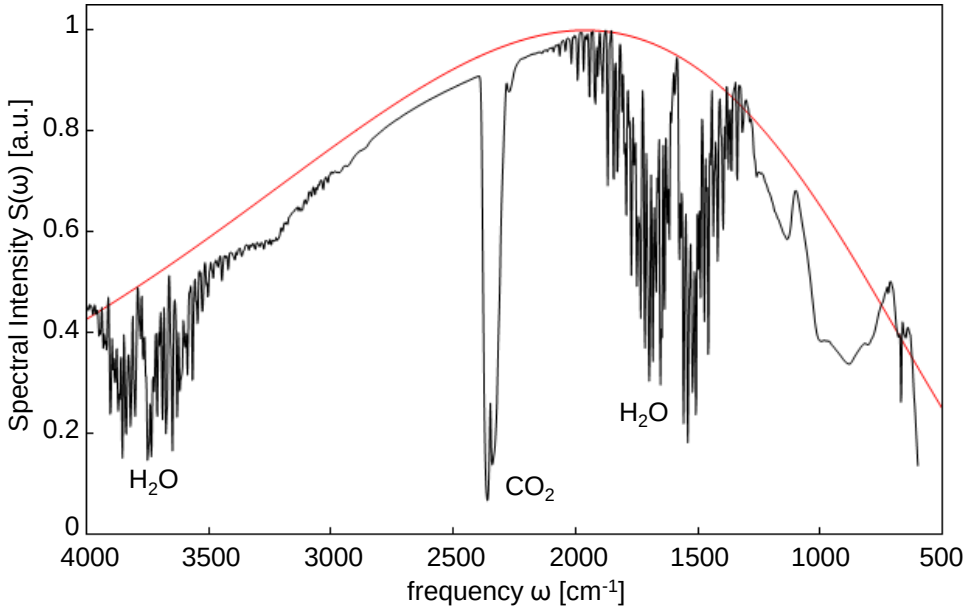

Fig. 3.6 The black spectrum is obtained by performing the FT of the interferogram shown in Fig. 3.5. It was measured in the absence of a sample, and thus resembles the optical properties of the instrument, such as the emission of the broadband source, the responsivity of the infrared detector and atmospheric absorption between source and detector, mostly water vapor (around 1600 cm^{-1} and 3700 cm^{-1}) and CO_2 (around 2350 cm^{-1}). The red curve represents the emission of a blackbody source at 1000 K temperature, calculated according to Planck´s law. Both curves have been normalized to their maximum.

To obtain the infrared spectrum of a sample, the instrument characteristics and the influence of atmospheric absorption have to be known and corrected for. To measure this dependence, a background spectrum $S_{\mathrm{BG}}(\omega)$ like the one in Fig. 3.6 is recorded in absence of a sample and then a spectrum of the sample $S_{\mathrm{Sample}}(\omega)$ is recorded. To extract the pure sample response, independent of the instrument characteristics, the measured sample spectrum, $S_{\mathrm{Sample}}(\omega)$ is normalized to the background spectrum $S_{\mathrm{BG}}(\omega)$, as

$$T(\omega) = \frac{S_{\mathrm{Sample}}(\omega)}{S_{\mathrm{BG}}(\omega)}, \tag{3.11}$$

with $T(\omega)$ being the transmission spectrum of the sample. If the sample would be completely transparent for all measured frequencies, the resulting (normalized) transmission spectrum would be 1 throughout the whole spectrum.

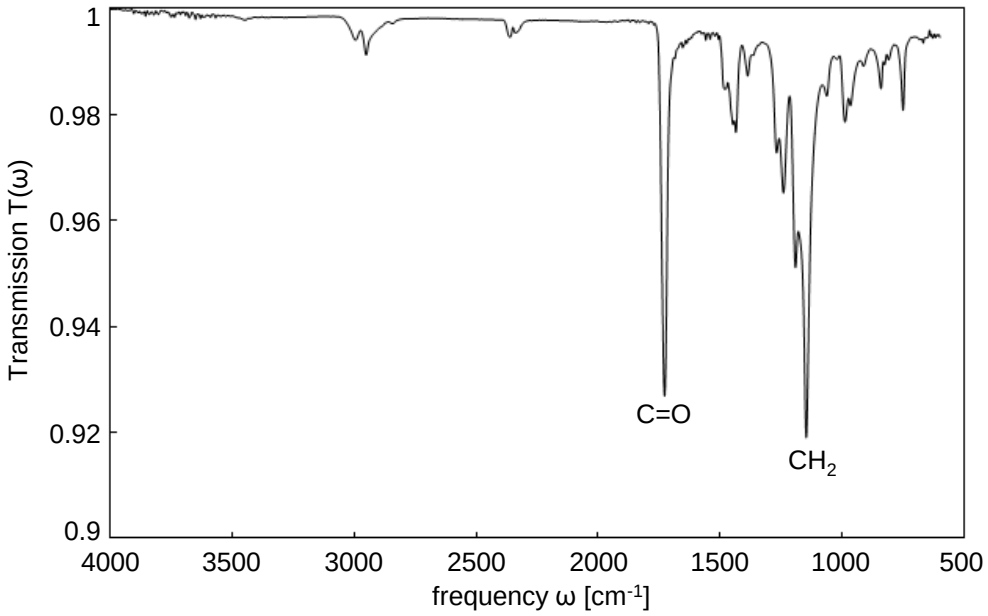

Fig. 3.7 Example infrared transmission spectrum of a thin film of PMMA. In the region from 4000 cm^{-1} to 2000 cm^{-1} the sample is mostly transparent, thus the transmission is almost 1. Below 2000 cm^{-1} a lot of peaks can be found, corresponding to different molecular bonds and their various vibrational modes. The measurement was done by Wiwat Nuansing.

Fig. 3.7 shows the transmission spectrum of a widely used polymer, Poly (methyl methacrylate), in short PMMA. At certain frequencies, the transmission is significantly reduced due to absorption in the material. The absorption occurs, because molecular bonds can be efficiently excited at their resonance frequencies, as those lie in the infrared range. Some bonds have several motional degrees of freedom, and therefore can have also several resonant frequencies at which they absorb. For example, in the spectrum of PMMA, the absorption at 1730 cm^{-1} can be assigned to the stretching mode of the C=O bond, which obviously absorbs very strongly. Due to the complexity of most materials, each material exhibits a unique infrared spectrum, which can serve as a fingerprint, allowing for its identification and characterization. Therefore, infrared spectroscopy is also called fingerprint spectroscopy, and the mid-infrared spectral region is also called the fingerprint region. State-of-the-art infrared spectrometer can measure complete spectra within seconds, making infrared spectroscopy a powerful tool for material analysis and identification.

3.3.1 Spectral Resolution

In FTIR spectroscopy, the spectral resolution is determined by the retardation of the (moving) reference mirror within the Michelson interferometer. To illustrate this, a simplified example is taken, similar to what was used in section 3.3. A source spectrum $S(\omega)$ that consists of only two frequencies, ω_1 and ω_2, both having the same intensity, yields an interferogram $I(d)$ that is a superposition of two cosine waves. (Fig. 3.8a, left side).

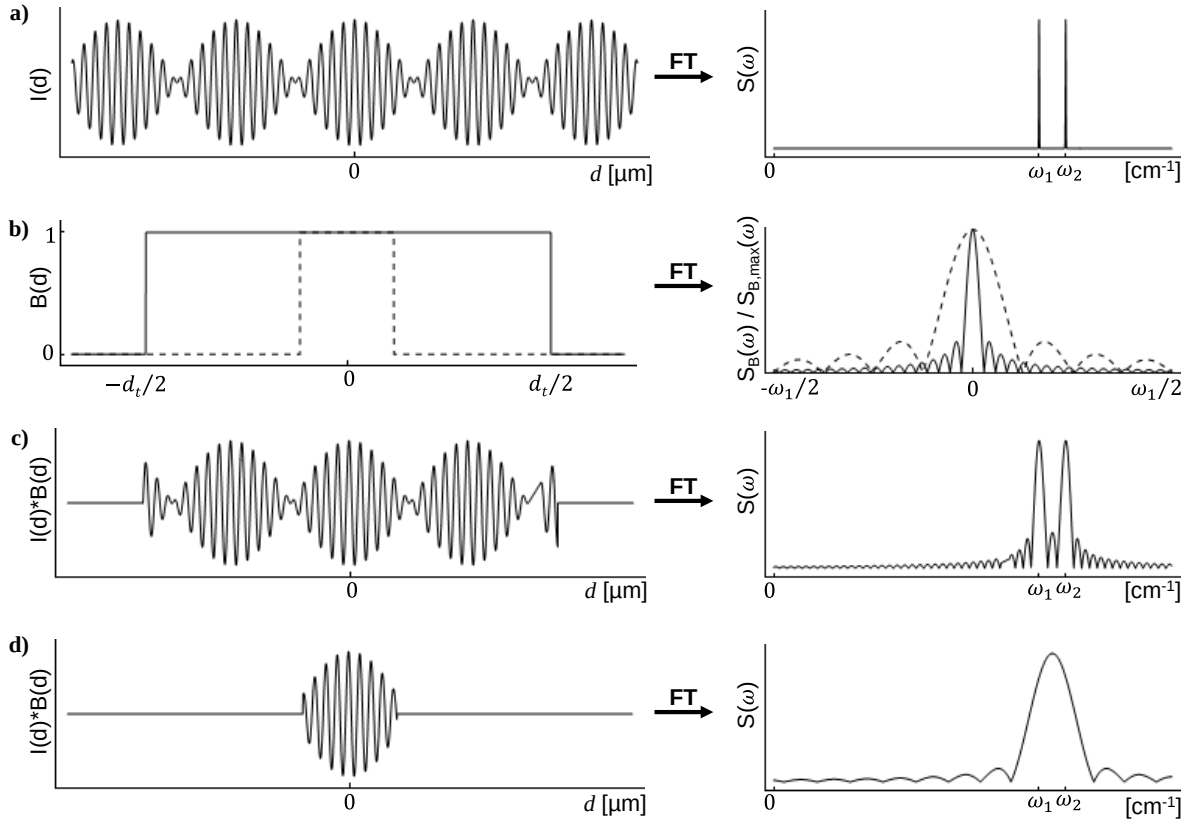

Fig. 3.8 Spectral resolution in FTIR. **a)** An interferogram, resulting from a source spectrum with two narrow lines. **b)** Boxcar truncation functions with different width (solid and dashed line) and their corresponding spectra. Both spectra have been normalized to their maximum value for better comparability **c)** Interferogram of (a), multiplied by the wider boxcar function of (b) and the resulting spectrum. The two peaks are still resolved, but artifacts due to the truncation appear. **d)** Interferogram of (a), multiplied by the narrower boxcar function of (b) and the resulting spectrum. The two separate lines cannot be resolved any more.

When the interferogram is measured over a sufficiently long total optical path difference d_t, the two lines of the source spectrum are well resolved, as can be clearly seen on the right side of Fig. 3.8a. It should be noted that the spectrum in Fig. 3.8a results from an analytical calculation, that performs the FT of the complete (simulated) interferogram,

which is much larger than the shown part. Thus the two spectral lines appear exactly as in the original function that was used to create the simulated interferogram.

To simulate the effect of measuring an interferogram over a finite total optical path difference d_t, the interferogram $I(d)$ of Fig. 3.8a is multiplied with a truncation function

$$B(d) = \begin{cases} 1 & \text{if } -d_t \leq d \leq +d_t \\ 0 & \text{if } |d| > d_t \end{cases} \tag{3.12}$$

which is also called the boxcar truncation function (see Fig. 3.8b, left side, solid line) . The resulting interferogram is shown in Fig. 3.8c, left side. Its spectrum is then given by

$$S(\omega) = \int_{-\infty}^{+\infty} B(d)I(d)\cos(2\pi\omega d)\,\mathrm{d}d, \tag{3.13}$$

as shown in Fig. 3.8c, right side. The two lines of the source spectrum are well resolved. However, their line shape is broadened compared to the original source spectrum, and furthermore oscillations can be observed in the spectrum. Both phenomena can be understood be analyzing eq. (3.13). The Fourier transformation of a product of two functions is known to be the convolution of the Fourier transformation of each of the functions[57,58]. Thus the source spectrum (Fig. 3.8a) is convoluted with the spectrum of the boxcar truncation function (shown in Fig. 3.8b), which can be clearly seen in the resulting spectrum in Fig. 3.8c.

In Fig. 3.8d, the original interferogram has been multiplied by the boxcar truncation function shown as a dashed line in Fig. 3.8b to simulate a measurement with smaller total optical path difference d_t compared to Fig. 3.8c. Again the resulting spectrum (Fig. 3.8d, right side) is a convolution of the original spectrum with the spectrum of the truncation function (shown in Fig. 3.8b, dashed line). As the width of the (dashed) spectrum is larger than the separation of the two lines in the source spectrum, they cannot be resolved anymore and only one broad peak is observed. Thus, the spectral resolution in this (simulated) measurement is not sufficient to resolve the two lines as separate features.

In general, an interferogram of total optical path difference d_t yields a spectral resolution $\Delta\omega_{min}$ that is given by

$$\Delta\omega_{min}[\mathrm{cm}^{-1}] = \frac{1}{d_t[\mathrm{cm}]} \tag{3.14}$$

The origin of eq. (3.14) can be directly derived from the spectrum of the truncation function that used for Fig. 3.8c, which is shown in Fig. 3.9. The distance between the first minima on the positive and negative side is $1/d_t$, which provides a measure of how much a spectral feature will be broadened by the effect of measuring over a finite optical path difference d_t.

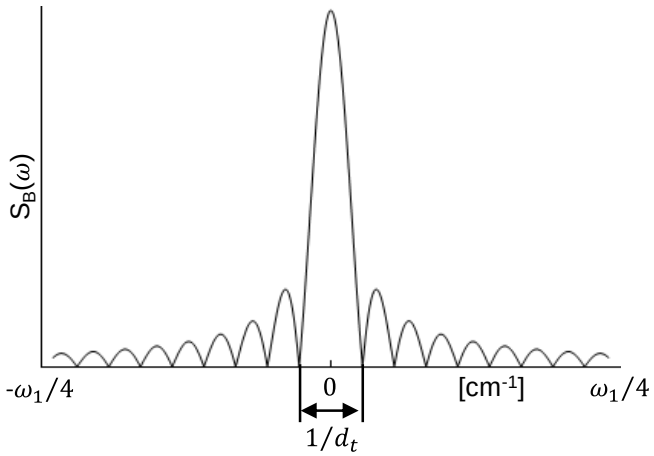

Fig. 3.9 Spectrum of the boxcar function that was used in Fig. 3.8c. The distance between the first minimum on the positive and negative side defines the spectral resolution.

Thus, if two spectral features are separated by at least $1/d_t$, they can be resolved in the measured spectrum[2]. From eq. (3.14) it can be easily calculated, what the maximum spectral resolution for a real spectrometer is. For example, when the moving mirror of the interferometer is mounted on a piezostage, which can travel a distance of up to 800 µm (and thereby create a maximum optical path difference of 1600 µm), the maximum spectral resolution is $\Delta\omega_{min} = (0.16\ \mathrm{cm})^{-1} = 6.25\ \mathrm{cm}^{-1}$.

3.3.2 Apodization

As demonstrated in the previous section, measuring an interferogram over a finite optical path difference d_t causes artificial oscillations to appear in the resulting spectrum due to the convolution with the spectrum of the truncation function. The oscillations can be minimized by apodization of the measured interferogram. Apodization is performed by multiplying the interferogram by a function $A(d)$ that is unity in the center of the interferogram and tends to zero at the edges of the interferogram. Fig. 3.10a shows the boxcar function (black), an example apodization function (red, Gaussian) and their corresponding FT spectra. It can be clearly seen, that there are no oscillations in the spectrum of the apodization function (red curve in the right panel of Fig. 3.10a). Fig. 3.10b shows the interferogram from Fig. 3.8c that has additionally been multiplied with the apodization function $A(d)$ and the resulting spectrum. As already indicated by the spectrum of the apodization function, the resulting spectrum does not exhibit the oscillations that have been observed in Fig. 3.8c. The drawback of apodization, however, is the slightly decreased spectral resolution, as can be seen by comparing the spectra of the boxcar function and the apodization function (Fig. 3.10a, right side, black and red spectrum).

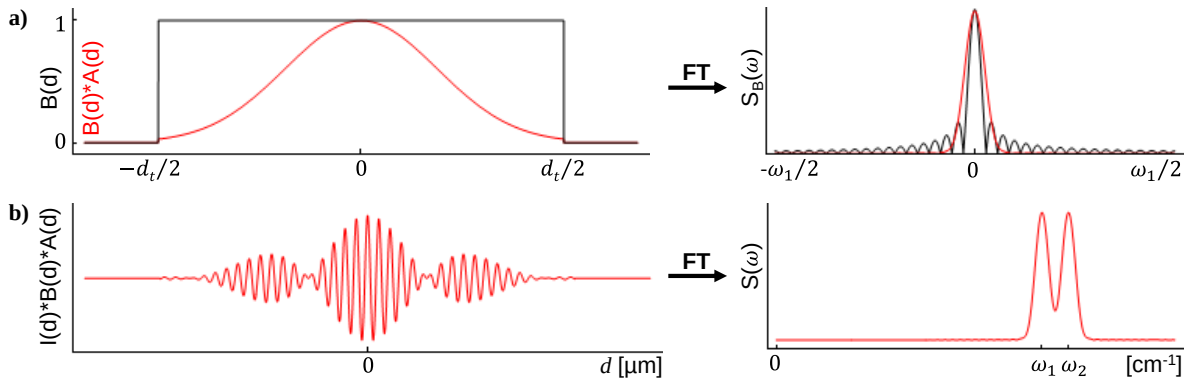

Fig. 3.10 Apodization in FT spectroscopy. a) the boxcar function (black) and a Gaussian apodization function (red). b) The interferogram from Fig. 3.8c, multiplied by the boxcar and the apodization function (left) and the resulting spectrum (right).

3.3.3 Discrete Fourier Transformation

The considerations in the previous section have been made by calculations of analytical functions, i.e. continuous FT has been applied for the calculations . Thus, the resulting spectra from such a computation in principle have an infinite sampling rate (i.e. data points). In a real measurement, however, an interferogram is measured by a data acquisition card (DAQ), which has a limited acquisition speed. The interferogram is measured at finite sampling intervals, returning a data set with a discrete number of data points. To calculate the spectrum from such discrete interferograms , a discrete Fourier Transformation is required.

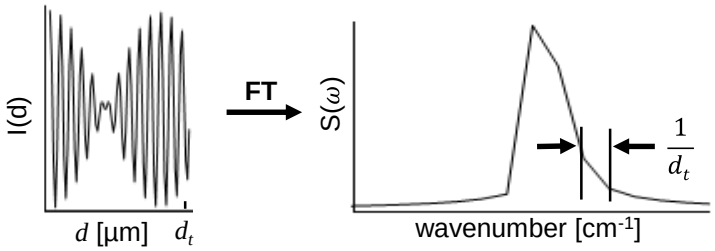

Fig. 3.11 Example interferogram and resulting spectrum, obtained by performing the discrete FT.

Fig. 3.11 shows a part of the same interferogram that was used in Fig. 3.8c, but now is it discretized to a finite number of data points (here: 80 data points). Performing a discrete Fourier Transform, its spectrum is obtained. Fig. 3.11 shows that this spectrum has a limited number of data points, which are spaced exactly by $1/d_t$, the spectral resolution. It turns out that due to the discrete sampling of the interferogram the spectral resolution seems to be decreased. This issue can be addressed by zero-filling, or *padding*, which will be demonstrated in the next section.

3.3.4 Zero Filling / Padding

As illustrated in Fig. 3.11, when an interferogram is measured with a finite sampling interval over a total optical path difference d_t, the resulting spectrum has data points that are spaced by $1/d_t$ and this seemingly decreases the spectral resolution. Obviously, two spectral features in a distance of $1/d_t$ cannot be properly resolved, if the spacing between the data points is only $1/d_t$. They would simply be neighboring

data points in the spectrum and could not be identified as individual peaks. This issue can be addressed by artificially increasing the total optical path difference d_t by adding zeros to both ends of the interferogram. This procedure is called zero-filling or padding, and is demonstrated in Fig. 3.12

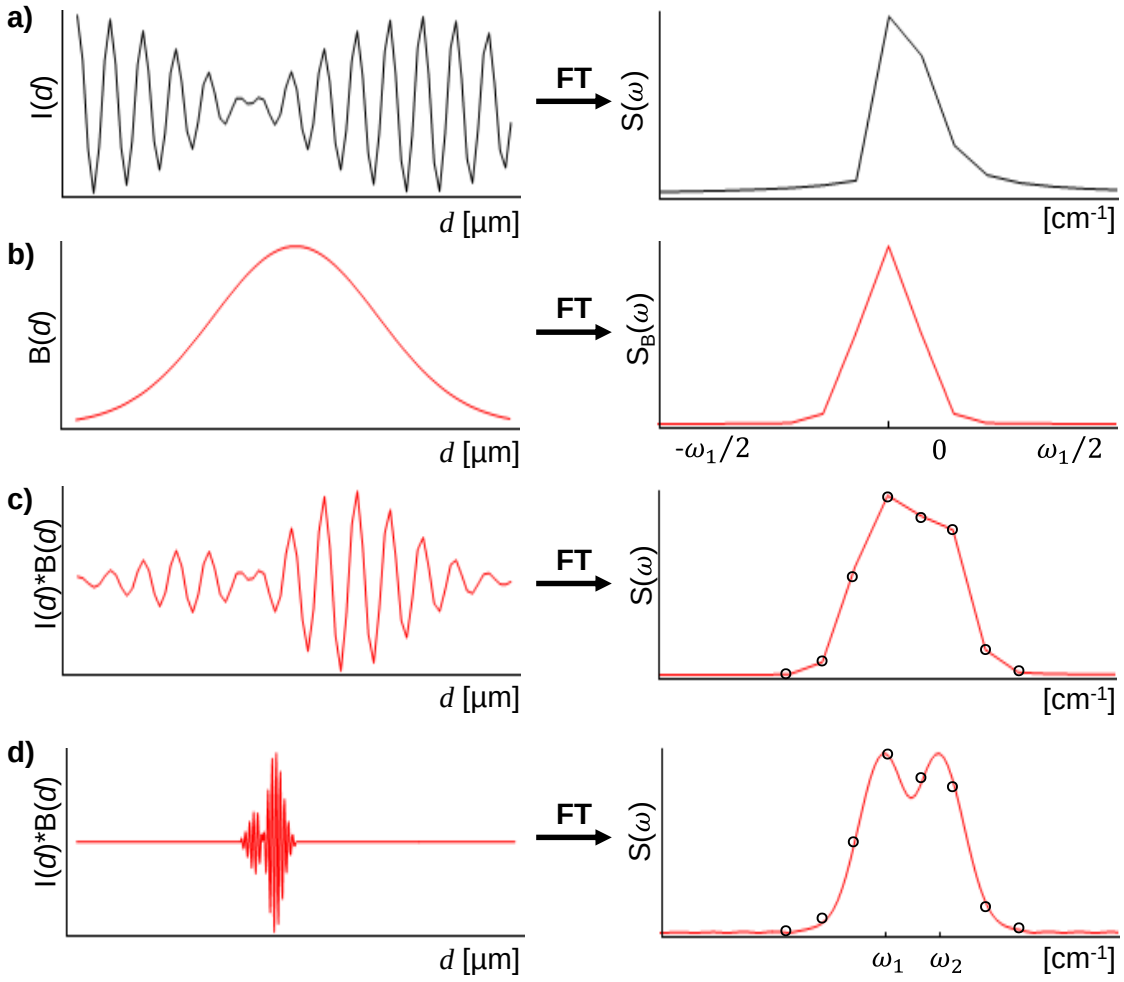

Fig. 3.12 Zero-Filling. **a)** The interferogram from Fig. 3.11, and the resulting spectrum. **b)** The apodization function from Fig. 3.10a, adjusted to the length of (a) and discretized to the same number of points (80). On the right side is the discrete FT of the apodization function. **c)** The interferogram of (a) multiplied with the apodization function from (b), and the resulting FT spectrum d) The interferogram of (c) which has been extended by a factor of 8, by adding zeros at both ends. On the right side, the resulting FT spectrum is shown. The black dots in the spectrum mark the data points of the (c) spectrum, to illustrate that zero-filling does not change the original data points, but adds new intermediate points.

The interferogram in Fig. 3.12a is the same as shown in Fig. 3.11 and the resulting spectrum is shown to the right. Only one broad peak can be observed. In Fig. 3.12b, the apodization function of Fig. 3.10a is shown, now also discretized to 80 points to fit the

interferogram in Fig. 3.12a. Its discrete FT spectrum, shown in Fig. 3.12b on the right, also has the same number of data points, which are spaced equally to those in the spectrum of Fig. 3.12a. In Fig. 3.12c, the interferogram of Fig. 3.12a has been multiplied with the apodization function from Fig. 3.12b and the resulting FT spectrum is shown on the right. There is still only one broad peak observed, which is additionally broadened due to the apodization. In Fig. 3.12d, the interferogram of Fig. 3.12c has been extended by a factor of 8 by adding zeros on both sides and the resulting FT spectrum is shown to the right. It can be clearly seen that the resulting spectrum has more data points (i.e. they are more closely spaced) and two peaks can be observed. It should be noted that no new information was added by performing the zero-filling, and also the spectral resolution cannot be increased by this technique. However, the spectrum gets smoother, and peaks that are spaced closely to the resolution limit can be visualized better, due to higher sampling of the spectrum (i.e. more data points per cm^{-1}). The black circles in both spectra in Fig. 3.12c and d mark the data points of the original (un-padded) spectrum and show that zero-filling does not change the original data points, it rather adds new points between them.

3.3.5 Spectral Bandwidth

The spectral bandwidth in FTIR determines the maximum (optical) frequency that can be measured. When an interferogram is recorded by a fast digital instrument, the signal has to be digitized. Thus the (originally continuous) signal is discretized in a limited number of pixels, resulting in a limited bandwidth. When the optical path difference of the interferometer is d_t and the resulting interferogram is divided in n equidistant steps (or pixels), then the resulting spectral bandwidth is determined by

$$\omega_{\max}[\mathrm{cm}^{-1}] = \frac{n}{2\, d_{\mathrm{t}}[\mathrm{cm}]} \tag{3.15}$$

The factor 2 on the right side of eq. (3.15) is due to the symmetry of the discrete Fourier Transformation. The FT returns a spectrum ranging from 0 to $2\omega_{\max}$, but only information about the first half is obtained, since the second half is simply its conjugate[57]. Note that the maximum frequency ω_{max} is a spatial frequency (with units

cm^{-1}), which is very convenient, as the most infrared spectra are also given in these units, rather than in wavelength λ. However, the units can be easily converted according to

$$\lambda[\mu\mathrm{m}] = \frac{10^4}{\omega[\mathrm{cm}^{-1}]} \tag{3.16}$$

The frequency $\omega = 1000\ \mathrm{cm}^{-1}$ for example thus converts to a wavelength $\lambda = 10\ \mu\mathrm{m}$. Sometimes radiation is also described by its temporal frequency, that is, how often the electric field oscillates per second. The conversion from spatial to temporal frequencies can be done according to

$$f[\mathrm{Hz}] = c\ \omega[\mathrm{cm}^{-1}] \tag{3.17}$$

with c being the speed of light. The frequency of $\nu = 1000\ \mathrm{cm}^{-1}$ thus converts to approximately $f \approx 30\ \mathrm{THz}$.

3.4 Micro-Spectroscopy

In conventional FTIR spectroscopy, as illustrated in Fig. 3.4, IR spectra are acquired from typically macroscopic samples. The collimated infrared beam passes a bulk sample, and the resulting spectrum is an average over the total illuminated area. No spatial variations can be distinguished. For spectroscopy of local material properties, the sample needs to be imaged through small apertures (see Fig. 3.13), as the spatial extension of thermal sources prevents diffraction limited focusing.

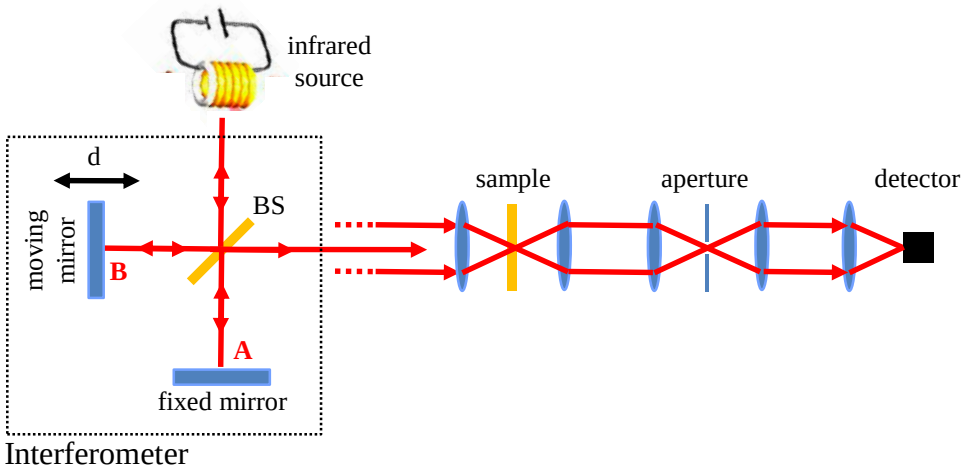

Fig. 3.13 Micro-FTIR spectroscopy. After passing the interferometer, the broadband infrared light is focused on the sample. With a small aperture the measured sample area can be spatially restricted to gain access to spatial variations on the sample.

Equipped with apertures (as illustrated in Fig. 3.13), state-of-the-art micro-spectrometers achieve a spatial resolution of about 10 µm (ref.[2]). However, an improvement of several orders of magnitude is needed for IR spectroscopic mapping of nanoscale structures and complexes such as bio-membranes, semiconductor devices or polymer composites. Thus, novel microscopy concepts are required and one of them is developed and presented in this thesis in chapter 5.

4 Introduction to s-SNOM

This chapter provides an introduction to scattering-type Scanning Near-field Optical Microscopy (s-SNOM), a technique that overcomes the diffraction limit in optical imaging by orders of magnitudes. The basic working principle of s-SNOM will be described as well as analytical models for the interpretation of near-field optical image contrasts. (This introduction follows the basic concepts from[59-62])

4.1 Diffraction Limit in Classical Optical Microscopy

Classical optical microscopy uses propagating electromagnetic waves, usually in the visible spectral regime, to form an image of an object under investigation. The image is formed with the help of lenses and objectives. Depending on the properties of these optical elements, the image can be much larger than the original object, revealing small details that cannot be seen by eye. However, if the size of the details gets smaller than the wavelength that is used for imaging the object, the image gets blurred. Due to the diffraction of propagating waves, the image of an ideal point source produced by an optical microscope is not a point anymore. The image of a point source exhibits a ring-shaped structure, which is known as Airy pattern[63,64] (see Fig. 4.1), which leads to a limit in the spatial resolution that can be achieved by conventional light microscopy. Already at the end of the 19th century, E. Abbe and Lord Rayleigh derived a criterion for the diffraction-limited spatial resolution of an optical microscope. The minimal distance Δx_{min} between two imaged point sources at which they can still be unambiguously resolved is given by

$$\Delta x_{min} = \frac{0.61\lambda}{NA} \tag{4.1}$$

Here, λ is the wavelength of the light used for imaging, and $NA = n \sin(2\theta_{max})$ is the numerical aperture. n is the refractive index of the medium surrounding the imaging optics and $2\theta_{max}$ the maximum collection angle of the optical system. The largest values for the NA that can be achieved with recent objectives are in the range between

0.95 − 1.4, leading to a maximum spatial resolution of conventional optical imaging systems in the order of $\Delta x_{min} \approx \lambda/2$, which for visible light amounts to $\Delta x_{min} \approx 200 - 400$ nm. If light of the mid-infrared spectral regime is used, the spatial resolution is in the order of several micrometers.

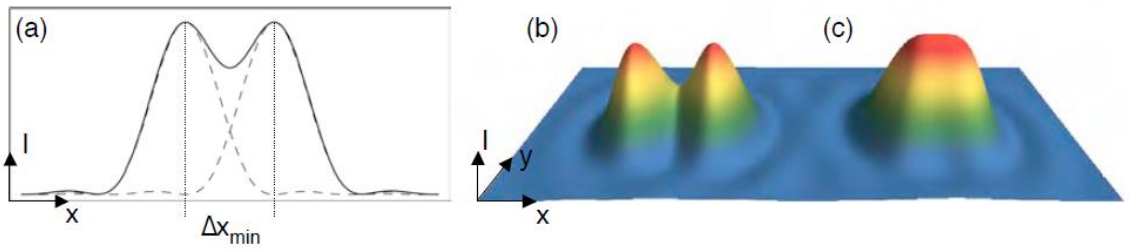

Fig. 4.1 Airy pattern of two closely spaced point sources. (a) Intensity distribution showing the resolution limit based on the Rayleigh criterion. (b) Two point sources separated by $\Delta x > \lambda/2$. (c) The two sources are not resolvable when $\Delta x < \lambda/2$.(Image taken from[59])

Fig. 4.1 shows the calculated intensity distribution of two Airy patterns when two closely spaced ideal point sources are imaged by a conventional optical microscope[64]. According to the Rayleigh criterion, the minimal resolvable distance Δx_{min} between two point sources is defined as their separation, when the maximum of the first Airy pattern is located at the first minimum of the second Fig. 4.1a). If the distance between the point sources is larger than Δx_{min}, they can be clearly resolved (Fig. 4.1b). If $\Delta x < \Delta x_{min}$, the sources cannot be separated anymore in the resulting image (Fig. 4.1c)

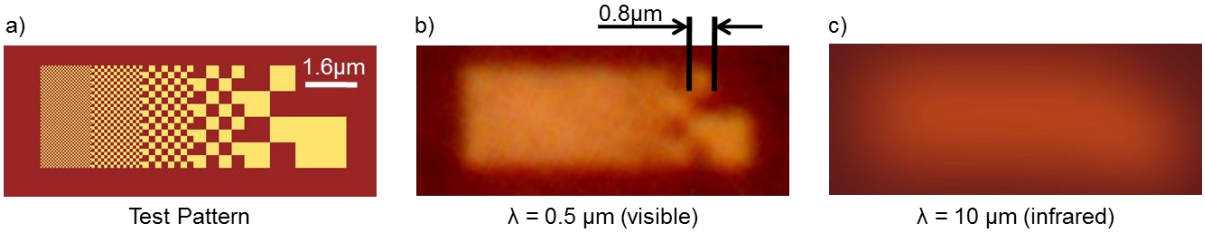

Fig. 4.2 Diffraction-limited Imaging. **(a)** Schematic of a test Pattern with structures from 1.6 µm size down to 100 nm **(b)** Image of the test pattern that was fabricated by patterning a SiC crystal with Focused Ion beam (FIB), using visible light ($\lambda = 0.5$ µm) **(c)** (calculated) image of the test pattern, using infrared light ($\lambda = 10$ µm), no features can be resolved. (Images taken from[60])

As an example, a test pattern (Fig. 4.2a), exhibiting structures from 1.6 µm in size down to 100 nm was patterned in a SiC crystal by Focused Ion Beam (FIB) and imaged with a

conventional light-microscope (wavelength around 0.5 µm, Fig. 4.2b). The 0.8 µm sized structures can still be resolved when using visible light for imaging but the smaller structures already are blurred. The mid-infrared image shown in Fig. 4.2c is not measured, but simulated (details can be found in[60]). Obviously, no structures are resolved, because their separation is smaller than the diffraction limit ($\Delta x_{min} \approx \lambda/2 \approx$ 5 µm for mid-infrared radiation).

4.2 Nanoscale Imaging

To study samples that are smaller than the classical resolution limit of optical microscopy, a variety of methods have been developed. One approach is to use smaller wavelength for imaging. With electrons and ions, wavelengths much smaller than the size of an atom (1 Å = 0.1 nm) can be achieved, enabling atomic resolution imaging. Note that these techniques are still diffraction limited. The drawback is the generally very high energy that is necessary to achieve these small wavelengths, which can be destructive to the sample. Also the technical efforts get quite high, as most of these systems usually require a high vacuum environment.

For biological samples, advances in fluorescence microscopy[65,66] have led to large variety of new techniques that overcome the diffraction limit. Generally in fluorescence microscopy, chemical labelling with fluorescent markers (such as dye molecules) allows for selective mapping of different components of biological samples. Fluorescent markers can be excited by a certain wavelength (typically in the visible regime) and usually emit light at a lower energy wavelength (i.e. longer wavelength) due to relaxation of the excited state. With suitable filters and detectors, even the emission of single molecule fluorescence can be detected. By combining confocal fluorescence microscopy with sophisticated illumination and detection schemes, fluorescence imaging with a spatial resolution well below the diffraction limit can be achieved . Among them is 4Pi microscopy[67], where a second objective below the sample (additional to the one above the sample) increases the total angle of collection, thereby increasing the total NA (numerical aperture) of the system, which leads to a higher resolution. In Stimulated Emission Depletion microscopy (STED)[68], two light pulses are used. The first one is used to excite the fluorophores and a second one quenches the fluorescence actively. Employing a donut-like shape of the second pulse the quenching

only occurs in the outer parts of the pulse, leaving a small area in the center in the excited state to be measured with a time-gated detection, triggered after the second pulse. Thereby the spatial resolution can be improved significantly, reaching about 20 nm (ref.[68]). Other approaches include Photo-Activated Localization Microscopy (PALM)[69], Stochastic Optical Reconstruction Microscopy (STORM)[70], Fluorescence Recovery after Photobleaching (FRAP)[71,72], and Förster Resonance Energy Transfer (FRET)[73].

Another class of microscopy techniques that enables imaging with nanoscale spatial resolution is Scanning Probe Microscopy (SPM)[74,75]. The name SPM originates from the procedure of scanning a sample to create an image by measuring certain quantities for each sample-position. The first SPM technique was introduced in 1982, and is called Scanning Tunneling Microscopy (STM)[76,77]. In STM, a sharp metallic tip is raster-scanned across a sample surface, with typical distances of less than 1 nm[74,75]. For STM, conductive sample are required. By applying a potential between the tip and the sample, a tunneling current can be detected when the tip is in close proximity to the sample. As the tunneling current depends exponentially on the tip sample distance, it is used for precise distance control to create a height profile of the sample surface (topography). STM achieves atomic-scale spatial resolution, due to the current flowing from the very last atom of the tip apex to single atoms at the sample surface.

To overcome the limitation of conductive samples, Atomic Force Microscopy[78] (AFM) was developed. AFM also uses a sharp tip to scan the topography of a sample surface, but in contrast to STM, this technique exploits mechanical interaction forces between tip and sample for distance control. AFM will be introduced in more detail in section 4.3.1.

Since the development of AFM, a large variety of additional techniques have been developed to extend AFM beyond only measuring the height profile (topography) of a sample surface. With additional electrical contacts to the tip and the sample, for example, the local capacity or conductivity of the sample can be measured simultaneously to topography. One approach to achieve optical nano-imaging with AFM is the use of tapered optical fibers as probing tips. Simultaneously to mapping the height, the sample can be illuminated through a small aperture at the end of the fiber-tip, enabling a localized illumination, and thus increasing the achievable optical resolution.

This technique is known as aperture-SNOM (scanning near-field microscopy)[79]. Aperture tips, that is metal coated fibers with a hole at the apex, are cutoff metal waveguides. For an aperture of 50 nm, the achievable transmission for visible light is on the order of 10^{-2} to 10^{-4} (ref.[5]) and will decrease further for smaller diameters or longer wavelengths. At mid-IR frequencies, for example, a 50 nm aperture tip would have a transmission of only 10^{-30}, which is much too small to be of practical use[80]. To overcome the wavelength restriction of aperture-SNOM, scattering-type SNOM (s-SNOM)[5,6,81-85] was developed. s-SNOM will be described in detail in section 4.3. It uses (side-) illumination of the scanning tip by a focused laser beam and measures the backscattered light from the tip-sample system simultaneously to the topography, enabling nanoscale resolved optical imaging. s-SNOM is particularly interesting, because it offers a wavelength-independent resolution[5,7], which makes it also suitable for infrared- and terahertz-nanoimaging[6,8,86].

4.3 Working Principle of s-SNOM

In s-SNOM, a metallic AFM tip is illuminated with a focused laser beam, and the backscattered light is measured to form an optical image with nanometer spatial resolution. In this section, the AFM, the tip illumination and the procedure of extracting the desired optical information from the detected signal will be described in detail. In the end, theoretical models to describe the signal origin are summarized.

4.3.1 Atomic Force Microscopy (AFM)

s-SNOM typically is based on atomic force microscopy (AFM)[78], where a sharp tip is scanned across a sample surface while being held at a constant but very small distance to the sample. Fig. 4.3 provides a schematic illustration of a typical AFM setup. To keep the distance constant, AFM employs a feedback system that exploits mechanical interaction forces between the tip and the sample surface. Therefore, the tip is mounted on a long flexible cantilever. There are several different interaction forces that play a role when the tip gets close to the sample surface. Some of them are attractive, others are repulsive. The main contributing attractive forces are van der Waals forces. If the tip and the sample have a potential difference, attractive electrostatic Coulomb forces can

be generated. In ambient conditions, samples can adsorb water molecules, which create a thin water layer on the sample surface. When the probing tip is close enough a liquid bridge called meniscus is formed[74,75], exhibiting attractive capillary forces. Repulsive forces mainly arise from Pauli repulsion or ionic repulsion at very small distances.

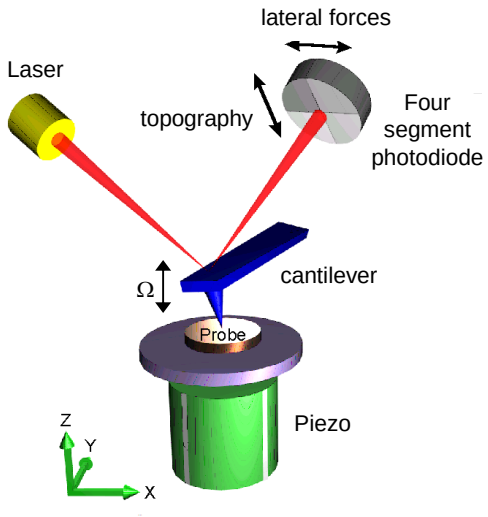

Fig. 4.3 Schematic representation of a typical AFM setup. A laser beam is reflected from the backside of the cantilever, onto a position-sensitve Photodiode. The sample is mounted on a piezo to precisely move the sample up and down. (Image taken from[87])

When the tip approaches the sample surface, first the attractive forces are dominant, causing the cantilever to bend towards the sample. When the tip gets closer to the sample, the repulsive forces start dominating, bending the cantilever in the opposite direction. To detect the bending of the cantilever, a laser beam is reflected from the backside of the cantilever and monitored with a position-sensitive photodiode (e.g. a four-segment photodiode, see Fig. 4.3). In the simplest approach, also called contact mode operation in AFM, the position of the reflected laser beam is kept constant while scanning the tip across the sample. A feedback system increases or decreases the distance between the tip and the sample, depending on the position of the reflecting beam deviating in one or the other direction. The output of the feedback system then resembles the topography of the sample.

Another mode of operation that is widely used, and is also used in s-SNOM, is called tapping mode. Here the tip is again mounted on a cantilever, but now the tip is oscillating at a mechanical resonance Ω of the tip-cantilever system (typically in the range of 10-300 kHz). By demodulating the signal of the position-sensitive photodiode at the oscillation frequency Ω, the oscillation amplitude can be monitored with high precision. As these resonances typically have quite high Q-factors, the oscillating system is very sensitive to external influences, such as the interaction forces mentioned in the previous paragraph. When the tip gets closer to the sample, the oscillation amplitude is damped. Using a feedback-system to keep the oscillation amplitude constant, the topography of a scanned sample can be measured analogous to contact mode.

As will be described in the next paragraphs, tapping mode operation is very suitable for the s-SNOM technique. The oscillation of the tip gives rise to a modulation in the measured optical signal, which will prove very useful.

4.3.2 Tip Illumination and Nano-Focusing

In s-SNOM, usually metal-coated AFM-tips are used. The tip is illuminated with a focused laser beam, as illustrated in Fig. 4.4a. Focusing is usually done with a parabolic mirror. Due to their metallization and sharp apex, these tips act like an antenna[5,20,35,37] and concentrate the illuminating electric field E_{in} to a nanoscale spot at their apex (Fig. 4.4b). The "lightning rod" effect known from electrostatics[5] combined with the excitation of Surface Plasmons Polaritons[5,88,89] in the metal cause a charge accumulation in the tip apex, which gives rise to very high local fields[90]. Fig. 4.4b shows a numerical simulation (boundary element method, BEM) of a metal cone with a sharp tip, which is illuminated with far-infrared light ($\lambda = 118$ µm). The illumination is considered to be a plane wave with linear polarization parallel to the tip axis (p-polarization), as depicted by the yellow arrows. The color scale denotes the field enhancement, that is the ratio between the local field and the incident field. Clearly the electric field is strongly confined around the tip apex, to a dimension much smaller than the illuminating wavelength, and decays exponentially with distance.

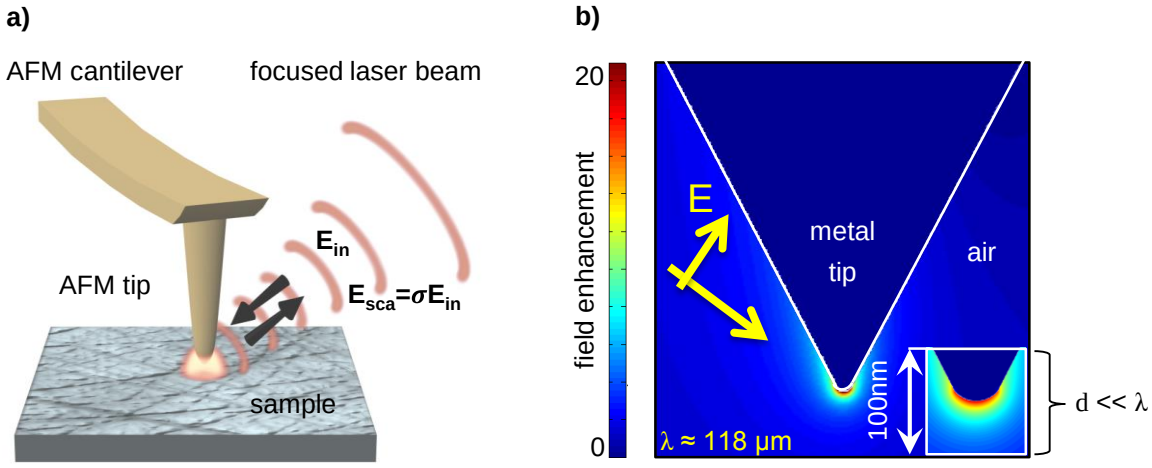

Fig. 4.4 Tip illumination and field enhancement in s-SNOM. **a)** A sharp AFM tip is mounted on a cantilever and illuminated by a focused laser beam. (Image taken from[60]) **b)** Numerical simulation of a metal cone, illuminated by far-infrared light with $\lambda = 118$ µm. (Taken from[8]).

When the illuminated tip comes in close proximity to a sample (closer than the spatial decay of the evanescent hot spot at the tip apex), the near-field interaction between tip and sample modifies the light scattered by the tip. The backscattered light is collected by the same parabolic mirror used for illumination and then is recorded with a detector, yielding nanoscale resolved optical images of the sample surface.

The near-field interaction can be described by the complex valued scattering coefficient $\sigma = se^{i\varphi}$ (with amplitude s and phase φ), which relates the scattered field E_{sca} with the incident field E_{in} according to

$$E_{\mathrm{sca}} = \sigma E_{\mathrm{in}} \tag{4.2}$$

Through σ and because the near-field interaction is localized to the scale of the tip radius, the recorded backscattered light and thus the recorded near-field images carry information about the *local* sample properties. The scattering coefficient σ will be discussed in more details in section 4.4.

4.3.3 Background Suppression

4.3.3.1 Harmonic Signal Demodulation

The scattered field associated with the near-field interaction between the tip and the sample surface, E_{nf}, is not the only contribution to the total backscattered field E_{sca} that is collected by the parabolic mirror. Considering a monochromatic laser source for tip illumination, such as a CO_2 laser, even for the best (diffraction limited) case, the resulting focal spot size is on the order of the used wavelength. For the mid-infrared spectral regime (with wavelengths $\lambda = 2 - 20$ µm), this leads to spot-sizes of several micrometer. Thus the backscattered light contains unavoidable background contributions from scattering off the tip shaft or distant sample positions, E_{bg}, yielding the total scattered field $E_{\mathrm{sca}} = E_{\mathrm{nf}} + E_{\mathrm{bg}}$. The detector thus measures the intensity

$$I_{\mathrm{det}} \propto I_{\mathrm{sca}} \propto |E_{\mathrm{sca}}|^2 = \left|E_{\mathrm{nf}} + E_{\mathrm{bg}}\right|^2 = \left(E_{\mathrm{nf}} + E_{\mathrm{bg}}\right)\left(E_{\mathrm{nf}} + E_{\mathrm{bg}}\right)^* \tag{4.3}$$

As mentioned in section 4.3.1, s-SNOM is based on an AFM operating in tapping mode, where the tip is oscillating vertically with a frequency Ω. The amplitude of the oscillation is set to be much smaller than the wavelength of tip illumination. Typical tapping amplitudes are around 50 nm. Due to the oscillation of the tip, both contributions ($E_{\mathrm{nf}} + E_{\mathrm{bg}}$) are modulated and therefore E_{sca} can be written as

$$E_{\mathrm{sca}} = E_{\mathrm{nf}} + E_{\mathrm{bg}} = \sum_{n=0}^{\infty} E_{\mathrm{nf,n}} \cos(\mathrm{n}\Omega \mathrm{t}) + \sum_{n=0}^{\infty} E_{\mathrm{bg,n}} \cos(\mathrm{n}\Omega \mathrm{t}) \tag{4.4}$$

where $E_{\mathrm{nf,n}} = \sigma_{\mathrm{nf,n}} E_{\mathrm{in}} = s_{\mathrm{nf,n}} e^{i\varphi_{\mathrm{nf,n}}} E_{\mathrm{in}}$ and $E_{\mathrm{bg,n}} = \sigma_{\mathrm{bg,n}} E_{\mathrm{in}} = s_{\mathrm{bg,n}} e^{i\varphi_{\mathrm{bg,n}}} E_{\mathrm{in}}$ denote the n^{th} order complex-valued Fourier coefficients of E_{nf} and E_{bg}, respectively.

As the near-field scattering E_{nf} arises from the interaction of an evanescent local field at the tip apex with the sample, it is strongly non-linear with the tip-sample distance. This nonlinearity efficiently creates signal contributions in the higher harmonics nΩ of the tip oscillation frequency Ω. In contrast, the background scattering E_{bg} only changes due

to the spatial variation of the incident electric field, which occurs in the length-scale of its wavelength[6,7]. As the tip oscillation amplitude is set to values much smaller than the used wavelength, the background scattering can in good approximation be considered to change linear with the tip position. Therefore the contribution of the background scattering to the signal is mostly restricted to the oscillation frequency Ω. By demodulating the detected signal at sufficiently high harmonics nΩ (in the infrared usually for $n \geq 2$) the Fourier coefficients $\sigma_{\mathrm{bg,n}}$ are negligible compared to the Fourier coefficients $\sigma_{\mathrm{nf,n}}$(refs.[6,7]), i.e. $\sigma_{\mathrm{nf,n}} \gg \sigma_{\mathrm{bg,n}}$.

Thus, if the electric field E_{sca} were measured directly, signal demodulation at a sufficiently high harmonic nΩ would extract the desired near-field signal. However, with the infrared detectors that are commonly used in s-SNOM, the intensity is measured, rather than the field E_{sca}. As the intensity is the square of the field, $I_{\mathrm{det}} \propto I_{\mathrm{sca}} \propto |E_{\mathrm{sca}}|^2$, the near-field and background terms are mixed (ref.[60]). By calculating the square of (4.4) and assuming that $E_{\mathrm{bg,n}}$ is negligible for $\mathrm{n} > 1$, the signal at demodulation orders $\mathrm{n} \geq 2$ becomes

$$U_{\mathrm{n}} \propto E_{\mathrm{bg,0}} E^*_{\mathrm{nf,n}} + E_{\mathrm{nf,n}} E^*_{\mathrm{bg,0}} \tag{4.5}$$

Eq. (4.5) shows that all harmonic components of the detected signal are affected by $E_{\mathrm{bg,0}}$. This is known as the multiplicative background[91]. Thus, direct measurement of the back-scattered light intensity and subsequent demodulation is not sufficient to obtain completely background-free near-field signals.

4.3.3.2 Pseudo-heterodyne Interferometric Detection

A solution to also suppress the multiplicative background contribution was presented by Ocelic et al.[91]. By recording the tip-scattered light with a Michelson interferometer, modulation of the reference phase and appropriate analysis of the modulated detector signal, completely background-free near-field signals can be obtained. This detection scheme is called pseudo-heterodyne detection and will be briefly summarized in this section. Apart from superior background suppression, the interferometric detection

offers another valuable advantage, which is to access both the amplitude and the phase of the backscattered light. As will be shown in chapter 5 and 7, the phase carries useful information about the sample, eventually enabling chemical identification with nanoscale spatial resolution.

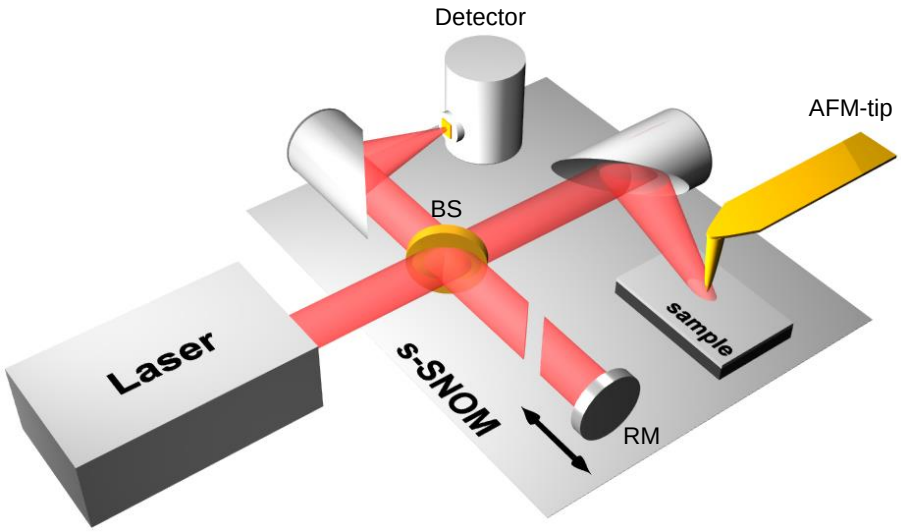

Fig. 4.5 Interferometric detection in s-SNOM. The metallic AFM-tip is illuminated with a focused laser beam. The backscattered light is analyzed with a Michelson interferometer, comprising a beamsplitter (BS), a reference mirror (RM) and a detector.

The experimental setup for pseudo-heterodyne detection is shown in Fig. 4.5. The tip-illuminating laser beam is split by a beamsplitter (BS) in two equal parts. The transmitted part is focused on the tip by a parabolic mirror. The same parabolic mirror collects the backscattered light from where it propagates back to the beamsplitter. At the beamsplitter, it is combined with the reference beam that is back reflected from the planar reference mirror (RM). The interference of the tip-scattered field and the reference field is measured at the detector, according to

$$I_{\mathrm{det}} = I_{\mathrm{s}} \propto |E_{\mathrm{sca}} + E_{\mathrm{ref}}|^2 = \left(E_{\mathrm{nf}} + E_{\mathrm{bg}} + E_{\mathrm{ref}}\right)\left(E_{\mathrm{nf}} + E_{\mathrm{bg}} + E_{\mathrm{ref}}\right)^* \qquad (4.6)$$

where E_{ref} is the electric field of the reference beam. As described in section 4.3.3, the probing tip oscillates vertically with a frequency Ω, causing the backscattered light from the tip ($E_{\mathrm{nf}} + E_{\mathrm{bg}}$) to be modulated at the frequency Ω (typically around Ω ≈ 250 kHz) and its higher harmonics nΩ (with n being an integer >1). For the pseudo-heterodyne detection, the position of the reference mirror is modulated sinusoidally in direction of the beam propagation, yielding a phase modulation of the reference beam. The modulation frequency M is chosen to be much lower than the tip vibration frequency (typically around M ≈ 300 Hz). Due to the interference of the scattered light E_{sca} with the phase modulated reference beam E_{ref}, the signal at the detector has a frequency spectrum as illustrated in Fig. 4.6

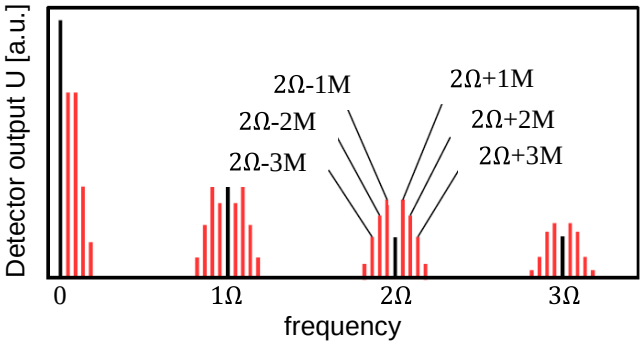

Fig. 4.6 Signal splitting in pseudo-heterodyne detection in s-SNOM. The metallic AFM-tip is oscillating with a frequency Ω, and the reference mirror with a frequency M (M ≪ Ω), causing the interferometric signal to split up in sidebands nΩ ± mM. (Image taken from[60])

As the tip oscillation frequency Ω is much higher than the phase modulation frequency M, the sum- and difference frequencies appear as sidebands around the tip oscillation frequency Ω and its higher harmonics nΩ at the spectral positions nΩ ± mM. These sidebands are shown in red in Fig. 4.6.

According to (refs.[60,91]), background-free near-field amplitude $s_{\mathrm{nf,n}}$ and phase $\varphi_{\mathrm{nf,n}}$ can then be reconstructed from the detector-signal $U_{\mathrm{n,1}}$ measured at the first sideband (at the frequency nΩ + 1M) and the signal $U_{\mathrm{n,2}}$, measured at the second sideband (at the frequency nΩ + 2M) for sufficiently high demodulating order n > 1, according to

$$s_{\mathrm{nf,n}} = 2.16k\sqrt{U_{\mathrm{n},1}^2 + U_{\mathrm{n},2}^2} \tag{4.7}$$

and

$$\varphi_{\mathrm{nf,n}} = \arctan\left(2.16k\frac{U_{\mathrm{n},2}}{U_{\mathrm{n},1}}\right), \tag{4.8}$$

with k being a proportionality constant. Note that this mathematical relationships require the modulation amplitude of the reference mirror to be set to 0.21λ (ref.[91]), with λ being the wavelength of illumination. Therefore this detection scheme is only applicable for monochromatic illumination of the tip.

Another interesting consequence arises when looking at eq. (4.6). If the reference field E_{ref} is much stronger than the back-scattered field from the tip, E_{sca}, the interference leads to a significant signal enhancement. This interferometric gain will be described in more detail in chapter 6.

4.3.4 Local Spectroscopy with Tunable Single-Line Lasers

In the previous sections, methods to measure the background-free near-field response for single-frequency illumination of the probing tip have been introduced. To obtain spectral information about the sample, that is the amplitude and phase of the near-field signal for many different wavelengths λ, the sample has to be imaged sequentially at various wavelengths from tunable laser sources[13,20,25,26]. The set of near-field images yields the wavelength-dependent dielectric sample properties, from which local chemical composition or conductivity can be determined[18,27]. Using s-SNOM, nanoscale infrared imaging and spectroscopy of molecular vibrations in the 6 µm wavelength region has been successfully demonstrated with polymer and protein nanostructures[13,14,92,93], including single viruses[18] and fibrils[19]. In these experiments, the illumination of the tip was provided by tunable CO gas lasers.

4.3.5 Local Spectroscopy with Broadband Sources

For chemical identification of unknown nanostructures, however, the acquisition of local near-field spectra in a broad spectral range spanning from near- to far-infrared

frequencies is needed. Continuous near-field spectroscopy has been recently demonstrated using mid-infrared frequency combs[94,95], but only relatively narrowband infrared radiation was available with this technique. In another approach, the tip was used to scatter the infrared near fields at the surface of a heated sample, yielding a thermal image of the sample surface[96]. Alternatively, a heated tip could be used for local infrared sample illumination[97]. In this thesis, continuous broadband near-field spectroscopy has been realized with a thermal source and a novel broadband laser system, which will be presented in chapter 6 and 7, respectively.

4.4 Theory of s-SNOM

Several theoretical models have been introduced to describe the near-field interaction between the tip and sample. In order to obtain an experimentally measurable quantity, they define the near-field scattering coefficient σ_{nf} that relates the light backscattered from the tip E_{sca} with the incoming light E_{in}, according to

$$E_{\mathrm{sca}} = \sigma_{\mathrm{nf}} E_{\mathrm{in}}. \tag{4.9}$$

The models relate the complex valued near-field scattering coefficient $\sigma_{\mathrm{nf}} = s_{\mathrm{nf}} e^{i\varphi_{\mathrm{nf}}}$ (with the near-field amplitude s_{nf} and the near-field phase φ_{nf}) to the dielectric properties of the sample in order to explain the experimentally acquired data. The theoretical models are discussed in great detail in ref.[60]. In this section a summary of the most important concepts and results will be given.

4.4.1 Dipole Model

The dipole model is illustrated in Fig. 4.7. The metallic AFM-tip is approximated by a metal sphere with radius R, which is placed at the distance H to a sample surface. The sample surface is modeled by a semi-infinite half-space, characterized by its dielectric function ϵ_{s}.

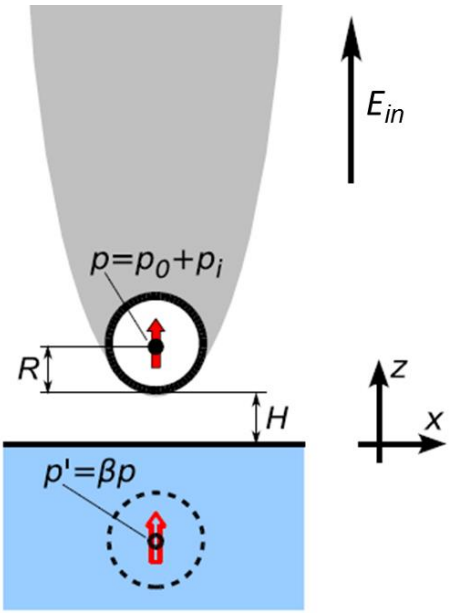

Fig. 4.7 Dipole model for s-SNOM. The incident electric field E_{in}creates a dipole p in the metallic AFM-tip, which is described by a sphere. The near-field interaction with the sample is described with a mirror dipole p'. Image taken from (ref.[60]).

Due to the incident electric field E_{in} (the tip illumination), the sphere gets polarized. This can be described by a simple point dipole, sitting in the center of the sphere, having an initial dipole moment

$$p_0 = \alpha E_{\text{in}} \tag{4.10}$$

where *a* describes the polarizability of the sphere as

$$\alpha = 4\pi R^3 \frac{\epsilon_t - 1}{\epsilon_t + 2} \text{ (in air).} \tag{4.11}$$

ϵ_t denotes the dielectric function of the tip, which, in case of a metallic tip, is a constant close to 1 for the near- to far-infrared spectral region. Due to the elongated shape of the tip and considering p-polarized incident illumination, the dipole is assumed to be oriented along the tip-axis, defined as z-direction. This dipole, situated close to a sample surface, now polarizes the sample, thereby creating a mirror dipole

$$p' = \beta p_0 \tag{4.12}$$

where $\beta = (\epsilon_s - 1)/(\epsilon_s + 1)$ is the so-called surface response function, which depends on ϵ_s, the local dielectric function of the sample. The mirror dipole acts back on the probe, thereby polarizing it even stronger. This additional probing dipole moment increases the strength of the mirror dipole, which in turn induces further polarization of the tip, and so on, representing the near-field interaction between tip and sample. Through this interaction, the total mirror dipole strength gets

$$p' = \beta(p_0 + p_i) \tag{4.13}$$

with p_i being the interaction-induced part, which is induced by p' according to

$$p_i = f p' \tag{4.14}$$

where f is a function of the distance between the tip and the sample. Inserting eq. (4.13) into eq. (4.14), we obtain $p_i = \beta f(p_0 + p_i)$. With the substitutions $p_i = p - p_0$ and $\beta f = g$ we get $p = p_0 + gp$ or

$$p = \frac{p_0}{1 - g} \tag{4.15}$$

If the separation of the point dipole and its mirror image is $D = 2(R + H)$, the field produced by the mirror dipole p' at the position of the tip dipole p is equal to

$$E = \frac{p'}{2\pi D^3} \tag{4.16}$$

The field E induces a dipole moment $p_\mathrm{i} = \alpha E$ in the tip. Inserting p_i and eq. (4.16) in equation (4.14) we get

$$f = \frac{p_\mathrm{i}}{p'} = \frac{\alpha}{2\pi D^3} \tag{4.17}$$

With $D = 2(R + H)$ and $g = \beta f = \beta\alpha/16\pi(R + H)^3$ we obtain the final solution for the tip dipole moment

$$p = E_\mathrm{in} \frac{\alpha}{1 - \frac{\alpha\beta}{16\pi(R+H)^3}} \tag{4.18}$$

Instead of the dipole moment, it is customary to use the effective polarizability $\alpha_\mathrm{eff} = p/E_\mathrm{in}$, which can be easily derived now from eq. (4.18):

$$\alpha_\mathrm{eff} = \frac{\alpha}{1 - \frac{\alpha\beta}{16\pi(R+H)^3}} \tag{4.19}$$

As introduced in the beginning of this chapter, the near-field scattering coefficient σ_nf is defined as the ratio between the light backscattered from the tip E_sca and the incoming light E_in as $\sigma_\mathrm{nf} = E_\mathrm{sca}/E_\mathrm{in}$. Because the near-field scattering coefficient σ_nf is proportional to the dipole moment p of the coupled tip-sample system and thus to the effective polarizability of the tip, we obtain the following relation $\alpha_\mathrm{eff} \propto \sigma_\mathrm{nf} = s_\mathrm{nf} e^{i\varphi_\mathrm{nf}}$. To take into account the tip-oscillation and the higher-harmonic signal demodulation, we calculate the time course of $\alpha_\mathrm{eff} = \alpha_\mathrm{eff}[h(t)]$ with $h(t) = A(1 + \cos(\Omega t)$. By Fourier analysis of $\alpha_\mathrm{eff}[h(t)]$ we obtain the Fourier coefficients $\alpha_\mathrm{eff,n}$, where $\alpha_\mathrm{eff,n}$ is the n-th Fourier coefficient, corresponding to the n-th demodulation order with respect to Ω. From $\alpha_\mathrm{eff,n}$ we obtain the amplitude $s_\mathrm{nf,n}$ and phase $\varphi_\mathrm{nf,n}$ of the n-th demodulation order as

$$s_\mathrm{nf,n} \propto \left|\alpha_\mathrm{eff,n}\right| \tag{4.20}$$

and

$$\varphi_\mathrm{nf,n} = \arg(\alpha_\mathrm{eff,n}). \tag{4.21}$$

4.4.2 Finite Dipole Model

When comparing the predictions of the dipole model with experimental data, the agreement turns out to be good only for samples exhibiting weak resonances. For strong resonances, such as phonon- or plasmon-polaritons, some discrepancy can be observed[20]. To overcome these constraints, the so-called finite-dipole model has been developed[60]. Instead of describing the tip by a sphere, it is described by a spheroid with length $2L$ in order to take into account that the tip in the experiment is elongated. The field in the proximity of such a spheroid is described by an extended or finite dipole, rather than a point-dipole. In Fig. 4.8, both the dipole and the finite dipole model are illustrated.

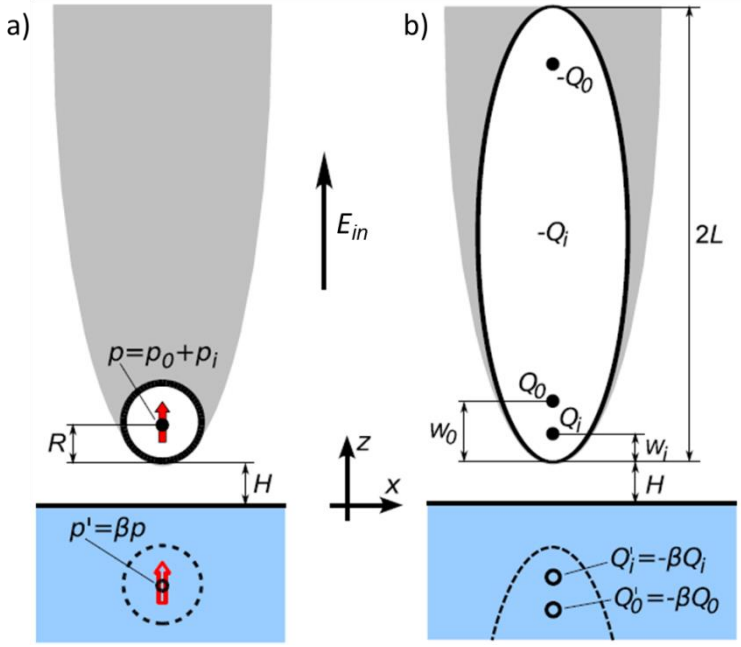

Fig. 4.8 Comparison of the point dipole model (a) and the finite dipole model (b). The point dipole model uses a point dipole to describe the s-SNOM probe, which is assumed to be a sphere. The finite dipole model describes the tip as an elongated spheroid, and its polarization due to the external illumination is described by a finite dipole, i.e. two discrete charges Q_0 and $-Q_0$ with finite separation. Only the charge Q_0 which is closer to the sample surface is assumed to contribute to the near-field interaction. (image taken from[60])

The incident field E_{in} induces two charges Q_0 and $-Q_0$ in the (spheroidal) tip, as illustrated in Fig. 4.8b. From these two charges only Q_0 (which is closer to the sample surface) participates in the near-field interaction. The initial dipole moment of the

spheroid then can be written as $p_0 = 2LQ_0$. When the tip comes close to a sample surface, an image charge $Q_0' = -\beta Q_0$ is induced in the sample. The image charge Q_0' acts back on the spheroid, where it induces an additional point charge Q_i close to the tip apex, whereas the opposite charge $-Q_i$ is distributed along the spheroid. The charge Q_i in turn induces an image point charge Q_i' in the sample, which again can be described using the surface response function β as $Q_\mathrm{i}' = \beta Q_\mathrm{i}$. Note that in the finite dipole model Q_0 is determined by the incident field and the geometry of the spheroid only, whereas Q_i and Q_i' are determined by the dielectric properties of the sample.

Similar to the dipole model, the finite-dipole model defines an effective dipole moment for the spheroid as $p_\mathrm{eff} = p_0 + p_\mathrm{i}$, where p_0 is the initial dipole moment caused by the external field, while p_i reflects the dipole moment induced by the tip-sample near-field interaction. The latter is given by $p_\mathrm{i} = Q_\mathrm{i}L$, where L is the effective length of the spheroid. According to [ref.[60]], the effective polarizability for the coupled tip-sample-system can be expressed as

$$\alpha_\mathrm{eff} = R^2 L \frac{\frac{2L}{R} + \ln\left(\frac{R}{4eL}\right)}{\ln\left(\frac{R}{4eL}\right)} \left(2 + \frac{\beta\left(g - \frac{R+h}{L}\right)\ln\left(\frac{4L}{4h+3R}\right)}{\ln\left(\frac{4L}{R}\right) - \beta\left(g - \frac{3R+4h}{4L}\right)\ln\left(\frac{2L}{2h+R}\right)}\right). \tag{4.22}$$

This solution for α_eff requires five parameters:

- h, the tip-sample distance. This value is taken from the experiment (tapping amplitude).
- β, the surface response function of the sample, which is derived from the dielectric function $\epsilon(\omega)$ of the sample.
- R, the tip radius. This value is usually between 10 nm and 50 nm, as specified by the manufacturer of the tip.
- L, the effective length of the spheroid.
- g, a complex factor describing the total charge induced in the spheroid.

The last two parameters, L and g, are determined by searching for the best agreement between experimental and calculated data. Values that give a reasonable agreement are

L = 600 nm, and $g = 0.7e^{0.06i}$ (ref.[60]). Analogous to the dipole model we can calculate the amplitude $s_{\mathrm{nf,n}}$ and phase $\varphi_{\mathrm{nf,n}}$ of the n-th demodulation order from $\alpha_{\mathrm{eff,n}}$ as

$$s_{\mathrm{nf,n}} \propto \left|\alpha_{\mathrm{eff,n}}\right| \tag{4.23}$$

and

$$\varphi_{\mathrm{nf,n}} = \arg(\alpha_{\mathrm{eff,n}}). \tag{4.24}$$

5 Nanoscale Infrared Near-Field Spectroscopy (nano-FTIR)

This chapter describes a novel microscopy and spectroscopy system, which was developed and experimentally realized in the course of this thesis. It combines the analytical power of Fourier transform infrared spectroscopy (FTIR, chapter 3) with the nanoscale spatial resolution of s-SNOM (chapter 4). Hence it was given the name nano-FTIR.

5.1 Working Principle

To obtain broadband spectral information, nano-FTIR extends the s-SNOM principle by using a broadband infrared source for tip illumination. FTIR spectroscopy of the backscattered light is performed, while the tip is in contact with the sample at a specific sample position. By a linear movement of the reference mirror (analogous to FTIR, see section 3.3) in combination with higher harmonic demodulation (as used in s-SNOM for background suppression, see section 4.3.3), a near-field interferogram can be recorded. Because the tip-sample system is located in one of the interferometer arms, the Fourier transformation of this interferogram yields the near-field amplitude $s_{\mathrm{nf,n}}(\omega)$ and near-field phase spectrum $\varphi_{\mathrm{nf,n}}(\omega)$ of the measured sample spot.

5.2 Experimental Implementation

The nano-FTIR setup is illustrated in Fig. 5.1. It is based on a commercial s-SNOM (www.neaspec.com), which comprises an AFM, the tip illumination optics and all electronics necessary for data recording and processing. A broadband light source illuminates the metallic AFM-tip of the near-field microscope. For illumination as well as for collection a parabolic mirror is used, in order to avoid chromatic aberrations. The tip-scattered light is analyzed with a Michelson-type interferometer. To implement the interferometer, a ZnSe beamsplitter (BS, Fig. 5.1) was positioned very close to the probing tip and a reference mirror (RM, Fig. 5.1) is placed on a Piezo-driven Linear Stage, which can travel up to 1500 µm in closed-loop operation. It has a high linearity

(0.03) and a position resolution of < 3 nm, which is important for high performance Fourier analysis. The Piezo Stage is mounted on a manual high-stability micrometer-stage with cross-roll bearings, which has a travel range of 25 mm. This is required to adjust the white light position (WLP, details in section 3.3).

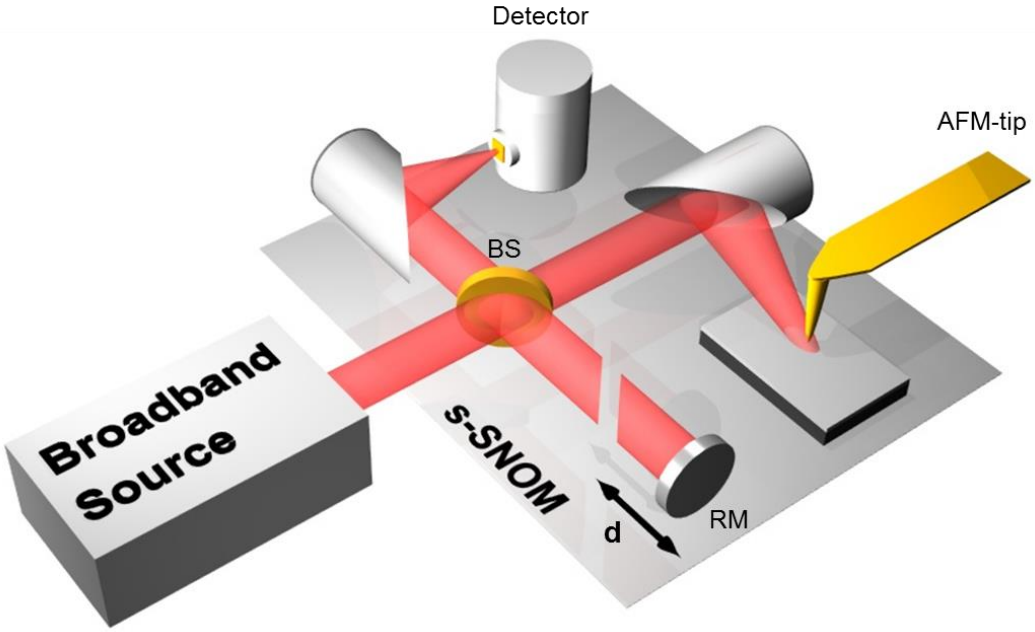

Fig. 5.1 Schematic nano-FTIR Setup. The metallic tip of a near-field microscope (s-SNOM) is illuminated with a broadband source. The backscattered light is analyzed with a Michelson-type interferometer, comprising a beamsplitter, reference mirror and detector.

The light exiting the interferometer is focused to the detector with a second parabolic mirror. The signal detection is done with a liquid nitrogen (LN_2) cooled mercury cadmium telluride (MCT) detector. It has a very high sensitivity and low noise ($D^* > 10^{10}$) with a bandwidth > 1 MHz, as typical tip oscillation frequencies are in the range of 10 – 300 kHz. The detector signal is demodulated at higher harmonics nΩ of the tip oscillation amplitude Ω and recorded as a function of the mirror position d, generating an interferogram $I_n(d)$. Subsequent Fourier Transformation of $I_n(d)$ yields the spectrum of the backscattered light $S_n(\omega)$.

Asymmetric FTIR Spectrometer

In contrast to conventional FTIR, the sample (together with the tip) is located in one of

the interferometer arms while the reference beam is reflected at a planar mirror (see Fig. 5.1). Such a detection scheme is called asymmetric FTIR spectroscopy and offers two important advantages. First, a strong signal enhancement can be achieved due to interferometric gain, as the scattered power of nanoscale objects (here: the probing tip) is very weak compared to the illumination power. Because of the interference between the tip-scattered radiation and the much stronger reference beam, the detected power is $P_{\mathrm{det}} \propto \sqrt{P_{\mathrm{ref}} P_{\mathrm{sca}}}$ rather than the scattered power P_{sca}, resulting in a signal enhancement by several orders of magnitude[29] (for details see chapter 3.2 and 6). Second, the optical phase can be measured with an asymmetric FTIR spectrometer. As will be described in detail in chapter 0, the possibility of measuring the amplitude *and* the phase of the tip-scattered light allows to measure *local* absorption and in principle a full reconstruction of the *local* complex dielectric function $\epsilon(\omega)$ of the sample can be done[98].

5.3 Background Suppression in nano-FTIR

As in s-SNOM, the (polychromatic) illumination spot is diffraction limited, resulting in unavoidable background scattering off the tip shaft and neighboring sample regions. To suppress the background contribution, higher harmonic demodulation is used, as described in chapter 5.2.According to ref.[60] and eq. (4.5), the (complex valued) signal at the n-th harmonic is given in good approximation by

$$U_{\mathrm{n}} \propto s_{\mathrm{nf,n}}\left[s_{\mathrm{bg,0}}\, cos\left(\varphi_{\mathrm{nf,n}} - \varphi_{\mathrm{bg,0}}\right) + s_{\mathrm{ref}}\, cos\left(\varphi_{\mathrm{nf,n}} - \varphi_{\mathrm{ref}}\right)\right], \tag{5.1}$$

with s and φ being the amplitude and phase of the near-field (index nf), background (index bg) and reference (index ref), respectively. Translating the reference mirror from an initial start-position ($d = 0$) to an end-position ($d = d_{\mathrm{max}}$) in small steps $\mathrm{d}d$ yields the interferogram $U_{\mathrm{n}}(d)$. Considering that $\varphi_{\mathrm{ref}} = 2\pi\omega d$, Fourier Transformation of $U_{\mathrm{n}}(d)$ gives the spectrum $S_{\mathrm{n}}(\omega)$ according to

$$S_{\mathrm{n}}(\omega) = \int_0^{\infty} s_{\mathrm{nf,n}}\left[s_{\mathrm{bg,0}}\, cos\left(\varphi_{\mathrm{nf,n}} - \varphi_{\mathrm{bg,0}}\right) + s_{\mathrm{ref}}\, cos\left(\varphi_{\mathrm{nf,n}} - 2\pi\omega d\right)\right] e^{i2\pi\omega d}\mathrm{d}d. \tag{5.2}$$

The first term contains background contributions but does not depend on d, and thus does not yield spectral components for $\omega > 0$. The second term depends on d, but does not contain background contributions. It thus yields the background-free complex-valued near-field spectrum $S_{\mathrm{n}}(\omega) \propto s_{\mathrm{nf,n}}(\omega)\, e^{i\varphi_{\mathrm{nf,n}}(\omega)}$ for signal demodulation at a sufficiently high harmonic $\mathrm{n}\Omega$ of the tip oscillation amplitude Ω.

5.4 Normalization in nano-FTIR

As in conventional FTIR, the nano-FTIR spectrum needs to be normalized to a background spectrum to eliminate the influence of the instrumental characteristics on a measured sample spectrum. However, the procedure to obtain a background spectrum is slightly different in nano-FTIR.

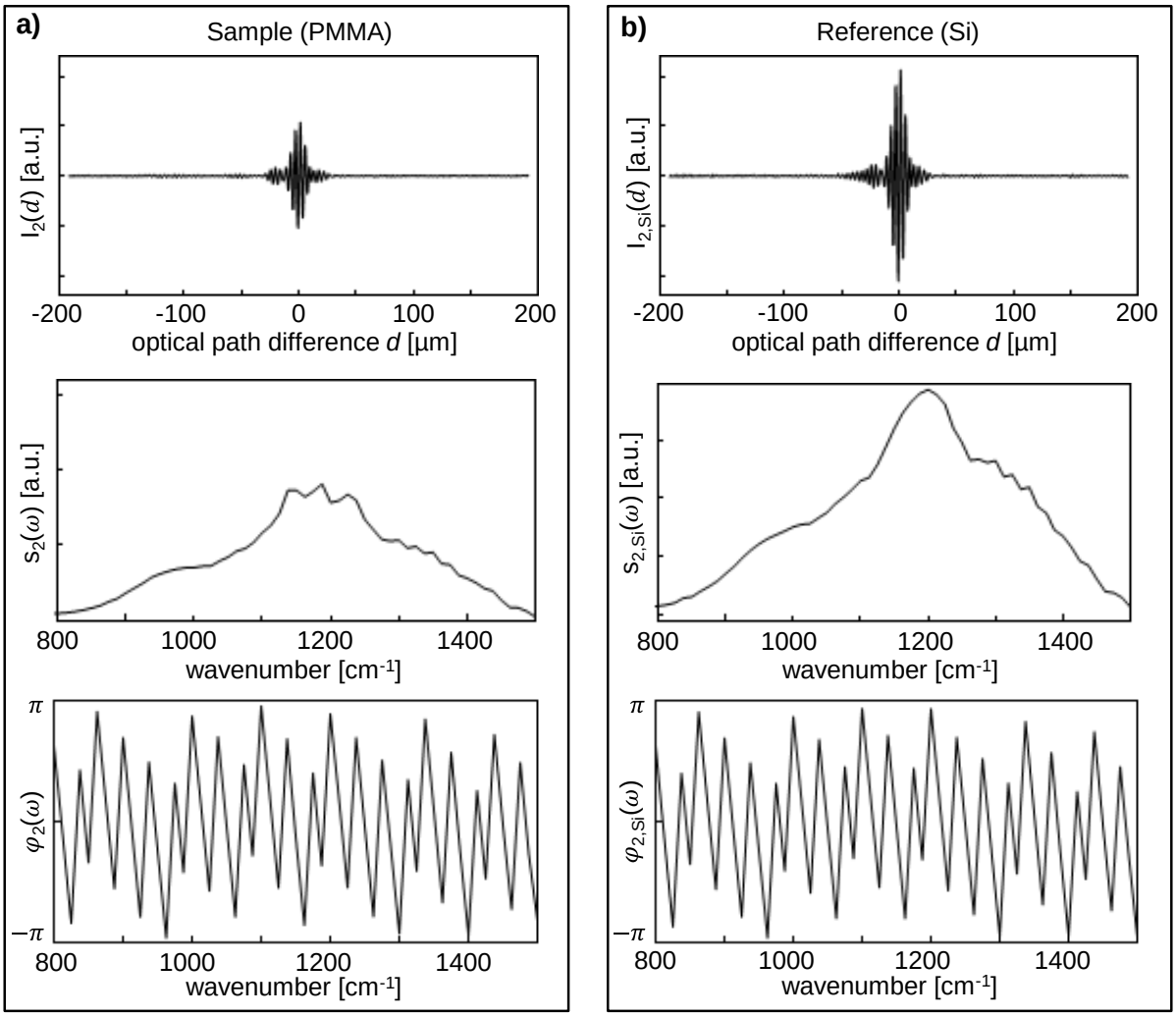

Fig. 5.2 nano-FTIR measurements of a PMMA sample and a Si substrate. Interferogram and resulting amplitude (s_n) and phase (φ_n) spectra are shown. Each interferogram is an average of 10 single scans, each taken with 1024 pixels in 80 s.

As the near-field signal arises from the tip-sample interaction, a measurement without sample is not reasonable, as it would not produce a near-field signal. Instead, in nano-FTIR the near-field spectrum of a known substrate, which ideally is spectrally flat (i.e.

has no spectral absorption peaks or other resonances, e.g. phonon-polaritons), is measured. For the mid-infrared spectral region, Si is a suitable substrate. A second interferogram (Fig. 5.2b) has been measured on a bare Si substrate with identical experimental settings (e.g. same tip, same tapping amplitude, same illumination, etc.). FT yields the reference amplitude $s_{2,\mathrm{Si}}(\omega)$ and phase $\varphi_{2,\mathrm{Si}}(\omega)$ spectrum. By normalizing the sample spectra (Fig. 5.2a) to the reference spectra (Fig. 5.2b), the normalized amplitude spectrum $s_2(\omega)/s_{2,\mathrm{Si}}(\omega)$ and the normalized phase spectrum $\varphi_2(\omega) - \varphi_{2,\mathrm{Si}}(\omega)$ of the sample are obtained (see Fig. 5.3)

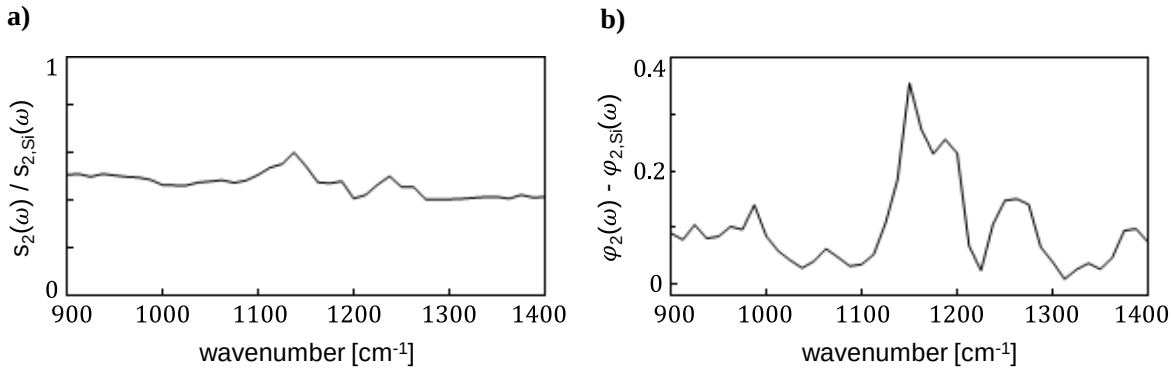

Fig. 5.3 Normalized amplitude $s_2(\omega)/s_{2,\mathrm{Si}}(\omega)$ (a) and phase $\varphi_2(\omega) - \varphi_{2,\mathrm{Si}}(\omega)$ (b) spectra of a PMMA sample.

It should be noted that the interferogram, which is obtained by recording the demodulated detector signal as a function of the mirror position (eq. (5.1)), is complex-valued, as it records the output of a (software-based) lock-in amplifier used for the demodulation. What is shown in Fig. 5.2a and b is the real part of this complex-valued interferogram. For the Fourier Transformation, however, the complex valued interferogram is considered, returning a complex-valued spectrum, which can then be split in amplitude and phase spectra (as shown in see Fig. 5.3)

5.5 Apodization and Zero-Filling

As in conventional FTIR, the interferograms measured in *nano-FTIR* are processed by discrete Fourier Transformation. Apodization and Zero-filling is applied as described in chapter 3.3.4. To illustrate this, the spectra from Fig. 5.3 have been apodized by a

Gaussian apodization function and extended by a factor 8 by zero-filling. The resulting normalized amplitude and phase spectra are shown in Fig. 5.4.

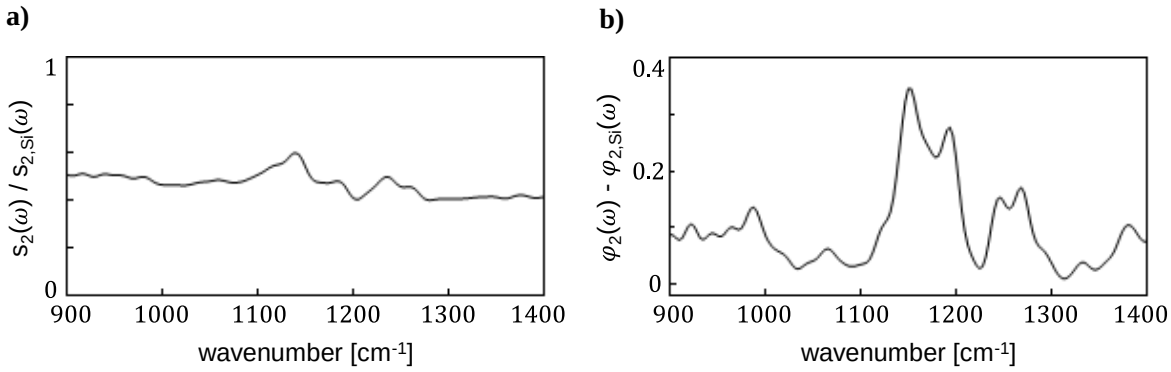

Fig. 5.4 Normalized Spectra from Fig. 5.3 after apodization and zero-filling.

5.6 Definition of nano-FTIR Absorption

In the course of this thesis, it could be demonstrated that the (complex) measurement of broadband infrared near-field spectra gives access to the local infrared absorption. Therefore, the nano-FTIR absorption was defined as

$$a_{\mathrm{n}}(\omega) = Im[\eta_{\mathrm{n}}(\omega)] = Im\left[\frac{\sigma_{\mathrm{n}}(\omega)}{\sigma_{\mathrm{n,ref}}(\omega)}\right], \tag{5.3}$$

the imaginary part of the normalized near-field spectrum $\eta_{\mathrm{n}}(\omega)$. The imaginary part can be easily calculated from the amplitude and phase spectra, according to

$$Im[\eta_{\mathrm{n}}(\omega)] = \frac{s_{\mathrm{n}}(\omega)}{s_{\mathrm{n,ref}}(\omega)} \sin\Big(\varphi_{\mathrm{n}}(\omega) - \varphi_{\mathrm{n,ref}}(\omega)\Big), \tag{5.4}$$

A comprehensive derivation of this relation is presented in chapter 7.4 of this thesis.

6 Nano-FTIR Spectroscopy with a Thermal Source

In its first experimental realization, the nano-FTIR system was implemented with a thermal light source, similar to what is used in conventional FTIR spectroscopy. With this setup we succeeded in nanoscale infrared near-field imaging of a semiconductor device within a few minutes, as well as in mapping of local infrared spectra with a spatial resolution better than 100 nm.

6.1 Experimental Setup

Our setup is depicted in Fig. 6.1a. As already introduced in chapter 4.3.2, a parabolic metal mirror is used for illuminating an AFM tip, as well as for the collection of the backscattered light.

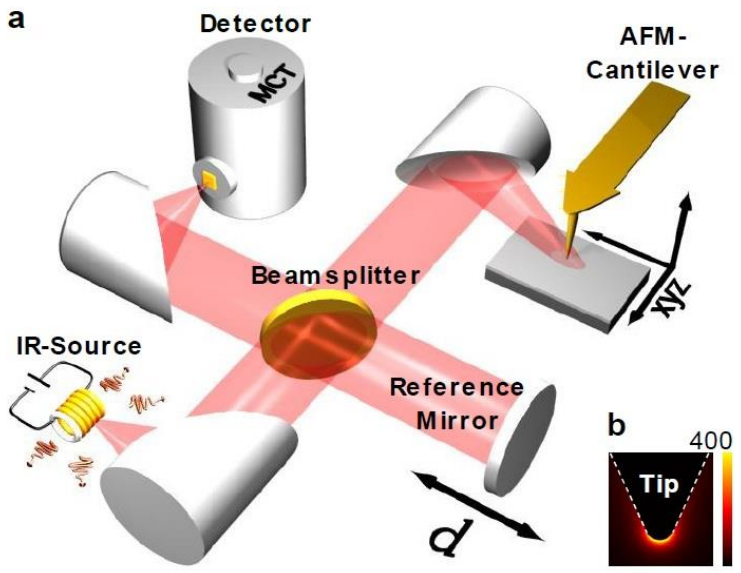

Fig. 6.1 Near-field spectroscopy with a thermal source. **a)** Experimental Setup. **b)** Numerical calculation showing the field distribution at the apex of a metal tip (10 µm long, 100 nm apex diameter), which is illuminated with infrared radiation of 10.7 µm wavelength.

Standard AFM tips with gold coating are used as antennas[5,32,99] for nano-focusing of thermal radiation. The antenna function of the metal tip is illustrated with a numerical calculation of the near-field distribution of a metal cone with 100 nm apex diameter

(Fig. 6.1b). It shows the concentrated near-field spot at the tip apex, where the intensity is enhanced by a factor of 400 compared to the incident radiation.

To perform broadband infrared near-field spectroscopy, we implemented a Fourier transform (FT) spectrometer that uses a heated coil (SA10510-88, www.lasercomponents.com) as infrared light source. A simulated emission spectrum of such a source is shown in Fig. 3.6. A major challenge in this case are the extremely weak near-field signals. According to the Stefan-Boltzmann law and the second law of thermodynamics, a thermal light source with a temperature of 1000 K provides a maximum power density of about 6 W/cm^2 (in case of blackbody emission) at a distant sample surface[2]. In a narrow spectral window of $\Delta\omega = 1\ \mathrm{cm}^{-1}$, the power density is less than $I_S = 10^{-2}\ \mathrm{W/cm^2}$. It is thus several orders of magnitude lower than in former s-SNOM experiments using infrared lasers where the power density was $I_S > 10^2\ \mathrm{W/cm^2}$ (refs.[14,15,100,101], achieved by focusing 1mW laser radiation to a spot of 10 µm diameter).

In contrast to conventional FTIR, the sample (together with the tip) is located in one of the interferometer arms while the reference beam is reflected at a planar mirror. Such a detection scheme is called asymmetric FTIR spectroscopy[28]. Because of the interference between the tip-scattered radiation and the reference beam, we detect the power $P_{\mathrm{det}} \propto \sqrt{P_{\mathrm{ref}} P_{\mathrm{sca}}}$ rather than the scattered power P_{sca}. This important detail offers the advantage of a strong signal enhancement, which we illustrate with a simple calculation. In our experiment the reference beam has a power of about $P_{\mathrm{ref}} = 15\ \mu\mathrm{W}$. In case of optimal interferometer adjustment, a scattered power of $P_{\mathrm{sca}} = 200\ \mathrm{fW}$ (for example the infrared scattering of a 100 nm diameter metal sphere, which is illuminated with 1000 K blackbody thermal radiation) yields a signal $P_{\mathrm{det}} = 1.7\ \mathrm{nW}$. The detector signal P_{det} is thus enhanced by a factor of about 10^4 compared to P_{sca}. This signal enhancement is even stronger than the intensity enhancement provided by the tip, and thus an essential feature to push the sensitivity in FTIR near-field spectroscopy.

Similar to conventional FTIR, as described in detail in chapter 3.3, *nano-FTIR* needs to measure the system-characteristics to be able to extract the pure sample response. In Fig. 6.2a we show the interferogram $I_{2,\mathrm{Si}}(d)$ obtained on a Si surface at demodulation order n = 2, yielding a near-field spectrum $s_{2,\mathrm{Si}}(\omega)$ (Fig. 6.2b). Because of the nearly constant dielectric function of Si in the mid-infrared spectral range, $s_{2,\mathrm{Si}}(\omega)$ yields the

spectral characteristics of our setup including emission properties of the thermal source, transmission of the beamsplitter and responsivity of the infrared detector. We can thus use $s_{2,\mathrm{Si}}(\omega)$ as a reference spectrum for the following experiments.

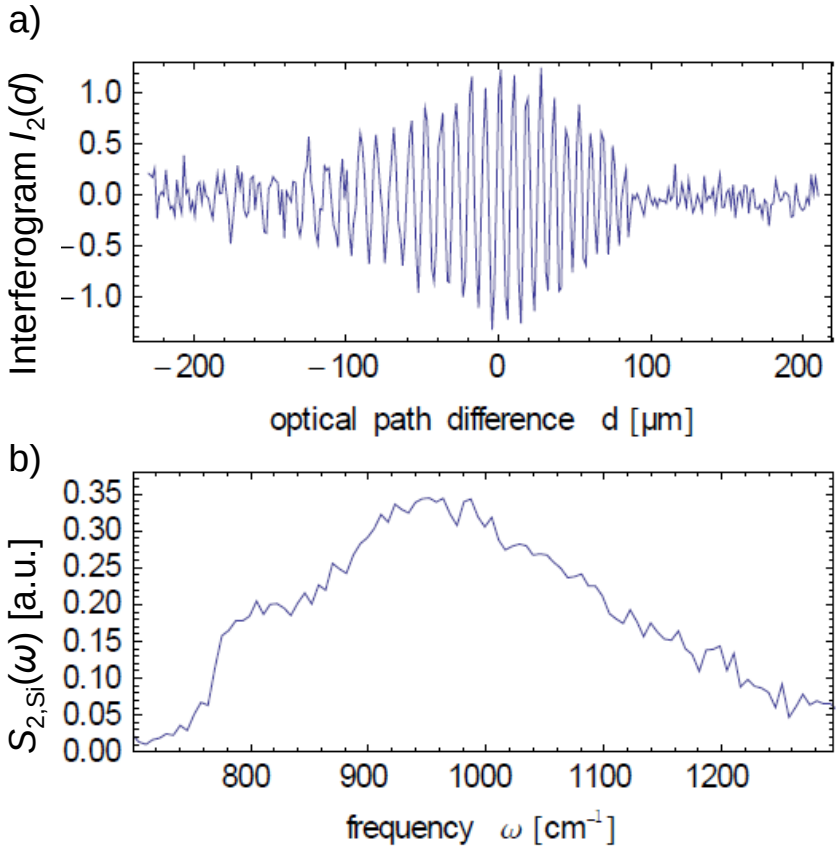

Fig. 6.2 Nano-FTIR with a thermal source. a) Interferogram $I_{2,\mathrm{Si}}(d)$ recorded on a Si surface. b) Near-field spectrum $s_{2,\mathrm{Si}}(\omega)$ of Si obtained by Fourier-transformation of $I_{2,\mathrm{Si}}(d)$ shown in (a). It should be noted that the interferogram appears broader compared to other data presented in this thesis, because the interferometer in this setup was not dispersion-corrected.

6.2 Nano-Imaging and Spectroscopy with Thermal Radiation

Nanoscale focusing of thermal radiation is validated by high-resolution near-field imaging of a state-of-the-art semiconductor device (provided by Infineon Technologies, Munich). The reference mirror is kept fixed at a position $d \approx 0$ (white light position), where the simultaneous interference of all spectral components maximizes the near-field signal $I_2(d \approx 0)$. The detector signal thus yields the spectrally integrated signal $I_{\mathrm{n}} = \int_0^\infty \left|Re\left(\sigma_{\mathrm{n}}(\omega)\right)\right|$, where $\sigma_{\mathrm{n}}(\omega)$ is the complex s-SNOM signal at frequency ω, and is proportional to the intensity of the incident light $I_{\mathrm{inc}}(\omega)$ and the spectral responsivity

$R(\omega)$ of the setup including beamsplitter and detector. Fig. 6.3a shows the topography and Fig. 6.3b the simultaneously acquired infrared near-field image of a mechanically polished cross section, consisting of a highly p-doped poly-Si layer (center) between two SiO_2 layers, which are embedded in a Si substrate. We note that the 100 x 100 pixel images were taken within less than 10 minutes and with 40 ms integration time per pixel. The topography image shows only slight height variations of about 20 nm, caused by differently strong material removal during the polishing process.

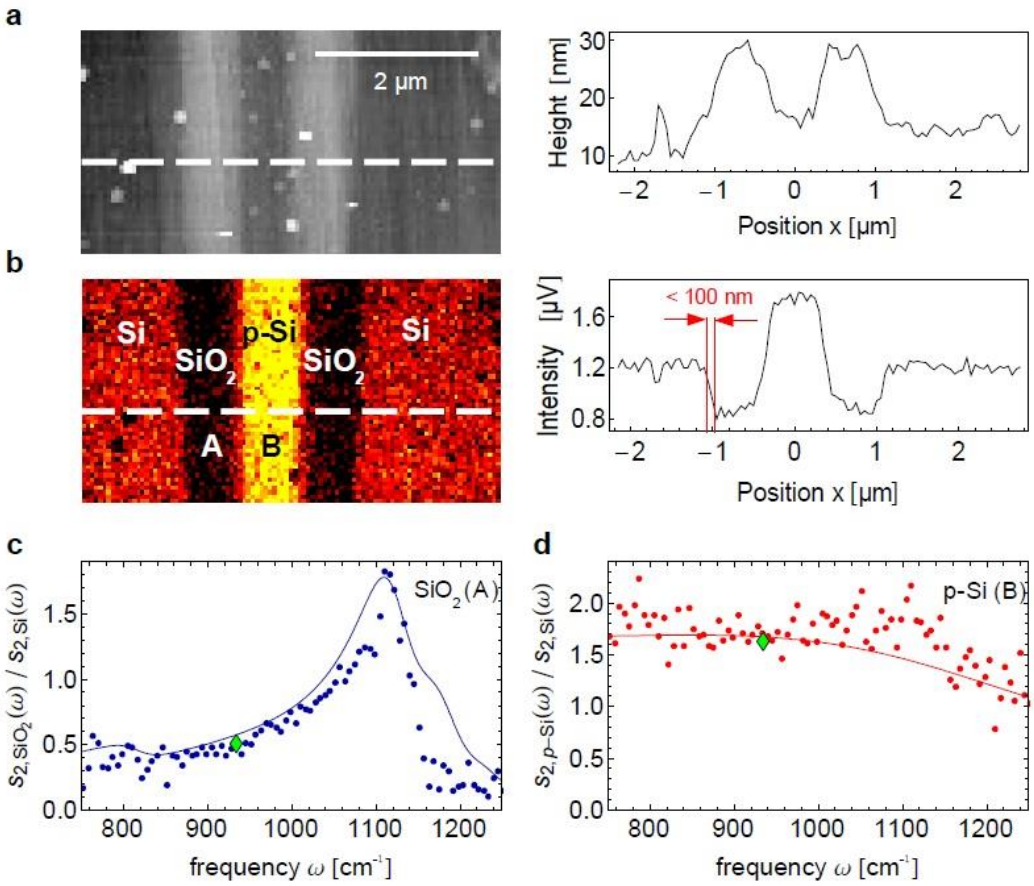

Fig. 6.3 Nano-imaging and spectroscopy of a polished cross-section of a semiconductor device with a thermal source. **a)** Topography image and line profile (averaged over 14 horizontal lines) extracted along the dashed white line. **b)** Infrared image s_1 simultaneously acquired with topography. The reference mirror was kept fixed at a position $d \approx 0$. The line profile displays s_1 along the white dashed line (averaged over 14 horizontal lines). **c)** Near-field spectrum $s_{2,SiO_2}(\omega)$ of SiO_2 (position A in (b)) normalized to Si spectrum. **d)** Near-field spectrum $s_{2,p-Si}(\omega)$ of highly p-doped poly-Si (position B in (b)) normalized to Si. The solid lines show calculations done with the finite dipole model of s-SNOM, using a tip-radius of 50 nm and a vibration amplitude of 60 nm. The dielectric data for the calculations for SiO_2 has been taken from (ref.[102]) and for p-Si from (ref.[103]). The best agreement between calculation and experiment on the p-Si was found for a free-carrier concentration $n = 9*10^{19}$. The data points marked with green symbols represent near-field amplitude contrast extracted from a measurement with a CO_2-Laser operated at a frequency of 935 cm^{-1} (not shown).

The near-field image, on the other side, exhibits a strong material contrast between the different device components. The bright region in the center reveals the highly p-doped poly-Si structure between the two dark SiO_2-layers. We explain the weak infrared signal on the SiO_2 by its low refractive index (considering the spectral average) compared to Si. We note that there is no one-to-one correspondence between the height and the infrared signal, which excludes a topography-induced infrared image contrast[6]. While both the p-Si and the SiO_2 areas are higher than the Si substrate, they exhibit an opposite infrared contrast relative to the Si substrate (the p-Si is brighter and the SiO_2 is darker than Si). Furthermore, the infrared profile (Fig. 6.3b) exhibits a sharp signal change at the Si/SiO_2 interface (marked by the two red lines). The topography line profile (Fig. 6.3a) shows, in contrast, that the height continuously increases from position x = -1.4 μm to x = -0.8 μm. The sharp infrared signal change at the Si/SiO_2 interface thus verifies an infrared spatial resolution better than 100 nm, providing unambiguous experimental evidence that a metal tip can nano-focus blackbody radiation to a near-field spot at the tip apex of about λ/100 in diameter.

In Fig. 6.3c and d we demonstrate that continuous near-field spectra can be recorded with subwavelength-scale spatial resolution, which allows for measuring the *local* infrared "fingerprint" of a sample. We show near-field spectra $s_2(\omega)$ of SiO_2 and highly p-doped Si, which were recorded at positions A and B marked in Fig. 6.3b. The normalized SiO_2 near-field spectrum $s_{2,\mathrm{SiO_2}}(\omega)/s_{2,\mathrm{Si}}(\omega)$ reveals a sharp peak at about 1120 cm^{-1}. The peak shows the fully resolved near-field phonon-polariton response[20] of SiO_2 (refs.[95,104]), which is confirmed by a calculation using the finite-dipole model of s-SNOM[105] and dielectric data for SiO_2 from literature[102]. We obtain a near-field spectrum (solid line) in good agreement with the experimental data. Remarkably, the calculation uses as parameters just the tapping amplitude A = 60 nm and tip radius r = 50 nm, both values taken from the experiment. No fit parameter has been applied. The experimental near-field spectrum of highly p-doped poly-Si, $s_{2,\mathrm{p-Si}}(\omega)/s_{2,\mathrm{Si}}(\omega)$ (red dots in Fig. 6.3d, recorded at position B) shows a totally different signature. At frequencies below 1100 cm^{-1}, the amplitude is about 2 times larger compared to the undoped Si, revealing metallic behavior[6]. At frequencies higher than 1100 cm^{-1}, the amplitude decreases strongly. This observation can be assigned to the near-field induced plasmon response of the free carriers in the highly doped p-Si[27]. This is proven by a calculation with the

finite dipole model (red solid line), analogous to Fig. 6.3c. We use dielectric data for p-doped Si from literature[103] and the free-carrier concentration n as fit parameter. Good agreement with the experiment is obtained for n=9*10^{19} cm^{-3}, which agrees well with the nominal doping concentration. We emphasize that spectra A and B - though separated by only 500 nm (λ/20) - exhibit the pure material response of either SiO_2 (phononic) or p-Si (plasmonic), thus proving local infrared near-field spectroscopy with a subwavelength-scale resolution.

Signal-to-Noise Considerations

In our experiment the signal was detected by a MCT detector (Judson Teledyne J15D12-M204-S050U) with an average noise-equivalent power of about 0.2 pW/Hz$^{1/2}$. With this detector we achieve a signal-to-noise ratio (SNR) of 16:1 RMS, measured in the poly-Si spectrum between 850 and 1000 cm^{-1} (Fig. 6.3d). Taking into account the spectral bandwidth of 6400 cm^{-1} (0.8 µm mirror increment), the spectral resolution of $\Delta\omega = 6.3\ \mathrm{cm}^{-1}$ (800 µm total mirror movement) and a data acquisition time of 5s at each interferometer position, we obtain $\mathrm{SNR} = 0.04\Delta\omega\sqrt{t}/\sqrt{\mathrm{Hz}}$, where t is the total interferogram acquisition time. In Fig. 6.4 we show that such SNR even allows for nanoscale infrared-spectroscopic mapping, as spectra with 25 cm^{-1} spectral resolution and a SNR of 10:1 can be recorded within 2 minutes.

6.3 Infrared-Spectroscopic Mapping with Thermal Radiation

To demonstrate infrared spectroscopic mapping, we display ~90 near-field spectra (vertical axis in Fig. 6.4) recorded along the dashed white line (horizontal axis) in Fig. 6.3b. The distance Δx between the recorded near-field spectra is about 30 nm.

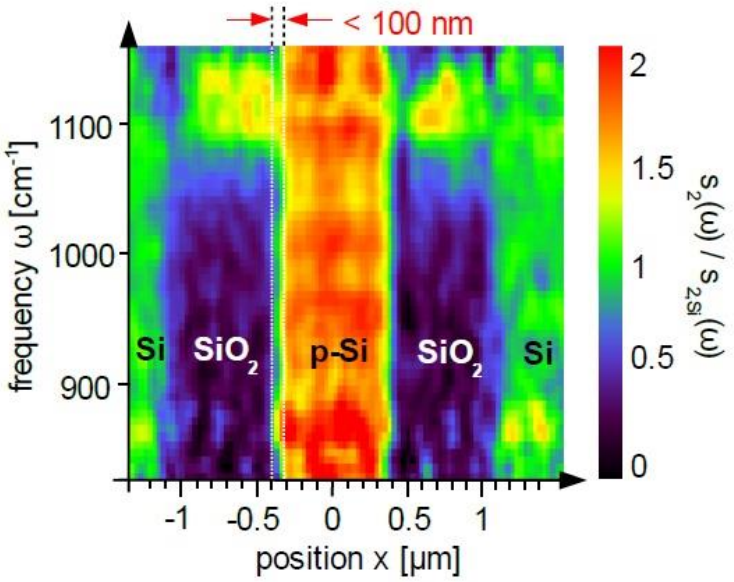

Fig. 6.4 Spectroscopic nano-imaging with a thermal source. The diagram shows infrared near-field spectra recorded along the dashed white line in Fig. 6.3b. Each of the 90 spectra was recorded in about 2 minutes and with a spectral resolution of 25 cm^{-1}.

We find that the spectral behavior dramatically changes when scanning across the interface between the different device components (positions x = -1.1 µm, -0.4 µm, 0.4 µm and 1.1 µm). The flat spectral response of Si clearly changes to that of SiO_2, exhibiting the significant phonon-polariton peak at 1120 cm^{-1} (x = -1.1 µm). The complete change from the SiO_2 to the p-doped Si spectrum occurs within 100 nm at position x = -0.4 µm (indicated by the dashed lines). From this spectral line scan we can provide first and unambiguous experimental evidence that local material properties can be accessed with nanoscale spatial resolution using broadband thermal radiation, which spectral energy density is several orders of magnitude smaller than in single-wavelength s-SNOM experiments using laser sources.

6.4 Characterization and Identification of different oxides

In the following we show that the combination of ultra-high spatial resolution and spectroscopic mapping can be applied to distinguish different oxides with dimensions on the nanometer length scale. Fig. 6.5 (left side) shows an infrared near-field image of a device cross-section containing two different silicon oxides, high-density plasma (HDP) oxide (left) and Borophosphosilicate glass (BPSG, right). The image contrast allows for distinguishing the two oxides and indicates their different dielectric properties. Taking FTIR spectra at the positions A and B marked in Fig. 6.5 (left side), we find the typical phonon peak around 1120 cm^{-1}. However, the peak positions as well as the spectral line widths differ clearly, revealing the individual IR signature of the oxides. In future applications, the infrared spectroscopic near-field signature of different oxides could be applied for process- and quality-control in semiconductor industry or to identify oxide modifications in meteorites or (bio-) minerals.

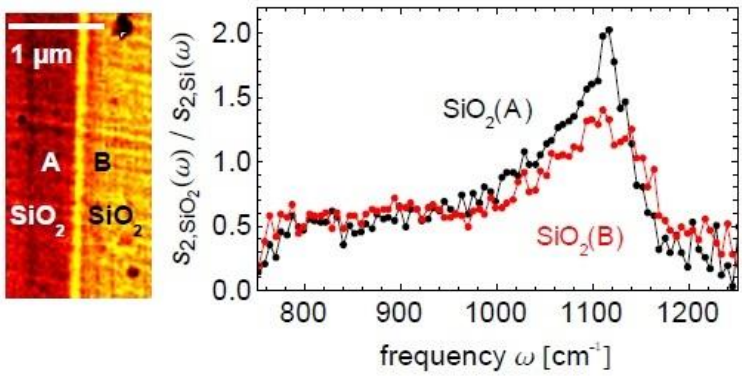

Fig. 6.5 Application of nano-FTIR for detection of chemically different Silicon Oxides. Left: Infrared near-field image of two adjacent and differently processed silicon oxides of a semiconductor device, taken with a CO2-laser at 11.3 µm wavelength. Right: FTIR near-field spectra taken at positions A and B.

6.5 Local free-carrier mapping

Another application of technological relevance is presented in Fig. 6.6. We demonstrate local conductivity measurements within a radial doping gradient, which is visualized by an infrared near-field image taken with a CO_2-laser (Fig. 6.6, left). The bright area to the left reveals highly doped Si. With decreasing free-carrier concentration *n*, the infrared near-field signal decreases and reaches a minimum (dark ring) at a medium

free-carrier concentration. Further decrease of n finally yields a constant near-field signal (right). Such contrast behavior is typical for doping gradients[9]. By fitting the spectra recorded at positions A and B (marked in the infrared image), analogous to Fig. 6.3d, we can quantify the local free-carrier concentration. We find values of $n = 9*10^{19}$ cm^{-3} at position A and $n = 7*10^{19}$ cm^{-3} at position B. The pronounced spectral shift between spectra A and B shows the high sensitivity, allowing for measuring changes of the free-carrier concentration with a relative precision well below 20%.

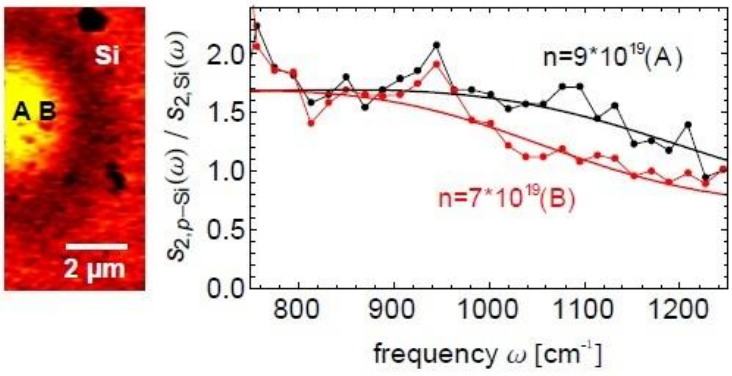

Fig. 6.6 Application of nano-FTIR for determination of the local free-carrier concentration in doping gradients. Left: Infrared near-field image of a doping gradient in the Si substrate of a semiconductor device, taken with a CO2-laser at 10.6 µm wavelength. Right: FTIR near-field spectra taken at positions A and B (data points). The solid lines display calculations according to Fig. 6.3d for two different carrier concentrations n.

6.6 Conclusions

It could be demonstrated, for the first time, that the incoherent broadband radiation of a thermal source can be utilized for imaging and spectroscopy with nanoscale spatial resolution by focusing it to the apex of an s-SNOM tip and analyzing the backscattered light with a combination of higher harmonic demodulation and an asymmetric FT-spectrometer. Plasmonic and phononic material properties could be analyzed with a spatial resolution $< 100\,nm$, which is two orders of magnitude below the diffraction limit. Intriguingly, a thermal source is one of the weakest broadband sources available. Its radiation cannot be well focused due to its spatial extension and it has a quite weak spectral power density leading to rather long measurement times. While practical

applications might be limited with such a weak source our results motivated further projects to conduct this new spectroscopy-technique (introduced as nano-FTIR spectroscopy) with more powerful sources such as synchrotrons[106]. Another approach will be demonstrated in the next chapter, where a novel broadband laser-system has been utilized to perform nano-FTIR spectroscopy[16].

7 Nano-FTIR Absorption Spectroscopy of Molecular Fingerprints

In a second experimental realization, the nano-FTIR system was implemented with a fs-pulsed super-continuum laser as broadband infrared light source. The setup was used to demonstrate that the method can straightforwardly determine the infrared absorption spectrum of organic samples with a spatial resolution of 20 nm, corresponding to a probed volume as small as 10 zeptoliter (10^{-20} l). Corroborated by theory, the nano-FTIR absorption spectra correlate well with conventional FTIR absorption spectra, as experimentally demonstrated with PMMA samples. Nano-FTIR can thus make use of standard infrared databases of molecular vibrations to identify organic materials in ultra-small quantity and at ultrahigh spatial resolution. As an application example the technique was used to identify a nanoscale PDMS (silicone) contamination on a PMMA sample.

7.1 Experimental Setup

The setup that was used for the following experiments in shown in Fig. 7.1a. A standard Au-coated AFM-tip is illuminated by a coherent broadband mid-infrared beam. The beam is generated by a difference frequency generator (DFG, lasnix.com), where two near-infrared, 100-fs pulse trains from a fiber-laser system (FemtoFiber pro IR and SCIR, toptica.com) are superimposed in a GaSe crystal. Compared to an earlier implementation[95], the mid-infrared output power is substantially increased to 0.25 mW. This mid-infrared source emits a continuous spectrum with a usable width up to 700 cm^{-1}, which can be tuned within the limits 700 – 2500 cm^{-1} dependent on DFG settings (e.g. the crystal orientation). Fig. 7.1b shows two mid-infrared output spectra (red and black) for two selected settings that were used in the presented experiments. Clearly, already these two settings suffice for a nearly complete coverage of the central 700 - 2100 cm^{-1} (5-14 μm) molecular infrared fingerprint region. For comparison we show the output spectrum of ref.[95] (blue line), clearly illustrating the significant enhancement of both spectral coverage and spectral intensity achieved with our new DFG setup.

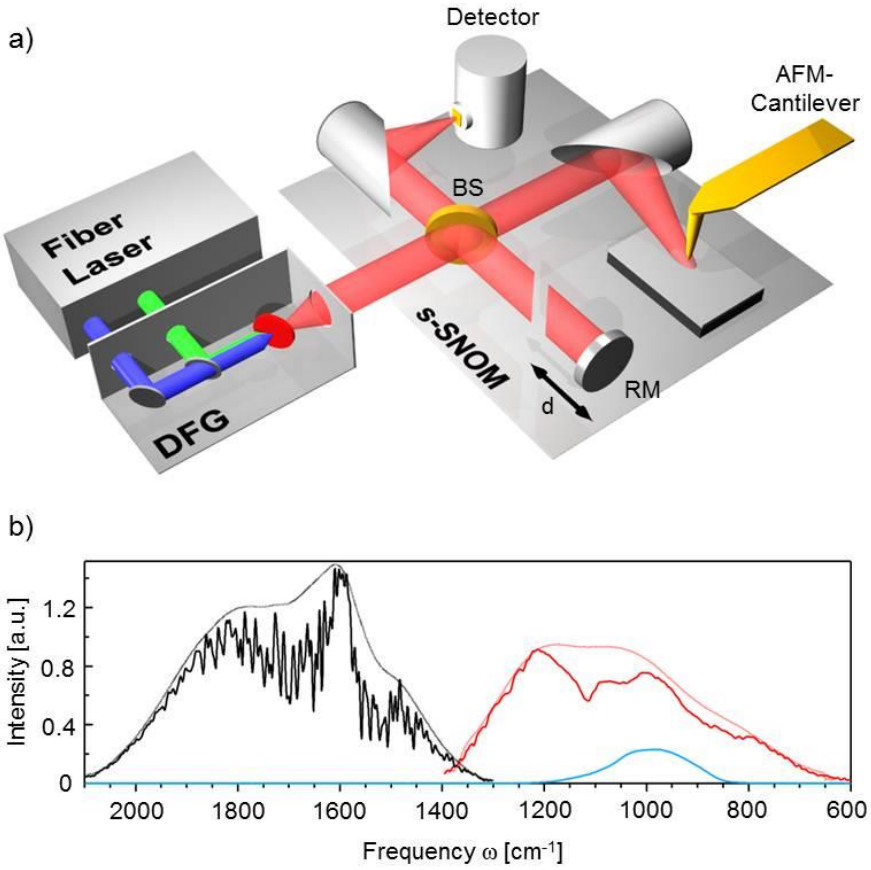

Fig. 7.1 Nano-FTIR operated by a coherent mid-infrared continuum source. (a) Experimental setup, showing the Er-fiber-laser system that emits a pulse train at 1.55 µm (blue) and another one which is broadened and red-shifted (green). A DFG unit superimposes both beams in a nonlinear crystal, which sub sequentially emits a MIR continuum beam that is used for illuminating the AFM tip of the nano-FTIR. The backscattered light is analyzed with an asymmetric Michelson interferometer comprising a beamsplitter (BS) and a reference mirror (RM). (b) Output spectra for two settings of the MIR continuum covering either the lower-frequency fingerprint region 700-1400 cm^{-1} (red) or the higher-frequency fingerprint region 1300-2100 cm^{-1} (black). Measurements were taken approx. 2 m away from the source. The fine curves represent the source spectra corrected for atmospheric absorption. For comparison, the blue line shows the output spectrum of a previous DFG implementation [16].

7.2 Nano-Imaging with a Broadband Laser

First we demonstrate the capabilities of this setup for nanoscale resolved infrared imaging by mapping the boundary region of a 90 nm thin film of PMMA on a Si substrate. Simultaneously, a topographical (Fig. 7.2 upper image) and a near-field infrared image (Fig. 7.2 lower image) is recorded. For the latter we fix the reference arm

of the Michelson interferometer at approximately the "white light position" (WLP). In this case both interferometer arms have equal optical path lengths, thus all frequencies are in phase creating a maximum detector signal. In the optical image we observe a strong material contrast between the PMMA and the Si regions. The stronger infrared signal on Si can be explained by its higher refractive index compared to PMMA[107]. The abrupt signal change at the material boundary verifies the nanoscale spatial resolution. We note that the infrared signal on the PMMA does not depend on the different heights of the PMMA surface in the edge region of the film. This indicates that the probing depth of the near-field interaction[108,109] is smaller than the thickness of the PMMA film.

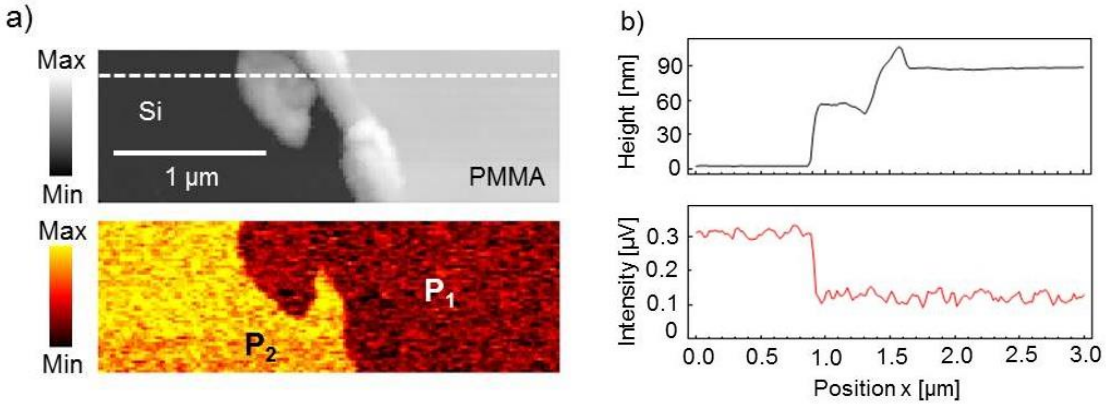

Fig. 7.2 Infrared nano-imaging of a polymer thin film (PMMA) on a Si substrate. (a) Topography (upper) and infrared amplitude image (lower, spectrally averaged over approx. 5-9 µm by setting the interferometer at the WLP) (b) Line profiles of height and infrared signal extracted at the position indicated by the white dashed line (averaged over 8 lines).

7.3 Local Fingerprint Spectroscopy

To demonstrate local fingerprint spectroscopy, we recorded nano-FTIR spectra of PMMA and Si at the positions marked with P_1 and P_2 in Fig. 7.2. Owing to the flat spectral response of Si, the spectrum at P2 serves as reference spectrum (as described in detail in chapter 3.3), yielding the local absorption spectrum of PMMA, $a_2(\omega) \propto P_1/P_2$. The broadband mid-infrared source was first set to cover the frequency range 1300 - 2100 cm^{-1}. For a second set of spectra the source was set to the frequency range 700 - 1400 cm^{-1}. The resulting nano-FTIR absorption spectra $a_2(\omega)$ (as defined in chapter 5.6 and derived in detail in the next paragraphs) are displayed in Fig. 7.3a. For comparison, a FTIR absorption spectrum (Fig. 7.2b) of a PMMA film (thickness of ~5

µm, produced by solvent casting method) was recorded with a conventional FTIR spectrometer (Equinox 55, bruker.com) in transmission mode. The FTIR spectrum shows the well-known molecular absorption lines of PMMA[56,110] around 1730 cm^{-1} (corresponding to C=O stretching), 1265 cm^{-1} and 1240 cm^{-1} (C-C-O stretching), 1190 cm^{-1} (C-O-C bending), and 1145 cm^{-1} (CH_2 bending). Convincingly, all these lines are also clearly seen in the nano-FTIR absorption spectrum. As documented by the dashed grey lines in Fig. 7.3, the near-field absorption peaks appear at the same positions as the far-field absorption peaks. The overall agreement of peak positions, peak shapes and relative peak heights provides clear experimental evidence that the imaginary part of the complex-valued near-field spectrum, $\mathrm{Im}[\sigma_n(\omega)]$, indeed reveals the *local* infrared absorption of the sample. It should be noted that, in contrast to the results shown in the previous chapters, here we compare the imaginary part of the normalized near-field spectrum, and not the amplitude and phase spectra. The explanation and theoretical derivation of this relationship is presented in the next section.

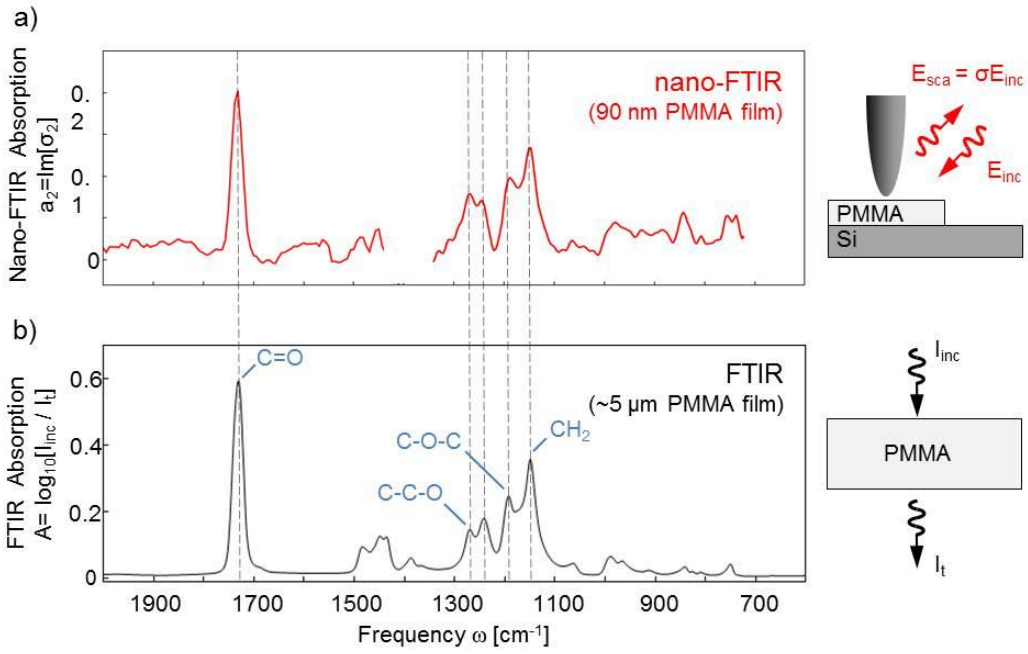

Fig. 7.3 Comparison of conventional far-field FTIR with nano-FTIR (a) Nano-FTIR absorption spectra from a 90 nm thin film of PMMA (b) Far-field FTIR spectra from a ~5 µm thick PMMA film. The nano-FTIR data is obtained from two consecutive measurements where the infrared source spectrum was changed from (2000 cm^{-1} – 1400 cm^{-1}) to (1400 cm^{-1} – 800 cm^{-1}). The acquisition time was 25 min, respectively 16 min, and the spectral resolution is 6 cm^{-1}. The far-field FTIR spectrum was taken in 20 min with a spectral resolution of 4 cm^{-1}. The schematics to the right of the spectra illustrate nano-FTIR and standard transmission FTIR.

7.4 Theory of nano-FTIR of molecular vibrations

The light backscattered from the oscillating metallic tip is analyzed with an asymmetric Fourier transform spectrometer[95,111,112], which is based on a Michelson interferometer. In contrast to conventional FTIR, the sample (together with the tip) is located in one of the interferometer arms (Fig. 7.1). This detection scheme allows for recording both the amplitude $s(\omega)$ and phase $\varphi(\omega)$ spectra of the backscattered light. The pertaining complex-valued scattering coefficient $\sigma(\omega) = s(\omega) \cdot e^{i\varphi(\omega)}$ relates the scattered field $E_{\mathrm{sca}}(\omega)$ with the incident field $E_{\mathrm{inc}}(\omega)$ according to $E_{\mathrm{sca}}(\omega) = \sigma(\omega) \cdot E_{\mathrm{inc}}(\omega)$. To extract the near-field signals, that is, to suppress background contributions, the detector signal is demodulated at a higher harmonic nΩ of the tip vibration frequency Ω (refs.[113,114]). Translation of the reference mirror with a piezo stage yields an interferogram of the demodulated signal. By subsequent Fourier transformation of the interferogram we obtain the complex-valued near-field spectra $E_{\mathrm{n}}(\omega) = \sigma_{\mathrm{n}}(\omega) \cdot R(\omega) \cdot E_{\mathrm{inc}}(\omega)$ where $R(\omega)$ is the spectral response of the instrument including the transmission of the beamsplitter, atmospheric absorption and responsivity of the infrared detector. Analogue to conventional FTIR, the near-field spectra $E_{\mathrm{n}}(\omega)$ are normalized with the help of a reference spectrum $E_{\mathrm{n,Ref}}(\omega)$. The latter can be readily obtained by recording a near-field spectrum of a spectrally flat sample such as Si ($\sigma_{\mathrm{n,Si}}(\omega) = \mathrm{const}$), yielding $E_{\mathrm{n,Ref}}(\omega) = \mathrm{const} \cdot R(\omega) \cdot E_{\mathrm{inc}}(\omega)$. The normalized spectra thus directly yield the scattering coefficient of the tip-sample system, $\sigma_{\mathrm{n}}(\omega) \propto E_{\mathrm{n}}(\omega)/E_{\mathrm{n,Ref}}(\omega)$ (as introduced with example data in chapter 5.4).

The scattering coefficient $\sigma_{\mathrm{n}}(\omega)$ describes the near-field interaction between tip and sample and carries information about the local dielectric function, respectively the refractive index, of the sample. Earlier experiments with organic samples indicate that the imaginary part $\mathrm{Im}[\sigma(\omega)] = s(\omega) \cdot \sin[\varphi(\omega)]$ is connected with the local absorption of the sample[13,19,115]. Owing to the lack of broadband near-field spectra, however, a clear experimental demonstration with molecular fingerprint spectra has not been provided yet, nor has a rigorous physical derivation been put forward. In chapter 5.6, the nano-FTIR absorption was defined as $a_{\mathrm{n}} \equiv \mathrm{Im}[\sigma_{\mathrm{n}}(\omega)]$. Here we verify experimentally and theoretically that nano-FTIR absorption spectra of molecular vibrations correlate well with conventional far-field absorption spectra.

The direct correlation between conventional and nano-FTIR absorption spectra might be surprising when considering that nano-FTIR records the scattered light arising from a complex near-field interaction between tip and sample. We explain this intriguing phenomenon by theoretical considerations of the scattering process. It has been shown formerly that the scattering coefficient σ can be successfully described by the point-dipole model[6] and more accurately by the finite-dipole model[105]. In both models, the scattering coefficient σ has the same structure:

$$\sigma(\omega, H) = \alpha_{\mathrm{eff}}(f \cdot \beta)(1 + r_{\mathrm{s}})^2 \tag{7.1}$$

where $\alpha_{\mathrm{eff}}(f \cdot \beta)$ is the effective polarizability of the tip and r_{s} the far-field reflection coefficient of the sample surface. $\beta = \beta(\omega) = (\varepsilon(\omega) - 1)/(\varepsilon(\omega) + 1)$ is the surface response function, which is dependent on the complex-valued dielectric function $\varepsilon(\omega)$ of the sample. $f = f(H)$ is a (model-specific) frequency-independent function of the tip-sample distance H. For studies of thin films with a thickness $\Delta \ll \lambda$ (for infrared light: $\lambda \sim 10\ \mu m$), r_{s} can be well approximated by the Fresnel reflection coefficient from the substrate. In case the substrate is spectrally flat, like the Si in our experiment, the reflection r_s can be considered as spectrally constant. In the absence of infrared plasmon or geometrical antenna resonances[90,116,117] in the tip, and for a thin film composed of weak molecular oscillators, such as PMMA or other organic materials, the condition $|f \cdot \beta| < 1$ is always satisfied. Therefore we can expand $\sigma(\omega, H)$ into a Taylor series, which to the first order in $(f \cdot \beta)$ yields:

$$\sigma(\omega, H) \approx [\alpha_0 + \alpha_1 \cdot f(H) \cdot \beta(\omega)](1 + r_s)^2 \tag{7.2}$$

where α_0 and α_1 are frequency- and height-independent constants that are determined by the material and the size of the tip. Taking into account the demodulation of the detector signal, which is applied for background suppression in our experiments, and the normalization of the sample spectra to those of Si, all height-independent terms vanish, yielding

$$\sigma_{\mathrm{n}}(\omega) \propto \beta(\omega) \tag{7.3}$$

Thus, the spectral characteristics of $\sigma_{\mathrm{n}}(\omega)$ are determined exclusively by the local dielectric function $\varepsilon(\omega)$ of the sample. This, in principle, allows the determination of both real and imaginary parts of $\varepsilon(\omega)$ from the measurements of the scattering coefficient, and therefore, the derivation of the imaginary part κ of the complex-valued refractive index $N(\omega) = \sqrt{\varepsilon(\omega)}$. For molecular vibrations, such as the ones of PMMA, we find that $\kappa(\omega)$ and $\mathrm{Im}[\beta(\omega)]$ have nearly the same spectral behavior (see Fig. 7.4) and we can write in good first approximation $\kappa(\omega) \sim \mathrm{Im}[\beta(\omega)]$.

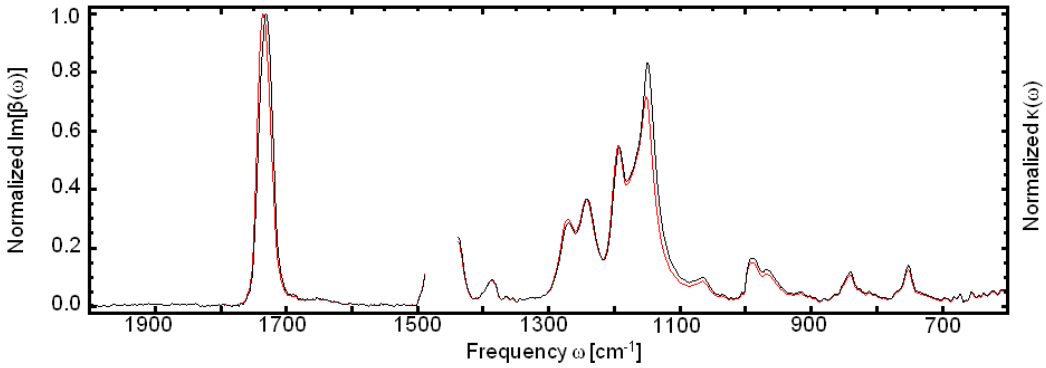

Fig. 7.4 The spectra of κ (black) and $\mathrm{Im}[\beta]$ (red) for a PMMA sample calculated from the real and imaginary parts of $\varepsilon(\omega)$ obtained by ellipsometry. Both spectra are normalized to the peak values at $\omega \approx 1730\mathrm{cm}^{-1}$.

Considering that the far-field absorption A in conventional FTIR spectroscopy follows the relation $A \propto \kappa(\omega)$, we immediately obtain $a_{\mathrm{n}}(\omega) \propto \mathrm{Im}[\beta(\omega)] \propto \kappa(\omega) \propto A$. The connection between near-field and far-field absorption is thus described in good approximation by the simple and model-independent relation

$$a_{\mathrm{n}}(\omega) \propto A \tag{7.4}$$

which theoretically explains the experimental observation documented in Fig. 7.3, and provides a firm ground for chemical recognition and possibly even chemometrics at nanoscale spatial resolution.

7.5 Spatial Resolution of Nano-FTIR

In Fig. 7.5 we demonstrate nanoscale spectroscopic mapping of the local infrared absorption. While scanning the tip across the PMMA edge (Fig. 7.5a), an infrared spectrum is recorded at each position. Each panel of Fig. 7.5b shows 50 spectra, every single one recorded in 80 s and with 13 cm^{-1} spectral resolution. The distance between the points at which the spectra are acquired is 20 nm. As before all spectra are normalized to the reference spectrum taken on the Si surface. On the PMMA we clearly see the characteristic absorption lines. The peak maxima are nearly constant until the edge is reached at $x = 0.5$ µm.

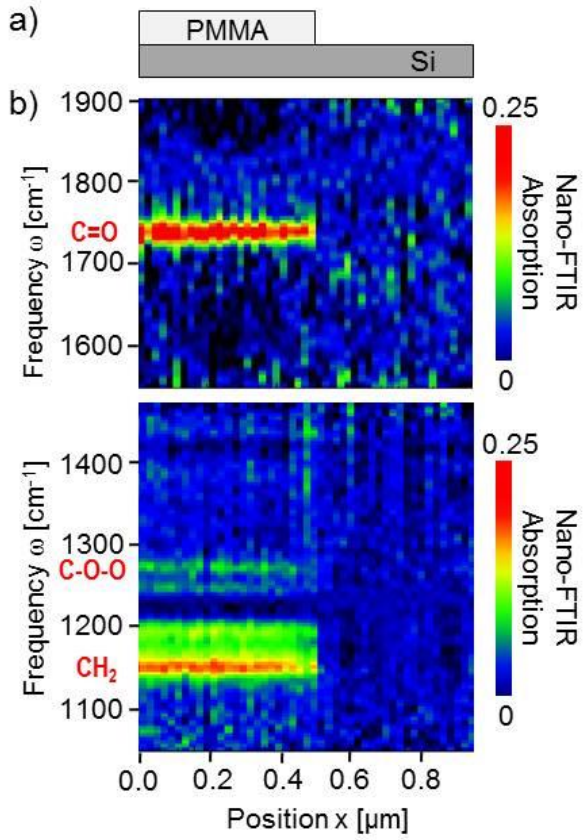

Fig. 7.5 Nanoscale infrared-spectroscopic mapping of PMMA on Si. (a) Schematics of the sample cross section. (b) Infrared-spectroscopic line scans recorded while the tip was scanned in 20 nm steps (horizontal axis) across the sample. Each panel is composed of 50 spectra (vertical axis) acquired with the coherent source set to cover the 1000 - 1500 cm^{-1} (bottom) and 1500 - 1900 cm^{-1} (top) spectral ranges.

Within a single scan step, the strong C=O and CH_2 absorption peaks vanish completely. This observation confirms that infrared fingerprint spectroscopy can be performed at 20

nm spatial resolution. Because the probing depth of the near-field interaction approximately equals the lateral spatial resolution[108,109,118], we further conclude that the probed volume is as small as $(20\ \text{nm})^3 = 10^{-20}\ \text{l} = 10\ \text{zl}$ (10 zeptoliter). We note that the spatial resolution in s-SNOM is determined essentially by the radius of the tip apex[6], which is about 20 nm in our experiments. Decreasing the scan step below 20 nm thus would not improve the spatial resolution.

7.6 Identification of Nanoscale Sample Contaminants

As an application example we demonstrate the chemical identification of nanoscale sample contaminants. Fig. 7.6a shows the topography image of a scratched PMMA film (Position P_3) on a Si substrate, revealing a particle-like feature at the PMMA edge (Position P_4),

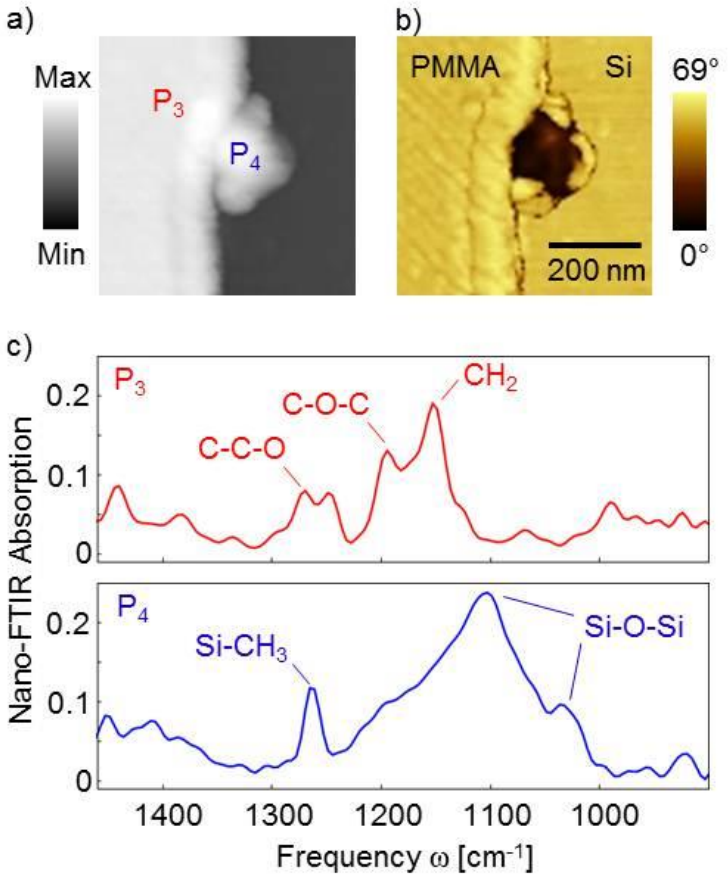

Fig. 7.6 Chemical identification of nanoscale sample contaminations with nano-FTIR. (a) AFM topography image of a scratched PMMA film on a Si substrate. (b) Mechanical AFM phase image, where the strong contrast designates a particle that consists neither of PMMA nor of Si. (c) nano-FTIR absorption spectra of the PMMA film (taken at position P_3) and of the particle (taken at position P_4). The acquisition time was 7 min and the spectral resolution is 13 cm^{-1}.

which in the mechanical AFM phase image (Fig. 7.6b) exhibits a strong phase contrast of about 70 degree. Such phase contrasts indicate different materials[119]. Without prior knowledge, however, we cannot identify the particle-like feature of about 100 nm diameter. By taking a nano-FTIR absorption spectrum (lower panel in Fig. 7.6c) in the center of the particle (marked with P_4), we find a significantly different spectral signature compared to the spectrum taken on the PMMA film at the position marked with P_3. While the latter exhibits the known PMMA vibrational fingerprint (as seen before in Fig. 7.3 and Fig. 7.5), we find at P_4 a strong and broad peak centered around 1100 cm^{-1}, a sharper peak around 1260 cm^{-1}, and a small peak around 1040 cm^{-1}. With the help of conventional FTIR spectra from literature, we can assign the peak around 1260 cm^{-1} to the Si-CH_3 symmetric deformation and the broad peak around 1100 cm^{-1} as well as the peak around 1040 cm^{-1} to Si-O-Si asymmetric stretching modes[120]. The appearance of these spectral lines is typical for Polydimethylsiloxane (PDMS)[120]. We can thus identify the particle-like feature as a PDMS contamination. We note that the PMMA sample preparation and pre-characterization involved PDMS material, obviously leaving PDMS remainders on the sample surface.

7.7 Conclusions

In conclusion, nano-FTIR with a coherent mid-infrared continuum source enables a full spectroscopic analysis of molecular vibrations on the nanometer scale in the important mid-IR frequency range 800-2000 cm^{-1}. We have shown experimentally and theoretically that nano-FTIR absorption spectra correlate well with conventional (far-field) FTIR absorption spectra. Nano-FTIR thus opens the door to nanoscale chemical identification of virtually any substance exhibiting IR vibrational resonances, in ultrasmall quantities and at ultrahigh spatial resolution, by simply searching for the corresponding spectra in standard FTIR databases. We envision, for example, nanoscale chemical mapping of polymer blends, organic fibers, and biomedical tissue. We furthermore established a simple relation between nano-FTIR spectra and the dielectric response of the sample, which in the future will allow for straightforward reconstruction of both the real and imaginary part of the local refractive index, respectively the local dielectric function $\epsilon(\omega)$ of organic, molecular, and biological materials, nanocomposites, or nanodevices.

8 Resonant Antenna Probes for Near-Field Microscopy

In typical IR s-SNOM studies, standard metalized AFM tips are used. The infrared antenna performance of these tips[32], however, is widely unexplored and antenna concepts[33-47] have not yet been applied to optimize near-field probes for the infrared spectral range. In this chapter we demonstrate the successful fabrication of infrared-resonant antenna tips on standard Si cantilevers with focused ion beam (FIB) machining. Characterization of these tips by electron energy loss spectroscopy (EELS), Fourier transform infrared (FTIR) spectroscopy and Fourier transform infrared near-field spectroscopy (nano-FTIR) clearly reveals geometrical antenna resonances in the tips, which are found to be in good agreement with numerical calculations. We verify the excellent probe performance of these tips by infrared near-field imaging of tobacco mosaic viruses of only 18 nm diameter.

8.1 Concept

The design of the anticipated near-field probes is illustrated in Fig. 8.1a. A high aspect ratio gold cone with a sharp tip apex replaces the tip of a standard Si AFM cantilever. We first study numerically the antenna function of such tips (using a commercial FDTD software package, Lumerical). To that end we consider a tip geometry as illustrated in Fig. 8.1b, where we assume a plane wave illumination (E_{inc}) with p-polarization at an angle α with respect to the tip axis. Fig. 8.1c shows the calculated near-field magnitudes near the tip apex (marked with the cross in Fig. 8.1b) for α = 0°, normalized to the incident field for antenna tips of three different lengths L. For the 0.5 µm long antenna (shown in red) we find a pronounced resonance peak at a frequency $\omega_{\mathrm{res},1} = 5120$ cm^{-1} ($\lambda \approx 1.95$ µm), corresponding the fundamental dipolar mode ($l = 1$) and a second, weaker peak at $\omega_{\mathrm{res},3} = 13420\ \mathrm{cm}^{-1}$ ($\lambda \approx 0.75$ µm), corresponding the second order dipolar mode ($l = 3$)[121]. With increasing rod length L, the resonance positions shift to lower frequencies ω, from the near-IR to the mid-infrared to the THz spectral range. Compared to classical radio wave antennas[122], where the resonance length is about half

the excitation wavelength λ, $L_{\mathrm{res}} = \lambda/2$, the tip resonances occur at much shorter lengths. We find $L_{\mathrm{res}} = \lambda/3.9$, $\lambda/2.7$ and $\lambda/2.4$ for the near-IR, mid-IR and THz spectral range, respectively, which we assign to the tip geometry, the finite frequency-dependent conductivity of the metal and the Si base. The latter acts as a capacitive load, which typically redshifts the antenna resonance[123,124].

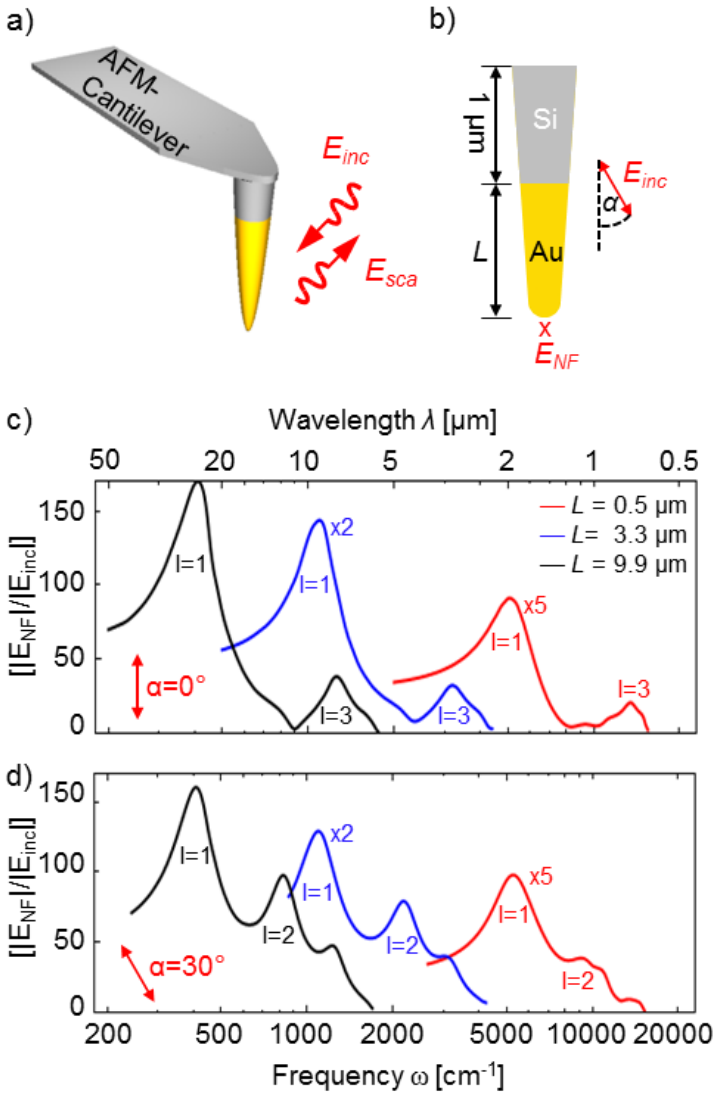

Fig. 8.1 Resonant antenna probes for near-field microscopy. a) Sketch of a Au-rod placed on a Si-based cantilever. b) Model to simulate the near-field enhancement at the tip apex for rods of different lengths L placed on a Si base of 1 µm length. c) Calculated near-field (E_{NF}) at 10 nm below the tip apex (marked with „x“ in panel b), normalized to the incident field (E_{inc}), which is linear polarized at an angle α = 0° with respect to the tip axis. For better visibility, the spectra of the 3.3 µm (blue) and 0.5 µm (red) long antenna-tip have been scaled by a factor of 2 and 5, respectively. d) Same as c) but for a polarization tilted by α = 30° with respect to the tip axis.

An interesting aspect is the significant increase of the field enhancement at the tip apex, amounting to more than 100, when the tip length increases, i.e. when the resonance shifts to the THz spectral range. We assign this finding to the increased sharpness of the tip relative to the wavelength and the rod-length, respectively. In Fig. 8.1d we show calculated near-field spectra where the tips are illuminated with p-polarized light under an angle of α = 30° relative to the tip axis, as typically done in s-SNOM. Additional to the dipolar modes ($l = 1,3$), the plane wave efficiently couples to the odd modes ($l = 2,4$)[125], due to retardation along the tip axis.

Under normal incident the odd modes are “dark”, owing to the vanishing total dipole moments because of a centrosymmetric charge distribution. The proposed antenna-tips promise precise tuning and optimization of the local field enhancement at the tip-apex throughout a broad spectral region from visible to THz frequencies. Tilted illumination thereby excites both even and odd modes, which increases the usable spectral bandwidth of the tips, although the maximum field enhancement decreases slightly.

8.2 Fabrication with Focused Ion Beam (FIB)

Fig. 8.2 shows the fabrication procedure of the proposed antenna tips by focused ion beam (FIB) machining. The fabrication was done with a Helios600 DualBeam (FEI, Netherlands) electron microscope by Andrey Chuvilin. We use standard Si atomic force microscopy (AFM) cantilevers (Nanosensors, Switzerland), where we first cut the tip apex.

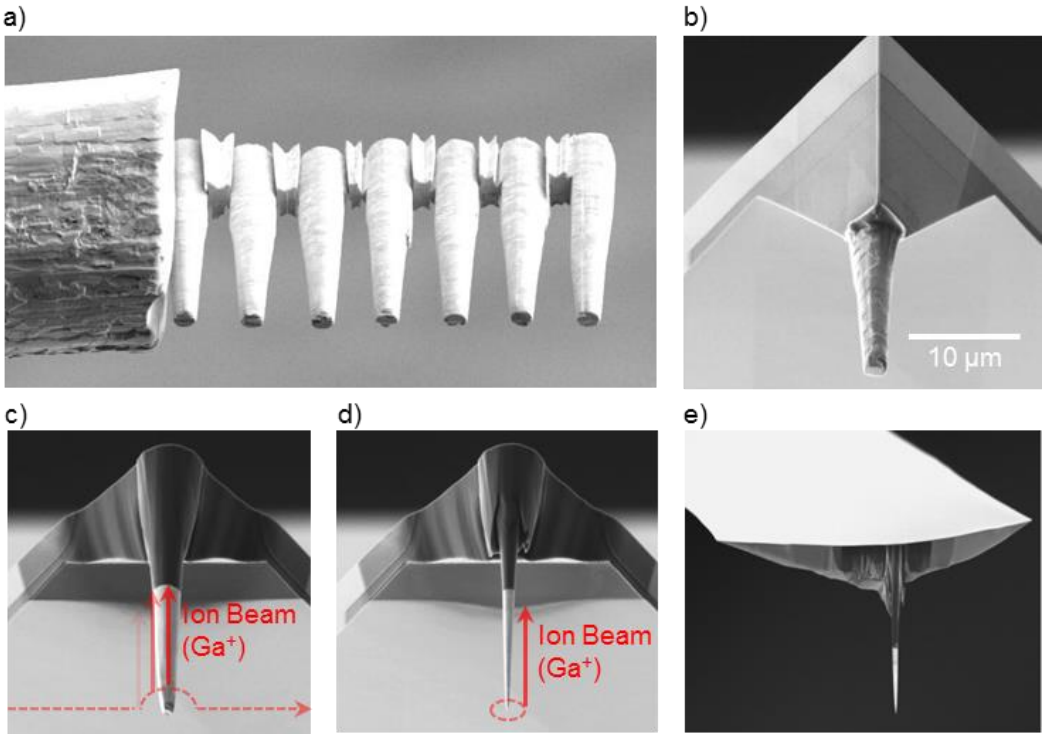

Fig. 8.2 Fabrication of antenna-tips by focused-ion-beam (FIB). a) Several rods cut from a 25 µm thick Au wire. b) Single Au rod attached to the cantilever. c) Intermediate step of sharpening the tip with FIB. The ion beam (red arrow) is moved along the red dashed line. d) Tip sharpening by circular ion milling (as indicated by the red dashed circle). e) Final antenna-tip.

Then a several micrometer long rod is milled out of a 25 µm thick Au wire (Fig. 8.2a) and attached to the cut tip by focused ion beam induced deposition (FIBID) of SiO_x Fig. 8.2b). As illustrated in Fig. 8.2c and d, the Au rod is shaped by the ion beam until a sharp high aspect ratio cone is formed (Fig. 8.2e). By adjusting the milling parameters, such as the ion beam current and the ion beam focusing, the conical angle of the tip can be varied. Simultaneous monitoring of the ion milling process with the electron beam allows for controlling the desired length of the Au cone with a precision of ±10 nm. The length can be varied between 200 nm and several tens of micrometers, yielding resonant

antennas for the visible, IR and THz spectral range. Remarkably, the radius of curvature of the tip apex can be as small as 10 nm (see Fig. 8.3).

8.3 Electron Energy Loss Spectroscopy (EELS)

We first study the antenna tips by electron energy loss spectroscopy (EELS). This method allows for both local plasmon spectroscopy and spatial plasmon mapping, the latter directly revealing the plasmonic eigenmodes of the antennas[126-129].

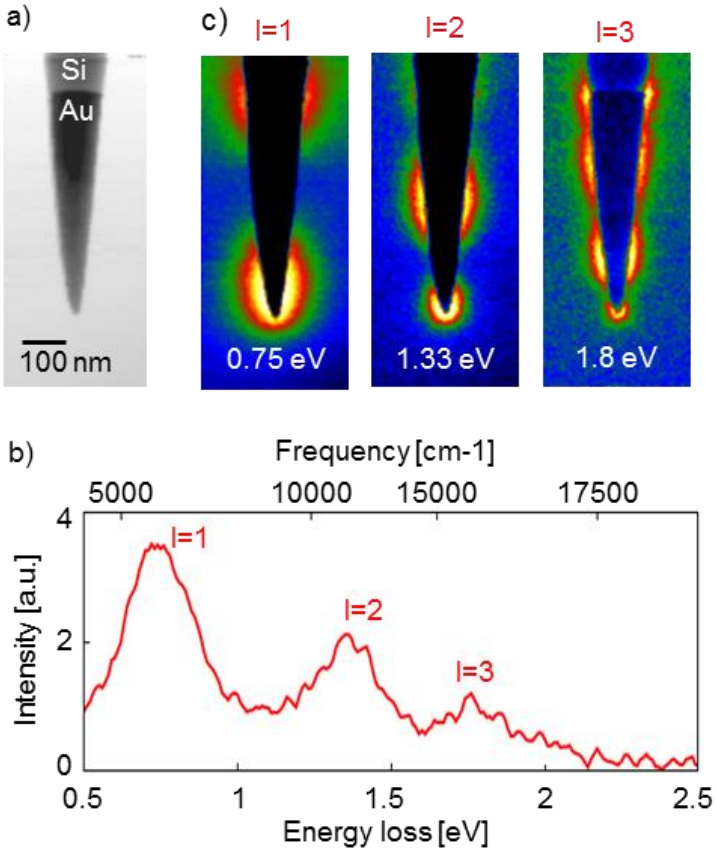

Fig. 8.3 Electron Energy Loss Spectroscopy (EELS) of FIB-fabricated antenna-tips. a) STEM image of a 0.5 µm long antenna-tip. b) EELS spectrum recorded at tip apex. c) EELS maps at the peak positions in the energy loss spectrum.

We use a Titan 60-300 (FEI, Netherlands) electron microscope equipped with a gun monochromator and an EELS spectrometer (GIF Quantum, Gatan, USA). For an accelerating voltage of 80 kV, the energy filter can reach an energy resolution of approximately 100 meV. This gives access to electron energy losses starting from 400

meV (corresponding to $\omega = 3200\,\mathrm{cm}^{-1}$), which allows for the study of plasmon resonances in the visible and near-IR spectral range. We use EELS spectrum imaging (SI) in scanning transmission electron microscope (STEM) mode to acquire spatially resolved EELS spectra. This method acquires a full resolution EELS spectrum at each pixel of the image. The recorded data cube is further processed to obtain either cumulative EELS spectra over a defined area or a spatial intensity distribution of particular energy losses (e.g. plasmon maps). In Fig. 8.3 we show the results obtained for a 0.5 micrometer long antenna tip. The STEM image (Fig. 8.3a) shows the tip with an apex radius of about 10 nm. Recording an EELS spectrum (Fig. 8.3b) at the tip apex reveals maxima at 0.75 eV, 1.33 eV and 1.8 eV. By mapping the energy loss at these energies (Fig. 8.3c), we can unambiguously assign the antenna modes[121,126-129]. The two bright spots in the 0.75 eV map clearly reveal the $l = 1$ (fundamental dipolar) plasmon mode. At 1.33 eV we observe three maxima, visualizing the $l = 2$ ("dark") mode of the tips. The $l = 3$ (second order dipolar) mode can be identified by the four maxima seen in the map at 1.8 eV. The EELS spectrum is in good agreement with the numerically calculated optical spectrum of the 0.5 µm long antenna tip shown in Fig. 8.1, experimentally verifying the function of the tips as resonant optical antennas.

8.4 AFM and SNOM Performance

The tip fabrication process offers great tunability of the antenna resonance, by simply adjusting the tip length. With lengths in the micrometer range we obtain resonances in the mid-infrared spectral range (4 - 20 µm wavelength), which is difficult to access by EELS. We thus test the mid-infrared performance of these tips by directly employing them as near-field probes in our near-field microscopy and spectroscopy setup shown in Fig. 8.4a. It is based on a commercial s-SNOM (Neaspec, Germany), where cantilevered AFM tips are used as near-field probes. Operating the AFM in tapping mode, the tip is vertically vibrating with an amplitude of about 50 nm at the mechanical resonance frequency Ω of the cantilever, in this work at about $\Omega \sim 120$ kHz. We perform mid-IR near-field imaging by illuminating the FIB-fabricated antenna-tips with a quantum cascade laser (QCL, Daylight Solutions, USA), tunable between 1550 cm^{-1} and 1750 cm^{-1} (Fig. 8.4a). A Michelson interferometer is used to analyze the tip-scattered light. Unavoidable background signals can be efficiently suppressed by

demodulating the detector signal at a higher harmonic of the tapping frequency, nΩ (refs.[6,7]). Employing a pseudo-heterodyne detection scheme[91] (where the reference mirror RM oscillates at a frequency M, see chapter 4.3.3.2) enables the simultaneous detection of both near-field amplitude $s_{\mathrm{nf,n}}$ and phase $\varphi_{\mathrm{nf,n}}$-signals.

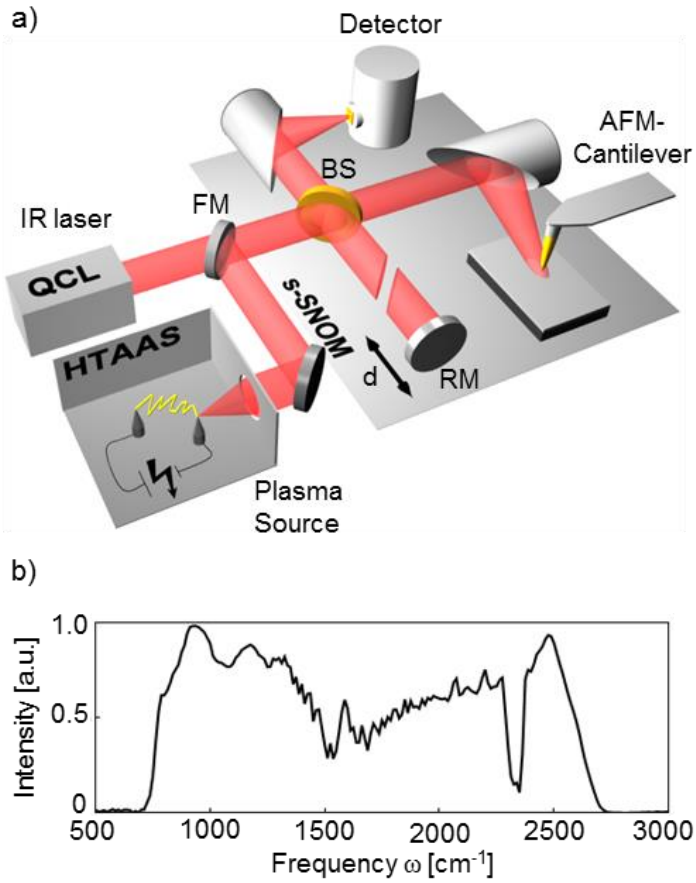

Fig. 8.4 Near-field imaging and spectroscopy setup. a) Schematics showing an s-SNOM employing a tunable single line laser (quantum cascade laser, QCL) or a broadband plasma source (high temperature argon arc source, HTAAS) for tip illumination. The illumination source can be changed with a flip mirror (FM). The light backscattered from the tip is analyzed with a Fourier-Transform spectrometer, comprising a beamsplitter (BS, uncoated ZnSe), a reference mirror (RM) and a detector. b) Output spectrum of the plasma source. The available frequencies are limited by the cut-off of the detector at the lower frequency side, and a low-pass filter (Anti-Reflection coated Ge window, not shown) at the high-frequency side. The dips in the spectrum are due to atmospheric absorption of air (e.g. water vapor, CO2), which the IR beam has to pass.

We first validate the mid-infrared antenna function of the tips, i.e. the conversion of the incident light into a highly concentrated infrared spot at the tip apex. To that end we recorded the near-field amplitude signals s_{n} (for the harmonics n = 1, 2, 3 and 4) as a

function of the distance *z* between the tip and a gold surface (so called approach curve). Fig. 8.5b shows the approach curves we obtained with a 4.8 µm long tip (shown in Fig. 8.5a) that was illuminated with light of 6 µm wavelength ($\omega = 1660\ \mathrm{cm}^{-1}$). We find that already for $n > 1$ the amplitude signals rapidly decay to the noise level when z increases, revealing strong near-field confinement at the tip apex and that the amplitude signals are essentially background free. We note that the illumination wavelength has been chosen in order to match an expected resonance of the 4.8 µm long antenna-tip, which is verified below in Fig. 8.6a.

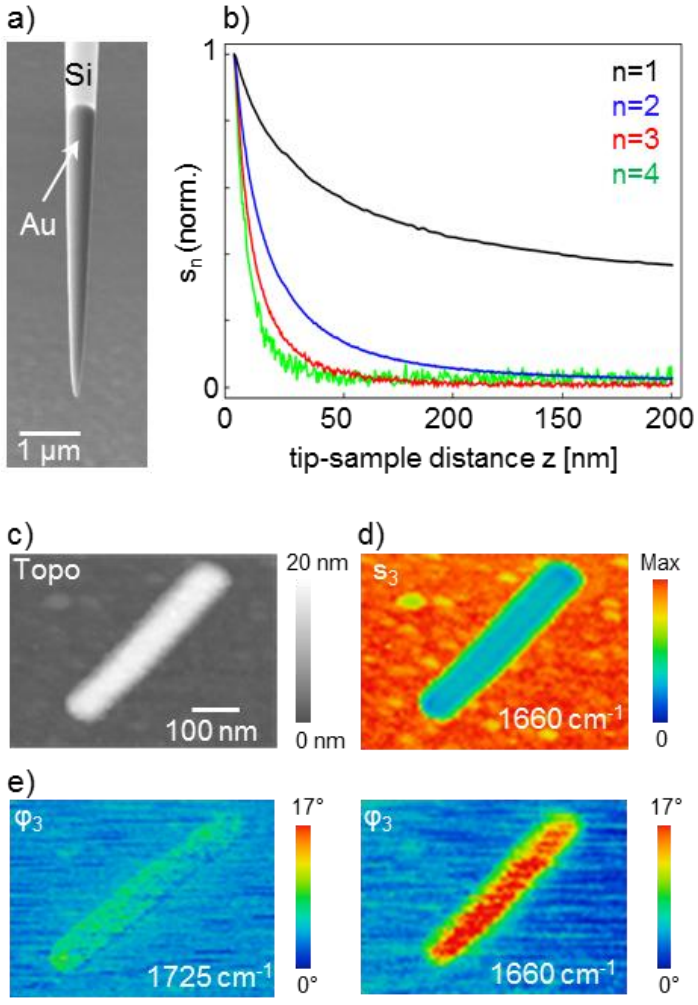

Fig. 8.5 AFM and s-SNOM performance of antenna tips. a) SEM image of a 4.8 µm long antenna tip. b) Approach curves on a flat Au-surface showing the IR amplitude signal s_n as a function of tip-sample distance. The amplitude of the tip vibration was set to 20 nm. c) AFM-topography image of a single tobacco mosaic virus. d) Simultaneously acquired near-field amplitude image s_3 (tip-illumination set to 1660 cm^{-1}). e) Near-field phase images φ_3 for tip-illumination set to 1660 cm^{-1} (right) and 1725 cm^{-1} (left).

The performance of the antenna tips for topography and near-field imaging is demonstrated in Fig. 8.5c-e. As a test object we have chosen a tobacco mosaic virus (TMV) because of its well-defined geometry and infrared response. TMVs have a diameter of 18 nm and consist of pure protein, exhibiting a well-known molecular vibrational resonance at 1660 cm^{-1} (amide I band). In the topography image (Fig. 8.5c), the virus can be easily identified as a 450 nm long rod with a height of about 18 nm. In the amplitude image s_3 (Fig. 8.5d) a decrease of the signal can be seen on the virus, which can be assigned to the lower refractive index of the organic virus compared to the Si substrate. The phase image φ_3 recorded at 1660 cm^{-1} (Fig. 8.5e, right) shows a distinct contrast between the virus and the Si substrate, amounting to approximately 17°. This phase contrast can be explained by the molecular absorption of the sample at this illumination frequency[16,18]. As expected, the phase contrast vanishes when the illumination is tuned to 1725 cm^{-1}, where the protein does not absorb Fig. 8.5e, left)[18]. The images exhibit an improved signal-to-noise ratio, compared to results we previously obtained with standard metallized AFM tips (ref.[18]), demonstrating the excellent performance of our antenna tips.

8.5 Nano-FTIR of RA Probes

To study the spectral near-field characteristics of the tips, we employ the Michelson interferometer shown in Fig. 8.4a as Fourier transform infrared (FTIR) spectrometer, thus operating the s-SNOM in nano-FTIR mode. For tip illumination we use the radiation from a current-induced high-temperature argon arc source (HTAAS, in the following referred to as plasma source)[130]. Its output spectrum corresponds to that of a blackbody emitter of 10000 K temperature, providing a spectral energy density comparable to synchrotron radiation[131]. Fig. 8.4b shows the output spectrum, which spans the whole mid-infrared region from 700 cm^{-1} up to 2700 cm^{-1}. In order to obtain the infrared response of the antenna tips, we perform spectroscopy of the scattered light when the tip is in near-field interaction with a gold surface, which exhibits a flat spectral response in the mid-infrared spectral range.

Fig. 8.6 shows representative infrared near-field (nano-FTIR) spectra of antenna tips with different lengths, varying between $L = 3.3$ µm and 5.2 µm. In the spectrum of the 3.7 µm antenna tip we find two peaks, one around $\omega_{\mathrm{res},1} = 950\ \mathrm{cm}^{-1}$ (corresponding to a wavelength of $\lambda \approx 10.5$ µm) and one around $\omega_{\mathrm{res},2} = 2100\ \mathrm{cm}^{-1}$ ($\lambda \approx 4.8$ µm).

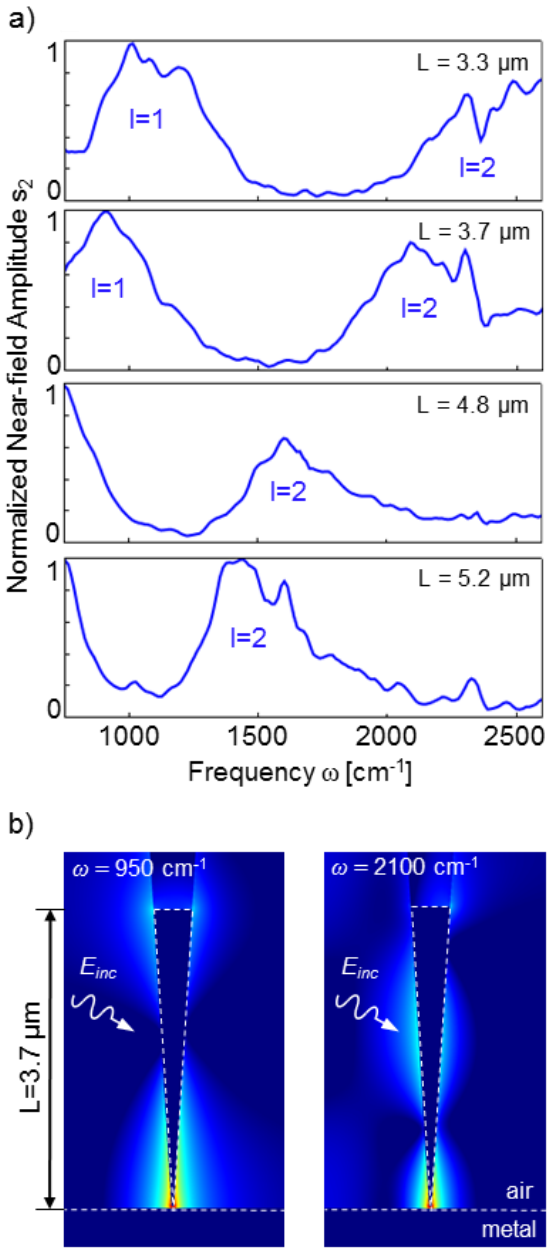

Fig. 8.6 Infrared near-field response of antenna tips. a) nano-FTIR spectra of antenna tips with different lengths L in contact with a flat Au surface. The spectra are normalized to the input spectrum of the plasma source and the maximum value of each spectrum is set to 1. The small dips or peaks around 2350 cm^{-1} we assign to changing atmospheric CO_2 absorption between the measurement of the tip spectrum and the input spectrum. b) Calculated field distribution (logarithmic color scale) around a 3.7 µm antenna tip placed 20 nm above a metal surface, assuming p-polarized plane wave illumination under an angle of 60° relative to the tip axis. Illumination as indicated by the white arrow (at the given frequencies).

Comparing the peak positions with the calculations in Fig. 8.1d (blue curve), we can assign the peak around 950 cm^{-1} to the fundamental dipolar mode ($l = 1$) and the second peak to the second order resonance ($l = 2$). With increasing antenna length (to $L =$ 4.8 µm and 5.2 µm), the resonance peaks of the first and second order modes ($l = 1$ and $l = 2$) shift to lower frequencies. This clearly demonstrates the possibility to tune the resonances by simple adjustment of the tip length. Interestingly, we observe the $l = 2$ mode, as predicted in Fig. 8.1d. To corroborate this mode assignment we calculate the field distribution around a $L = 3.7$ µm long antenna tip situated above a metal surface. It is illuminated with p-polarized light at an angel of 30° relative to the surface. Fig. 8.6b shows the field distributions for illumination at $\omega_{res,1}$ = 950 cm^{-1} and $\omega_{res,2}$ = 2100 cm^{-1}, the two frequencies where we observe the experimental resonance peaks in Fig. 8.6a ($L = 3.7$ µm). The two spatial field maxima observed at 950 cm^{-1} show the fundamental dipole mode ($l = 1$), while the 3 maxima at 2100 cm^{-1} clearly reveal the $l = 2$ mode. For both modes we find the strongest field concentration at the tip apex, which is the key to nanoscale resolved infrared mapping, as demonstrated in Fig. 8.5.

8.6 FTIR of RA Probes

We finally verify the infrared resonances of the tips by recording relative transmission spectra with a standard FTIR micro-spectrometer (Bruker, Hyperion 2000 microscope coupled to a Vertex 70 FTIR spectrometer). The tips are illuminated with light polarized either parallel or perpendicular to the tip axis. A small aperture (15 µm x 15 µm) is employed to isolate the infrared response of the tip.

Fig. 8.7 shows two representative spectra, obtained with antenna tips of $L = 4.5$ µm and 4.8 µm length and for polarization parallel to the tip axis. Both show a clear dip in the relative transmission, appearing at around $\omega_{res,1} = 850\ cm^{-1}$ and $920\ cm^{-1}$, respectively. Comparing with the calculations of Fig. 8.1d, we assign these dips to the fundamental dipolar antenna mode ($l = 1$). In a control experiment we recorded spectra of the transmitted light when illuminating the tip with light polarized perpendicular to the tip axis (not shown). The dips in the transmission vanish,

corroborating that the dips in Fig. 8.7 can be assigned to resonant infrared excitations along the tip axis.

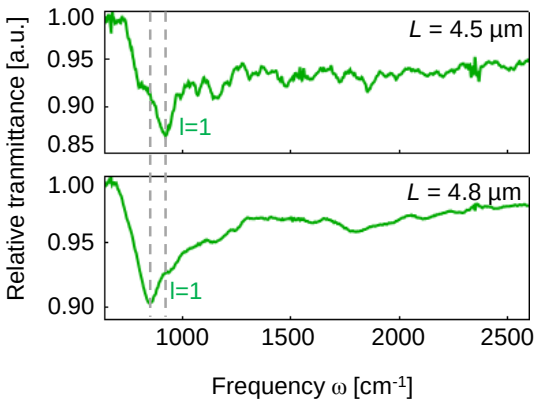

Fig. 8.7 Relative IR transmittance spectra of antenna tips with a length L = 4.5 µm and L = 4.8 µm. Measurement was done by Roman Krutokhvostok.

To summarize our results, we plot in Fig. 8.8 the resonance wavelengths $\lambda_{\mathrm{res,l}} \propto 1/\omega_{\mathrm{res,l}}$ obtained by EELS (red symbols), nano-FTIR (blue symbols) and FTIR (green symbols) as a function of the tip length L.

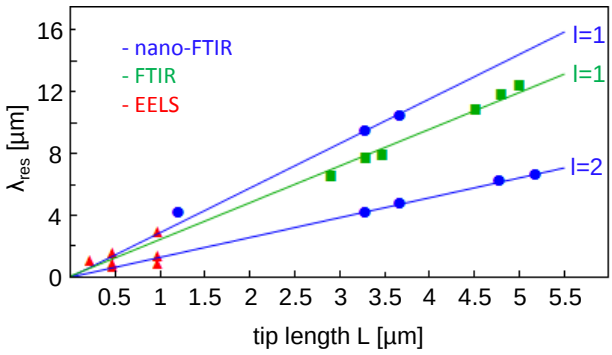

Fig. 8.8 Resonance wavelength λ_{res} as a function of the tip length L, measured by EELS (red symbols, data extracted from Fig. 8.3b), nano-FTIR (blue symbols, data extracted from Fig. 8.6a) and FTIR (green symbols, data extracted from Fig. 8.7). The lines represent linear fits to the corresponding data points.

We find a linear behavior for the nano-FTIR and FTIR results, as expected from antenna theory[122]. However, the simple relation $\lambda_{\mathrm{res,l}} = 2L/l$ of antenna theory does not fit our data. This is because antenna theory assumes ideal metals and very large aspect ratios (the antenna length compared to antenna width is typically $>10^3$)[122], while at optical and infrared frequencies we have to consider the finite conductivity of metals, plasmons, as well as aspect ratios that are much smaller than 10^3. On the other hand, Novotny[132] showed that antenna designs can be transferred to the optical frequency regime by replacing λ by a linearly scaled effective wavelength $\lambda_{\mathrm{eff}} = n_1 + n_2\,\lambda/\lambda_{\mathrm{p}}$, with λ_{p} being the plasma wavelength and n_1, n_2 being coefficients that depend on geometry and material properties. In this case, the resonance wavelength of the mode *l* can be found according to

$$\lambda_{\mathrm{res,l}} = \frac{2L/l - n_1}{n_2}\lambda_{\mathrm{p}}. \qquad (8.1)$$

At infrared frequencies and for micrometer long gold antennas with high aspect ratio (> 10), n_1 becomes very small and eq. (8.1) becomes $\lambda_{\mathrm{res,l}} = \frac{2\lambda_{\mathrm{p}}}{n_2 l}L = b_{\mathrm{l}}L$, which for $b_{\mathrm{l}} = \frac{2\lambda_p}{n_2 l} = \frac{2}{l}$ yields the relation for an ideal antenna. Fitting the data of Fig. 8.8 with eq. (8.1), we find b_1= 2.9 for the nano-FTIR (blue) and b_1= 2.4 for the FTIR experiments (green). Obviously, the nano-FTIR resonances are redshifted compared to FTIR. We assign this to the near-field interaction between the antenna-tip and the gold sample, which is absent in the case of the FTIR measurements. For the second order resonance ($l = 2$) we obtain $b_2 = 1.3 \approx \frac{b_1}{2}$, which confirms our mode assignment. Altogether Fig. 8.8 clearly corroborates that the optical response of the tips is governed by geometrical antenna resonances, which can be understood and described within the framework of optical antenna theory.

8.7 Comparison with Standard Tips

We finally compare a resonant tip of 1.92 μm length (Fig. 8.9a) with a standard commercial Au tip (Fig. 8.9b). To that end we imaged one and the same TMV virus and recorded approach curves on a Si substrate with both tips employing the same imaging

parameters. The length of the FIB fabricated tip was chosen in order to exhibit the fundamental resonance at 1660 cm^{-1} (see Fig. 8.8). We applied an illumination power of only 0.3 and 0.15 mW for imaging and approach curves, respectively, in order to better see the signal-to-noise ratio in the images and approach curves and to demonstrate the performance of the tips using the typically weak power of broadband infrared sources[16,29,95,133,134]. After maximizing the near-field signals for each tip, we obtain about two times more amplitude signal with the 1.92 µm long tip, in reasonable agreement with the calculations shown in Fig. 8.1e. We note that the absolute near-field signals depend on the alignment of the laser focus and the interferometer, which lets us consider this comparison as an estimate rather than an exact quantitative evaluation. We find that the phase contrast φ_3 of the virus obtained with the resonant tip (Fig. 8.9a, upper row) is about two-fold enhanced compared to the image obtained with the standard tip (Fig. 8.9b, upper row), while the noise is reduced.

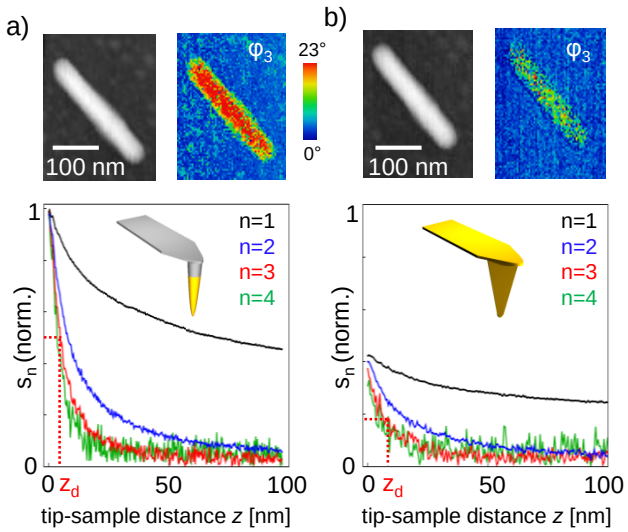

Fig. 8.9 Comparison of the performance of resonant and standard tips under the same conditions. (a) Results obtained with a 1.92 µm long tip, resonant at 1660 cm^{-1}. (Top) Topography (left) and phase image φ_3 (right) of a TMV virus. (Bottom) Approach curves on a flat Si substrate. (b) Results obtained with a standard tip (Nanosensors, PPP-NCST-Au). (Top) Topography (left) and phase image φ_3 (right) of the same TMV virus as in (a). (Bottom) Approach curves on a flat Si substrate. The approach curves of the 1.92 µm long tip have been normalized to the signal at z = 0 nm. The approach curves of the standard tip have been normalized to the signal at z = 0 nm obtained with the resonant tip at the corresponding harmonic n. For imaging, both tips were illuminated with 0.3 mW optical power at 1660 cm^{-1} and both tips were oscillating with 20 nm tapping amplitude. For approach curves, both tips were illuminated with 0.15 mW optical power at 1660 cm^{-1} and both tips were oscillating with 50 nm tapping amplitude.

Recording approach curves (amplitude s_n vs. tip−sample distance z), we also find that the near-field confinement at the tip apex is better for the antenna tip. The amplitude signal s_3 decays to half its value at a tip−sample distance of z_d = 4.6 nm (Fig. 8.9a), while for the standard tip we measure z_d = 8.6 nm. The improved confinement at the apex of the antenna tip we assign to the apex geometry and an eventually smaller tip radius. This might also explain the enhanced phase contrast of the virus, however, further studies are needed to separate the different contributions of apex geometry and tip resonance on the image contrasts.

8.8 Conclusions

We have demonstrated FIB-assisted fabrication of micrometer-long antenna tips on conventional AFM cantilevers. As verified by EELS, FTIR and nano-FTIR, the optical resonances of these tips can be precisely tuned from visible to infrared to terahertz frequencies, by simply adjusting the tip length. Employing these tips for near-field infrared imaging of individual viruses, we verified state-of-the-art AFM performance, accompanied by an excellent optical performance. Due to their well-defined geometry, these antenna tips will significantly ease the qualitative description of the tip-sample near-field interaction, which will be essential for quantitative measurements of the local sample properties such as dielectric function and molecular absorption. We furthermore envision a wide application potential of these tips in infrared nano-imaging and nano-spectroscopy. Optimization of the tips could further enhance the resolution and sensitivity, eventually enabling single molecule infrared spectroscopy in the future. Shorter tips with resonances at visible and near-infrared frequencies could be applied to push the field enhancement and sensitivity in tip-enhanced Raman spectroscopy (TERS).

9 References

1 Kuzmany, H. *Solid-State Spectroscopy*. (Springer, 1998).

2 Griffiths, P. R. & de Haseth, J. A. *Fourier Transform Infrared Spectrometry*. (Wiley, 2007).

3 Garczarek, F. & Gerwert, K. Functional waters in intraprotein proton transfer monitored by FTIR difference spectroscopy. *Nature* **439**, 109-112 (2006).

4 Li, Z. Q. *et al.* Dirac charge dynamics in graphene by infrared spectroscopy. *Nature Physics* **4**, 532-535 (2008).

5 Novotny, L. & Hecht, B. *Principles of Nano-Optics*. (Cambridge University Press, 2006).

6 Keilmann, F. & Hillenbrand, R. *Nano-Optics and Near-Field Optical Microscopy*. (Artech House, Boston/London, 2008).

7 Keilmann, F. & Hillenbrand, R. Near-field optical microscopy by elastic light scattering from a tip. *Philosophical Transactions of the Royal Society of London, Series A* **362**, 787-805 (2004).

8 Huber, A. J., Keilmann, F., Wittborn, J., Aizpurua, J. & Hillenbrand, R. Terahertz Near-Field Nanoscopy of Mobile Carriers in Single Semiconductor Nanodevices. *Nano Letters* **8**, 3766-3770 (2008).

9 Stiegler, J. M. *et al.* Nanoscale Free-Carrier Profiling of Individual Semiconductor Nanowires by Infrared Near-Field Nanoscopy. *Nano Letters* **10**, 1387-1392 (2010).

10 Stiegler, J. M., Tena-Zaera, R., Idigoras, O., Chuvilin, A. & Hillenbrand, R. Correlative infrared–electron nanoscopy reveals the local structure–conductivity relationship in zinc oxide nanowires. *Nat Commun* **3**, 1131 (2012).

11 Qazilbash, M. M. *et al.* Mott transition in VO2 revealed by infrared spectroscopy and nano-imaging. *Science* **318**, 1750-1753 (2007).

12 Jones, A. C., Berweger, S., Wei, J., Cobden, D. & Raschke, M. B. Nano-optical Investigations of the Metal−Insulator Phase Behavior of Individual VO2 Microcrystals. *Nano Letters* **10**, 1574-1581 (2010).

13 Taubner, T., Hillenbrand, R. & Keilmann, F. Nanoscale polymer recognition by spectral signature in scattering infrared near-field microscopy. *Applied Physics Letters* **85**, 5064-5066 (2004).

14 Raschke, M. B. *et al.* Apertureless near-field vibrational imaging of block-copolymer nanostructures with ultrahigh spatial resolution. *ChemPhysChem* **6**, 2197-2203 (2005).

15 Akhremitchev, B. B., Pollack, S. & Walker, G. C. Apertureless scanning near-field infrared microscopy of a rough polymeric surface. *Langmuir* **17**, 2774-2781 (2001).

16 Huth, F. *et al.* Nano-FTIR Absorption Spectroscopy of Molecular Fingerprints at 20 nm Spatial Resolution. *Nano Letters* **12**, 3973-3978 (2012).

17 Knoll, B. & Keilmann, F. Near-field probing of vibrational absorption for chemical microscopy. *Nature* **399**, 134-137 (1999).

18 Brehm, M., Taubner, T., Hillenbrand, R. & Keilmann, F. Infrared spectroscopic mapping of single nanoparticles and viruses at nanoscale resolution. *Nano Letters* **6**, 1307-1310 (2006).

19 Paulite, M. *et al.* Imaging Secondary Structure of Individual Amyloid Fibrils of a β2-Microglobulin Fragment Using Near-Field Infrared Spectroscopy. *Journal of the American Chemical Society* **133**, 7376-7383 (2011).

20 Hillenbrand, R., Taubner, T. & Keilmann, F. Phonon-enhanced light-matter interaction at the nanometer scale. *Nature* **418**, 159-162 (2002).

21 Ocelic, N. & Hillenbrand, R. Subwavelenght-scale tailoring of surface phonon polaritions by focused ion-beam implantation. *Nature Materials* **3**, 606-609 (2004).

22 Huber, A. J., Ziegler, A., Kock, T. & Hillenbrand, R. Infrared nanoscopy of strained semiconductors. *Nature Nanotechnology* **4**, 153-157 (2009).
23 Chen, J. *et al.* Optical nano-imaging of gate-tunable graphene plasmons. *Nature* **487**, 77-81 (2012).
24 Fei, Z. *et al.* Gate-tuning of graphene plasmons revealed by infrared nano-imaging. *Nature* **487**, 82-85 (2012).
25 Zentgraf, T. *et al.* Amplitude- and phase-resolved optical near fields of split-ring-resonantor-based metamaterals. *Optics Letters* **33**, 848 (2008).
26 Kehr, S. C. *et al.* Anisotropy contrast in phonon-enhanced apertureless near-field microscopy using a free-electron laser. *Physical Review Letters* **100**, 256403 (2008).
27 Huber, A. J., Kazantsev, D., Keilmann, F., Wittborn, J. & Hillenbrand, R. Simultaneous IR material recognition and conductivity mapping by nanoscale near-field microscopy. *Advanced Materials* **19**, 2209-2212 (2007).
28 Russell, E. E. & Bell, E. E. Measurement of the Optical Constants of Crystal Quartz in the Far Infrared with the Asymmetric Fourier-Transform Method. *Journal of the Optical Society of America* **57**, 341-348 (1967).
29 Huth, F., Schnell, M., Wittborn, J., Ocelic, N. & Hillenbrand, R. Infrared-spectroscopic nanoimaging with a thermal source. *Nat Mater* **10**, 352-356 (2011).
30 Röseler, A. *Infrared spectroscopic ellipsometry*. (Akademie-Verlag, 1990).
31 Keilmann, F. & Amarie, S. Mid-infrared Frequency Comb Spanning an Octave Based on an Er Fiber Laser and Difference-Frequency Generation. *J Infrared Milli Terahz Waves* **33**, 479-484 (2012).
32 Brehm, M., Schliesser, A., Cajko, F., Tsukerman, I. & Keilmann, F. Antenna-mediated back-scattering efficiency in infrared near-field microscopy. *Optics Express* **16**, 11203-11215 (2008).
33 Frey, H. G., Keilmann, F., Kriele, A. & Guckenberger, R. Enhancing the resolution of scanning near-field optical microscopy by a metal tip grown on an aperture probe. *Applied Physics Letters* (2002).
34 Kalkbrenner, T., Ramstein, M., Mlynek, J. & Sandoghdar, V. A single gold particle as a probe for apertureless scanning near-field optical microscopy. *Journal of Microscopy* **202**, 72-76 (2001).
35 Kalkbrenner, T. *et al.* Optical microscopy via spectral modification of a nanoantenna. *Physical Review Letters* **95**, 200801 (2005).
36 Zou, Y., Steinvurzel, P., Yang, T. & Crozier, K. B. Surface plasmon resonances of optical antenna atomic force microscope tips. *Applied Physics Letters* **94**, 171107-171103 (2009).
37 Taminiau, T. H., Moerland, R. J., Segerink, F. B., Kuipers, L. & van Hulst, N. F. λ/4 Resonance of an Optical Monopole Antenna Probed by Single Molecule Fluorescence. *Nano Letters* **7**, 28-33 (2006).
38 Mivelle, M., van Zanten, T. S., Neumann, L., van Hulst, N. F. & Garcia-Parajo, M. F. Ultrabright Bowtie Nanoaperture Antenna Probes Studied by Single Molecule Fluorescence. *Nano Letters* (2012).
39 Taminiau, T. H., Stefani, F. D., Segerink, F. B. & Van Hulst, N. F. Optical antennas direct single-molecule emission. *Nature Photonics* **2**, 234-237 (2008).
40 Hoppener, C. & Novotny, L. Antenna-Based Optical Imaging of Single Ca2+ Transmembrane Proteins in Liquids. *Nano Letters* **8**, 642-646 (2008).
41 Johnson, T. W. *et al.* Highly Reproducible Near-Field Optical Imaging with Sub-20-nm Resolution Based on Template-Stripped Gold Pyramids. *ACS Nano* **6**, 9168-9174 (2012).
42 Weber-Bargioni, A. *et al.* Hyperspectral Nanoscale Imaging on Dielectric Substrates with Coaxial Optical Antenna Scan Probes. *Nano Letters* **11**, 1201-1207 (2011).

43 Fleischer, M. Near-field scanning optical microscopy nanoprobes. *Nanotechnol. Rev.* **1(4)**, 313 (2012).
44 Fleischer, M. *et al.* Gold Nanocone Near-Field Scanning Optical Microscopy Probes. *ACS Nano* **5**, 2570-2579 (2011).
45 Fleischer, M. *et al.* Three-dimensional optical antennas: Nanocones in an apertureless scanning near-field microscope. *Applied Physics Letters* **93**, 111114-111113 (2008).
46 Neacsu, C. C. *et al.* Near-Field Localization in Plasmonic Superfocusing: A Nanoemitter on a Tip. *Nano Letters* **10**, 592-596 (2010).
47 Berweger, S., Atkin, J. M., Olmon, R. L. & Raschke, M. B. Light on the Tip of a Needle: Plasmonic Nanofocusing for Spectroscopy on the Nanoscale. *The Journal of Physical Chemistry Letters* **3**, 945-952 (2012).
48 Ferguson, B. & Zhang, X. C. Materials for terahertz science and technology. *Nature Materials* **1**, 26-33 (2002).
49 Mittleman, D. *Sensing with THz radiation*. (Springer Verlag, 2003).
50 Tonouchi, M. Cutting-edge terahertz technology. *Nature Photonics* **1**, 97-105 (2007).
51 Chan, W. L., Deibel, J. & Mittleman, D. M. Imaging with terahertz radiation. *Reports on Progress in Physics* **70**, 1325-1379 (2007).
52 Withayachumnankul, W. *et al.* T-ray sensing and imaging. *Proceedings of the Ieee* **95**, 1528-1558 (2007).
53 Schuller, J. A. *et al.* Plasmonics for extreme light concentration and manipulation. *Nature Materials* **9**, 193-204 (2010).
54 Michelson, A. A. *Philos. Mag.* **31** (1891).
55 Michelson, A. A. Light Waves and their Uses. *University of Chicago Press* (1902).
56 <"http://riodb01.ibase.aist.go.jp/sdbs/ (National Institute of Advanced Industrial Science and Technology, 31 January 2012)" SDBS Nr. 4062> (
57 Brigham, E. O. *The Fast Fourier Transform and Its Applications*. (Prentice Hall, 1988).
58 Bracewell, R. N. *The Fourier Transform and Its Applications*. (McGraw-Hill Education, 2000).
59 Huber, A. J. *Nanoscale Surface-Polariton Spectroscopy by Mid- and Far-Infrared Near-Field Microscopy* PhD thesis, TU Munich, (2009).
60 Ocelić, N. *Quantitative Near-field Phonon-polariton Spectroscpy* PhD thesis, TU Munich, (2007).
61 Cvitković, A. *Substrate-Enhanced Scattering-Type Scanning Near-Field Infrared Microscopy of Nanoparticles* PhD thesis, TU Munich, (2009).
62 Stiegler, J. M. *Infrared spectroscopic near-field microscopy of nanoparticles and semiconductor nanowires* PhD thesis, University of the Basque Country, (2012).
63 Born, M. & Wolf, E. *Principles of optics*. (Cambridge University Press, 1999).
64 Hecht, E. *Optics*. (Addison Wesley, 2002).
65 Hawkes, P. W. & Spence, J. C. H. *Science of microscopy*. (Springer, 2007).
66 Hell, S. W. Toward fluorescence nanoscopy. *Nature Biotechnology* **21**, 1347-1355, doi:10.1038/nbt895 (2003).
67 Hell, S. W., Lindek, S., Cremer, C. & Stelzer, E. H. K. Measurement of the 4Pi-confocal point-spread function proves 75nm axial resolution. *Applied Physics Letters* **64**, 1335-1337, doi:10.1063/1.111926 (1994).
68 Hell, S. W. Far-field optical nanoscopy. *Science* **316**, 1153-1158, doi:10.1126/science.1137395 (2007).
69 Betzig, E. *et al.* Imaging intracellular fluorescent proteins at nanometer resolution. *Science* **313**, 1642-1645, doi:10.1126/science.1127344 (2006).
70 Rust, M. J., Bates, M. & Zhuang, X. W. Sub-diffraction-limit imaging by stochastic optical reconstruction microscopy (STORM). *Nature Methods* **3**, 793-795, doi:10.1038/nmeth929 (2006).

71 Peters, R., Peters, J., Tews, K. H. & Bahr, W. MICROFLUORIMETRIC STUDY OF TRANSLATIONAL DIFFUSION IN ERYTHROCYTE-MEMBRANES. *Biochimica Et Biophysica Acta* **367**, 282-294, doi:10.1016/0005-2736(74)90085-6 (1974).
72 Brown, E. B., Wu, E. S., Zipfel, W. & Webb, W. W. Measurement of molecular diffusion in solution by multiphoton fluorescence photobleaching recovery. *Biophysical Journal* **77**, 2837-2849, doi:10.1016/s0006-3495(99)77115-8 (1999).
73 Selvin, P. R. The renaissance of fluorescence resonance energy transfer. *Nature Structural Biology* **7**, 730-734, doi:10.1038/78948 (2000).
74 Meyer, E., Hug, H. J. & Bennewitz, R. *Scanning Probe Microscopy: The Lab on a Tip*. (Springer, 2004).
75 *Nanotribology and Nanomechanics: An Introduction*. (2006).
76 Binning, G., Rohrer, H., Gerber, C. & Weibel, E. SURFACE STUDIES BY SCANNING TUNNELING MICROSCOPY. *Physical Review Letters* **49**, 57-61, doi:10.1103/PhysRevLett.49.57 (1982).
77 Binnig, G. & Rohrer, H. SCANNING TUNNELING MICROSCOPY. *Surface Science* **126**, 236-244, doi:10.1016/0039-6028(83)90716-1 (1983).
78 Binnig, G., Quate, C. F. & Gerber, C. Atomic force microscopy. *Physical Review Letters* **56**, 930-933 (1986).
79 Ash, E. A. & Nicholls, G. Super-resolution aperture scanning microscope. *Nature* **237**, 510-512 (1972).
80 Knoll, B. *Abtastende Nahfeldmikroskopie mit Infrarot- und Mikrowellen* PhD thesis, Aachen, (1999).
81 Zenhausern, F., O´Boyle, M. P. & Wickramasinghe, H. K. Apertureless near-field optical microscope. *Applied Physics Letters* **65**, 1623-1625 (1994).
82 Zenhausern, F., Martin, Y. & Wickramasinghe, H. K. Scanning Interferometric Apertureless Microscopy: Optical Imaging at 10 Angstrom Resolution. *Science* **269**, 1083-1085 (1995).
83 Inouye, Y. & Kawata, S. Near-field scanning optical microscope with a metallic probe tip. *Opt. Lett.* **19**, 159-161 (1994).
84 Inouye, Y. & Kawata, S. Near-field scanning optical microscope with a metallic probe tip. *Optics Letters* **19**, 159-161 (1994).
85 Lahrech, A., Bachelot, R., Gleyzes, P. & Boccara, A. C. Infrared-reflection-mode near-field microscopy using an apertureless probe with a resolution of λ/600. *Optics Letters* **21**, 1315-1317 (1996).
86 Chen, H.-T., Kersting, R. & Cho, G. C. Terahertz imaging with nanometer resolution. *Applied Physics Letters* **83**, 3009-3011 (2003).
87 Schunk, P. *Untersuchung von Oberflächen und Oberflächenprozessen mit dem Rasterkraftmikroskop* Diplom thesis, Universität Karlsruhe (TH), (1998).
88 Salerno, M. *et al.* Plasmon polaritons in metal nanostructures: the optoelectronic route to nanotechnology. *Optoelectronics Review* **10**, 217-224 (2002).
89 Krenn, J. R. & Weeber, J. C. Surface Plasmon polaritons in metal stripes and wires. *Philosophical Transactions of the Royal Society of London, Series A* **362**, 739-756 (2004).
90 Crozier, K. B., Sundaramurthy, A., Kino, G. S. & Quate, C. F. Optical antennas: Resonators for local field enhancement. *Journal of Applied Physics* **94**, 4632-4642 (2003).
91 Ocelic, N., Huber, A. & Hillenbrand, R. Pseudo-heterodyne detection for background-free near-field spectroscopy. *Applied Physics Letters* **89**, 101124 (2006).
92 Samson, J.-S. *et al.* Characterization of single diamondlike and polymerlike nanoparticles by midinfrared nanospectroscopy. *Journal of Applied Physics* **105**, 064908 (2009).

93 Kopf, I. *et al.* Chemical Imaging of Microstructured Self-Assembled Monolayers with Nanometer Resolution. *The Journal of Physical Chemistry C* **111**, 8166-8171 (2007).
94 Brehm, M., Schliesser, A. & Keilmann, F. Spectroscopic near-field microscopy using frequency combs in the mid-infrared. *Optics Express* **14**, 11222-11233 (2006).
95 Amarie, S. & Keilmann, F. Broadband-infrared assessment of phonon resonance in scattering-type near-field microscopy. *Physical Review B* **83**, 045404 (2011).
96 De Wilde, Y. *et al.* Thermal radiation scanning tunnelling microscopy. *Nature* **444**, 740-743 (2006).
97 Raschke, M. B. US Patent Application No. US2010/0045970 A1 and Personal Communication.
98 Govyadinov, A. A., Amenabar, I., Huth, F., Carney, P. S. & Hillenbrand, R. Quantitative Measurement of Local Infrared Absorption and Dielectric Function with Tip-Enhanced Near-Field Microscopy. *Journal of Physical Chemistry Letters* **4**, 1526-1531, doi:10.1021/jz400453r (2013).
99 Cvitkovic, A., Ocelic, N., Aizpurua, J., Guckenberger, R. & Hillenbrand, R. Infrared Imaging of Single Nanoparticles via Strong Field Enhancement in a Scanning Nanogap. *Physical Review Letters* **97**, 060801 (2006).
100 Keilmann, F. Vibrational-infrared near-field microscopy. *Vibrational Spectroscopy* **29**, 109-114 (2002).
101 Samson, J.-S. *et al.* Setup of a scanning near field infrared microscope (SNIM): Imaging of sub-surface nano-structures in gallium-doped silicon. *Physical Chemistry Chemical Physics* **8**, 753-758 (2006).
102 Gunde, M. K. Vibrational modes in amorphous silicon dioxide. *Physica B: Condensed Matter* **292**, 286-295 (2000).
103 Masetti, G., Severi, M. & Solmi, S. Modeling of carrier mobility against carrier concentration in arsenic-, phosphorus-, and boron-doped silicon. *IEEE Transactions on Electron Devices* **30**, 764-769 (1983).
104 Huber, A. J., Wittborn, J. & Hillenbrand, R. Infrared spectroscopic near-field mapping of single nanotransistors. *Nanotechnology* **21**, 235702 (2010).
105 Cvitkovic, A., Ocelic, N. & Hillenbrand, R. Analytical model for quantitative prediction of material contrasts in scattering-type near-field optical microscopy. *Optics Express* **15**, 8550 (2007).
106 Hermann, P. *et al.* Near-field imaging and nano-Fourier-transform infrared spectroscopy using broadband synchrotron radiation. *Optics Express* **21**, 2913-2919, doi:10.1364/oe.21.002913 (2013).
107 Taubner, T., Hillenbrand, R. & Keilmann, F. Performance of visible and mid-infrared scattering-type near-field optical microscopes. *J. Microscopy* **210**, 311-314 (2003).
108 Taubner, T., Keilmann, F. & Hillenbrand, R. Nanoscale-resolved subsurfacce imaging by scattering-type near-field optical microscopy. *Optics Express* **13**, 8893-8898 (2005).
109 Raschke, M. B. & Lienau, C. Apertureless near-field optical microscopy: Tip--sample coupling in elastic light scattering. *Applied Physics Letters* **83**, 5089-5091 (2003).
110 Stuart, B. H. *Infrared Spectroscopy. Fundamentals and Applications*. (Wiley, 2004).
111 Ocelic, N. & Hillenbrand, R. Optical device for measuring modulated signal light, Patent No. EP1770714B1 and US 7738115 B2.
112 Huth, F., Schnell, M., Wittborn, J., Ocelic, N. & Hillenbrand, R. Infrared-spectroscopic nanoimaging with a thermal source. *Nature Materials* **10**, 352-356 (2011).
113 Labardi, M., Patane, S. & Allegrini, M. Artifact-free near-field optical imaging by apertureless microscopy. *Applied Physics Letters* **77**, 621-623 (2000).
114 Hillenbrand, R. & Keilmann, F. Complex optical constants on a subwavelength scale. *Physical Review Letters* **85**, 3029-3032 (2000).

115 Stiegler, J. M. *et al.* Nanoscale Infrared Absorption Spectroscopy of Individual Nanoparticles Enabled by Scattering-Type Near-Field Microscopy. *ACS Nano* **5**, 6494-6499 (2011).
116 Neubrech, F. *et al.* Resonant Plasmonic and Vibrational Coupling in a Tailored Nanoantenna for Infrared Detection. *Physical Review Letters* **101**, 157403 (2008).
117 Adato, R. *et al.* Ultra-sensitive vibrational spectroscopy of protein monolayers with plasmonic nanoantenna arrays. *Proceedings of the National Academy of Sciences* **106**, 19227-19232 (2009).
118 Krutokhvostov, R. *et al.* Enhanced resolution in subsurface near-field optical microscopy. *Opt. Express* **20**, 593-600 (2012).
119 Magonov, S. N. & Reneker, D. H. Characterization of polymer surfaces with atomic force microscopy. *Annual Review of Materials Science* **27**, 175-222 (1997).
120 Danilov, V., Wagner, H.-E. & Meichsner, J. Modification of Polydimethylsiloxane Thin Films in H2 Radio-frequency Plasma Investigated by Infrared Reflection Absorption Spectroscopy. *Plasma Processes and Polymers* **8**, 1059-1067 (2011).
121 Aizpurua, J. *et al.* Optical properties of coupled metallic nanorods for field-enhanced spectroscopy. *Physical Review B* **71**, 235420 (2005).
122 Balanis, C. A. *Antenna Theory*. (John Wiley & Sons, Inc., 2005).
123 Alu, A. & Engheta, N. Input Impedance, Nanocircuit Loading, and Radiation Tuning of Optical Nanoantennas. *Physical Review Letters* **101**, 043901 (2008).
124 Alu, A. & Engheta, N. Tuning the scattering response of optical nanoantennas with nanocircuit loads. *Nature Photonics* **2**, 307-310 (2008).
125 Dorfmüller, J. *et al.* Fabry-Pérot Resonances in One-Dimensional Plasmonic Nanostructures. *Nano Letters* **9**, 2372-2377 (2009).
126 Nelayah, J. *et al.* Mapping surface plasmons on a single metallic nanoparticle. *Nat Phys* **3**, 348-353 (2007).
127 Michel, B., Vicki, J. K., Masashi, W., Abbas, I. M. & Michael, B. C. Mapping surface plasmons at the nanometre scale with an electron beam. *Nanotechnology* **18**, 165505 (2007).
128 Rossouw, D., Couillard, M., Vickery, J., Kumacheva, E. & Botton, G. A. Multipolar Plasmonic Resonances in Silver Nanowire Antennas Imaged with a Subnanometer Electron Probe. *Nano Letters* **11**, 1499-1504 (2011).
129 Koh, A. L., Fernández-Domínguez, A. I., McComb, D. W., Maier, S. A. & Yang, J. K. W. High-Resolution Mapping of Electron-Beam-Excited Plasmon Modes in Lithographically Defined Gold Nanostructures. *Nano Letters* **11**, 1323-1330 (2011).
130 Bridges, J. M. & Migdall, A. L. Characterization of argon arc source in the infrared. *Metrologia* **32**, 625-628 (1995/1996).
131 McIntosh, A. L., Wofford, B. A., Lucchese, R. R. & Bevan, J. W. High resolution Fourier transform infrared spectroscopy using a high temperature argon arc source. *Infrared Physics & Technology* **42**, 509-514 (2001).
132 Novotny, L. Effective Wavelength Scaling for Optical Antennas. *Physical Review Letters* **98**, 266802 (2007).
133 Xu, X. G., Rang, M., Craig, I. M. & Raschke, M. B. Pushing the Sample-Size Limit of Infrared Vibrational Nanospectroscopy: From Monolayer toward Single Molecule Sensitivity. *The Journal of Physical Chemistry Letters* **3**, 1836-1841, doi:10.1021/jz300463d (2012).
134 Amarie, S. *et al.* Nano-FTIR chemical mapping of minerals in biological materials. *Beilstein J. Nanotechnol.* **3**, 312–323 (2012).

10 Own Publications

Presented in this thesis:

1. **F. Huth**, M. Schnell, J. Wittborn, N. Ocelic, and R. Hillenbrand
   Infrared-spectroscopic nanoimaging with a thermal source
   Nature Materials **10**, 352-356 (2011)
   CeNS Publication Award 2011

2. **F. Huth**, A.A. Govyadinov, S. Amarie,W. Nuansing, F. Keilmann, and R. Hillenbrand
   Nano-FTIR absorption spectroscopy of molecular fingerprints at 20 nm spatial resolution
   Nano Letters **12(8)**, 3973 (2012)
   CeNS Publication Award 2012
   Microscopy Today Innovation Award 2013

3. **F. Huth**, A. Chuvilin, M. Schnell, I. Amenabar, R. Krutokhvostov, and R. Hillenbrand
   Resonant Antenna Probes for Tip-Enhanced Infrared Near-field Microscopy
   Nano Letters **13(3)**, 1065 (2013)

Related publications:

4. J. Chen*, M. Badioli*****, P. Alonso-Gonzalez*****, S. Thongrattanasiri*****, **F. Huth***, J. Osmond, M. Spasenovic, A. Centeno, A. Pesquera, P. Godignon, A. Zurutuza Elorza, N. Camara,F. Javier Garcia de Abajo, R. Hillenbrand and F. H. L. Koppens
   Optical nano-imaging of gate-tunable graphene plasmons
   Nature **487**, 77 (2012) ***equally contributed first author***

5. J. Chen , P. Albella , Z. Pirzadeh , P. Alonso-Gonzalez , **F. Huth**, S. Bonetti , V. Bonanni, J. Akerman , J. Nogues , P. Vavassori , A. Dmitriev , J. Aizpurua , and R. Hillenbrand
   Plasmonic Nickel Nanoantennas
   Small **16**, 2341-2347 (2011)

6. R. Krutokhvostov, A. A. Govyadinov, J.M. Stiegler, **F. Huth**, A. Chuvilin, P. S. Carney,and R. Hillenbrand
   Enhanced resolution in subsurface near-field optical microscopy
   Optics Express **20**, 599 (2012)

7. P. Alonso-Gonzalez, P. Albella, M. Schnell, J. Chen, **F. Huth**, A. Garcia-Etxarri, F. Casanova,F. Golmar, L. Arzubiaga, L.E. Hueso, J. Aizpurua and R. Hillenbrand
   Resolving the electromagnetic mechanism of surface-enhanced light scattering at single hotspots
   Nature Communications **3**:684 (2012)

8. Alexander A. Govyadinov, I. Amenabar, **F. Huth**, P. S. Carney and R. Hillenbrand
Quantitative Measurement of Local Infrared Absorption and Dielectric Function with Tip-Enhanced Near-Field Microscopy
Journal of Physical Chemistry Letters (JPCL) **9**, 1526-1531 (2013)

9. I. Amenabar, S. Poly, W. Nuansing, E. H. Hubrich, A. A. Govyadinov, **F. Huth**, R. Krutokhvostov, L. Zhang, M. Knez, J. Heberle, A. Bittner & R. Hillenbrand
Structural analysis and mapping of individual protein complexes by infrared nanospectroscopy
Nature Communications **3**:890 (2013)

10. P. Hermann, A. Hoehl, P. Patoka, **F. Huth**, E. Rühl, and G. Ulm
Near-Field Imaging and Nano-Fourier-Transform Infrared Spectroscopy using Broadband Synchrotron Radiation
Optics Express **21**, 2913 (2013)

11 Acknowledgements

I want to express my gratitude to Prof. Rainer Hillenbrand, group leader of the NanoOptics group at NanoGUNE, for supervising my thesis. I am very thankful for his numerous ideas and motivating suggestions, the inspiring discussions and his constructive criticism about my conducted projects and the scientific presentation of my results.

I thank Prof. Txema Pitarke, director of CIC NanoGUNE, for the opportunity to work and carry out my experiments in the beautiful city of Donostia - San Sebastian, Spain.

I am thankful to all the present and past members of the NanoOptics group at NanoGUNE, including Dr. Alexander Govyadinov (Sasha), Dr. Johannes Stiegler, Dr. Martin Schnell, Dr. Simon Poly, Dr. Jianing Chen, Dr. Pablo Alonso-Gonzales, Paulo Sarriugarte, Stefan Mastel, Iban Amenabar, Roman Krutokhvostov and Carlos Crespo, for interesting and helpful discussions and the great atmosphere in the group. Special thanks to Sasha for great theoretical and to Carlos for technical support.

I want to thank all members of NanoGUNE for providing a great environment to conduct scientific work. Especially I want to thank Prof. Andrey Chuvilin for Focused Ion Beam (FIB) tip preparation and Electron Energy Loss Spectroscopy (EELS), and for valuable insights into electron microscopy. Many thanks also to Prof. Alex Bittner for valuable discussions and a great lecture on proteins.

Thanks to all Neaspec members, including Dr. Stefan Schiefer, Dr. Marcus Diem, Dr. Andreas Huber, Dr. Nenad Ocelic, Dr. Antonija Cvitkovic, Dr. Sergiu Amarie, Dr. Adrian Cernescu, Dr. Tobias Gokus, Dr. Miriam Böhmler, Patrick Borek, Ulf Waldmann and Dr. Fritz Keilmann, who supported me at all times during this thesis.

Special thanks to Dr. Reinhard Guckenberger, who was my advisor during my “Diplomarbeit”, and since then always had an open ear for my questions. I´m also very thankful for all the valuable insights he gave me in AFM technology and analog electronics.

I want to thank all collaborators, especially Prof. Javier Aizpurua, Prof. Scott Carney and Prof. Frank Koppens, who contributed to the projects within this thesis.

Finally I want to thank my family and my wonderful wife Sarah for all the support before and during this thesis.